

COLLOIDAL PROCESSING AND PHOTOCATALYTIC PROPERTIES OF  
TITANATE-NIOBATE NANOSHEETS

BY

TYLER ARTHUR GUBB

A THESIS  
SUBMITTED TO THE FACULTY OF

ALFRED UNIVERSITY

IN PARTIAL FULFILLMENT OF THE REQUIREMENTS  
FOR THE DEGREE OF

MASTER OF SCIENCE

IN

MATERIALS SCIENCE & ENGINEERING

ALFRED, NEW YORK

SEPTEMBER, 2016

COLLOIDAL PROCESSING AND PHOTOCATALYTIC PROPERTIES OF  
TITANATE-NIOBATE NANOSHEETS

BY

Tyler Arthur Gubb

B.S. Alfred University, 2013

SIGNATURE OF AUTHOR \_\_\_\_\_

APPROVED BY \_\_\_\_\_  
Dr. Scott Misture, ADVISOR

\_\_\_\_\_  
Dr. Steven M. Pilgrim, ADVISORY COMMITTEE

\_\_\_\_\_  
Dr. Herbert Giesche, ADVISORY COMMITTEE

\_\_\_\_\_  
CHAIR, ORAL THESIS DEFENSE

ACCEPTED BY \_\_\_\_\_  
ALASTAIR N. CORMACK, INTERIM DEAN  
KAZUO INAMORI SCHOOL OF ENGINEERING

Alfred University theses are copyright protected and may be used for education or personal research only. Reproduction or distribution in part or whole is prohibited without written permission from the author.

Signature page may be viewed at Scholes Library, New York State College of Ceramics, Alfred University, Alfred, New York.

## ACKNOWLEDGMENTS

The Alfred community, my family, and my friends deserve recognition for helping me complete this project. Dr. Misture, thank you taking me on as part of your research group and lending me your wisdom, insight, and patience. I've learned far more than just materials science. Thank you to Dr. Pilgrim and Dr. Liu for serving on my committee and for their expertise, and a special thank you to Dr. Giesche for replacing Dr. Liu at a very late stage in my thesis. Alfred's technical support team, including Swavek, Gerry, and Jim, were always willing to help my experiments and provide advice. Thank you all. I genuinely appreciate the help lent by my fellow graduate students, especially Peter, Trevyn, Wei, and Peng. Kirsten Fuller tirelessly helped me with sample preparation and experiments, and often helped my lab work be a bit more entertaining. I especially thank Ruby for her emotional (and sometimes, in a sense, spiritual) support. She's tolerated me and my lab work for a long time now, but I cannot express enough how much our friendship has helped me, especially during grad school. I want to thank my many Alfred friends (most of whom have moved, but never completely left) for their support and companionship. Lastly, I need to recognize the love and support of my family. To them, I still insist ceramic engineering is more than just making pots, as I hope the following thesis will demonstrate...

# TABLE OF CONTENTS

	<b>Page</b>
Acknowledgments .....	ii
Table of Contents .....	iii
List of Tables .....	iv
List of Figures .....	v
Abstract .....	ix
<b>I. INTRODUCTION .....</b>	<b>1</b>
<b>II. EXPERIMENTAL .....</b>	<b>6</b>
A. Nanosheet Synthesis .....	6
B. Assembly .....	6
C. Photocatalysis .....	7
D. Apparatuses .....	8
<b>III. RESULTS AND DISCUSSION .....</b>	<b>10</b>
A. Ion Exchange and Exfoliation .....	10
B. Self-Assembly by Gelation and Flocculation .....	19
1. Gelation .....	19
2. Flocculation .....	29
3. Liquid Crystals .....	32
C. Self-Assembled Microstructures .....	33
1. Gelation .....	33
2. Flocculation .....	39
D. Photocatalysis .....	45
1. Optical Properties of Nanosheets .....	45
2. Photocatalytic Hydrogen Production .....	48
3. Methylene Blue Dye Degradation .....	52
<b>IV. CONCLUSION .....</b>	<b>56</b>
<b>V. FUTURE WORK .....</b>	<b>58</b>
<b>VI. REFERENCES .....</b>	<b>60</b>

## LIST OF TABLES

	<b>Page</b>
Table I: Structural Data For The Chemistries Employed In This Study. “Motif” Refers To The Grouping Of Edge-Shared (Ti,Nb)-O Polyhedra. Theoretical Specific Surface Area (tSSA) Considers Single Sheets As Flat Surfaces. Theoretical Specific Surface Charge (tSSC) Denotes The Charge Per Unit Area For One Sheet Only. Solids Loading Specifies Approximate Nanosheet Mass Per Volume As Measured Following Exfoliation. ....	10
Table II: Summarized TGA Data For Exfoliated HTiNbO <sub>5</sub> , Exfoliated H <sub>3</sub> Ti <sub>5</sub> NbO <sub>14</sub> , And Exfoliated HTi <sub>2</sub> NbO <sub>7</sub> Reassembled With Na <sub>2</sub> SO <sub>4</sub> Or HCl.....	26
Table III: Specific surface area, average pore width, and specific pore volume (BJH adsorption) for gelled and flocculated exfoliated nanosheets. ....	40
Table IV: Summarized Band Gap Energies For Parent And Exfoliated Phases.....	45
Table V: Measured Hydrogen Rates For P25, Exfoliated HTiNbO <sub>5</sub> , Exfoliated H <sub>3</sub> Ti <sub>5</sub> NbO <sub>14</sub> , and Exfoliated HTi <sub>2</sub> NbO <sub>7</sub> Nanosheets With And Without Pt Co-Catalyst. ....	50
Table VI: Measured hydrogen rates for exfoliated HTiNbO <sub>5</sub> , exfoliated H <sub>3</sub> Ti <sub>5</sub> NbO <sub>14</sub> , and exfoliated HTi <sub>2</sub> NbO <sub>7</sub> flocculated with Na <sub>2</sub> SO <sub>4</sub> , rinsed, boiled in IPA to produce a high surface area powder, heated to temperature, dispersed in H <sub>2</sub> O, then loaded with 1% Pt.....	50
Table VII: Methylene Blue Decomposition Rates, Correlation Coefficients, Theoretical Specific Surface Area, and Theoretical Specific Surface Charge For Each Chemistry. ....	54

## LIST OF FIGURES

	<b>Page</b>
Figure 1. Illustrated structures of (a) $\text{KTiNbO}_5$ , (b) $\text{K}_3\text{Ti}_5\text{NbO}_{14}$ , and (c) $\text{CsTi}_2\text{NbO}_7$ . Interlayer alkali ions have been omitted for clarity. Dashed lines denote the unit cell.....	11
Figure 2. XRD patterns for (a) $\text{KTiNbO}_5$ , $\text{HTiNbO}_5$ , and exfoliated $\text{HTiNbO}_5$ ; (b) $\text{K}_3\text{Ti}_5\text{NbO}_{14}$ , $\text{H}_3\text{Ti}_5\text{NbO}_{14}$ , and exfoliated $\text{H}_3\text{Ti}_5\text{NbO}_{14}$ ; (c) $\text{CsTi}_2\text{NbO}_7$ , $\text{HTi}_2\text{NbO}_7$ , and exfoliated $\text{HTi}_2\text{NbO}_7$ . Exfoliated samples were dried at room temperature onto flat XRD sample holders. Peaks are denoted beneath patterns as tick marks from available PDF cards: ( $\text{KTiNbO}_5$ ) 04-009-8714, ( $\text{HTiNbO}_5$ ) 04-011-3432, ( $\text{K}_3\text{Ti}_5\text{NbO}_{14}$ ) 04-010-0680, ( $\text{CsTi}_2\text{NbO}_7$ ) 04-012-8410, and ( $\text{HTi}_2\text{NbO}_7$ ) 00-054-1154.....	14
Figure 3. AFM images for exfoliated $\text{HTi}_2\text{NbO}_7$ showing nanosheet thicknesses of (a) 1.7 nm and (b) 1.2 nm.....	14
Figure 4. Proposed restacking scheme for the nanosheets studied using exfoliated $\text{HTiNbO}_5$ as a prototype, as measured by XRD and AFM. Ti/Nb-O octahedra are illustrated as polyhedra for clarity, however the model was constructed using space-filling atoms.	15
Figure 5. XRD patterns of exfoliated $\text{HTiNbO}_5$ dried as-prepared, following acid treatment to induce gelation at pH 6, heat treatment to 200° C, 250° C, and treated to pH 6 followed by 250° C.....	17
Figure 6. Infrared spectra for exfoliated $\text{HTiNbO}_5$ : $\text{Na}_2\text{SO}_4$ flocculated and boiled in isopropanol, gelled with HCl at pH 3.98, and gelled at pH 0.98.....	17
Figure 7. Infrared spectra for exfoliated $\text{HTiNbO}_5$ with intercalated TBA exposed to 500 W Xe lamp for 0, 60, 120, and 240 minutes.....	18
Figure 8. Image of suspended exfoliated $\text{HTiNbO}_5$ under vigorous stirring as viewed through crossed polarizers. Image width corresponds to approximately 5 cm.....	18
Figure 9. Image of exfoliated $\text{HTiNbO}_5$ flocculated with $\text{Na}_2\text{SO}_4$ (left) and gelled with HCl (right). Tube height is approximately 3 cm. Concentration of $\text{Na}_2\text{SO}_4$ was 0.04 M and pH of gelation was 1.5.....	20
Figure 10. Optical micrograph of gelled exfoliated $\text{HTiNbO}_5$ . Image captured through a 40x objective and crossed polarizers.....	20

Figure 11. Viscosity at 0.1/s measured as a function of pH for suspensions of exfoliated HTiNbO <sub>5</sub> (diamonds), exfoliated H <sub>3</sub> Ti <sub>5</sub> NbO <sub>14</sub> (squares), and exfoliated HTi <sub>2</sub> NbO <sub>7</sub> (circles). .....	21
Figure 12. Stress curves measured as functions of shear rate and pH for suspensions of exfoliated HTiNbO <sub>5</sub> (a), exfoliated H <sub>3</sub> Ti <sub>5</sub> NbO <sub>14</sub> (b), and exfoliated HTi <sub>2</sub> NbO <sub>7</sub> (c). .....	23
Figure 13. XRD patterns of wet suspensions of exfoliated HTiNbO <sub>5</sub> , exfoliated H <sub>3</sub> Ti <sub>5</sub> NbO <sub>14</sub> , and exfoliated HTi <sub>2</sub> NbO <sub>7</sub> gels. Suspension pH was approximately 1.5. Measured in reflection geometry with variable slit source and detector. D-spacings and Miller indices are labeled for observed reflections in accordance with the peak indices of the parent phases. ....	24
Figure 14. TGA curves for exfoliated HTiNbO <sub>5</sub> , exfoliated H <sub>3</sub> Ti <sub>5</sub> NbO <sub>14</sub> , and exfoliated HTi <sub>2</sub> NbO <sub>7</sub> reassembled with Na <sub>2</sub> SO <sub>4</sub> or HCl. ....	26
Figure 15. XRD patterns for dry films of exfoliated HTiNbO <sub>5</sub> treated to pH 11, pH 6.00, 4.57, 3.76, 2.48, 1.53, and 0.99. Measured in reflection geometry. ....	27
Figure 16. XRD patterns for dry films of exfoliated H <sub>3</sub> Ti <sub>5</sub> NbO <sub>14</sub> treated to pH 11, 5.98, 5.05, 4.01, 3.01, 2.02, and 0.98. ....	27
Figure 17. XRD patterns for dry films of exfoliated HTi <sub>2</sub> NbO <sub>7</sub> treated to pH 11, pH 6.34, 4.98, 3.99, 2.98, 1.93, and 0.99. ....	28
Figure 18. Images of exfoliated H <sub>3</sub> Ti <sub>5</sub> NbO <sub>14</sub> treated with HCl to pH 4.90 (a), 4.08 (b), 3.05 (c), 1.97 (d), 1.36 (e), 0.90 (f), and 0.38 (g) having been allowed to settle for 24 hours. The volume of each sample was approximately 4.5 ml. Dashed line denotes approximate liquid height. ....	29
Figure 19. Image of exfoliated HTiNbO <sub>5</sub> flocculated with Na <sub>2</sub> SO <sub>4</sub> . Image corresponds to a length of approximately 5 cm. No additional processing had been performed after flocculation. ....	30
Figure 20. Optical micrograph of exfoliated HTiNbO <sub>5</sub> flocculated with Na <sub>2</sub> SO <sub>4</sub> . Image captured through a 40x objective and crossed polarizers. ....	30
Figure 21. XRD patterns of exfoliated HTiNbO <sub>5</sub> , exfoliated H <sub>3</sub> Ti <sub>5</sub> NbO <sub>14</sub> , and exfoliated HTi <sub>2</sub> NbO <sub>7</sub> flocculated with Na <sub>2</sub> SO <sub>4</sub> , rinsed, and suspended in H <sub>2</sub> O. Concentration of Na <sub>2</sub> SO <sub>4</sub> in the suspension was approximately 0.04 molar. Measured in reflection geometry with variable divergence slits. ....	31

Figure 22. XRD patterns for exfoliated HTiNbO <sub>5</sub> treated with Cs <sub>2</sub> CO <sub>3</sub> in suspension and dried as a film. Concentration of Cs <sub>2</sub> CO <sub>3</sub> was approximately 0.04 molar. ....	32
Figure 23. BET isotherms and pore size distributions (insets) for (a) assembled exfoliated HTiNbO <sub>5</sub> , (b) exfoliated H <sub>3</sub> Ti <sub>5</sub> NbO <sub>14</sub> , and (c) exfoliated HTi <sub>2</sub> NbO <sub>7</sub> gels. Pore size distributions were calculated from the BJH adsorption with a Halsey:Faas correction. ....	34
Figure 24. SEM image of freeze dried exfoliated and gelled HTi <sub>2</sub> NbO <sub>7</sub> assembly. ....	35
Figure 25. XRD patterns for assemblies of exfoliated and gelled HTiNbO <sub>5</sub> , H <sub>3</sub> Ti <sub>5</sub> NbO <sub>14</sub> , HTi <sub>2</sub> NbO <sub>7</sub> powders dried at 75° C. D-spacings are provided for primary peaks. Samples were measured in reflection geometry with variable divergence slits. ....	36
Figure 26. XPS survey spectra of exfoliated and HCl gelled (a) HTiNbO <sub>5</sub> , H <sub>3</sub> Ti <sub>5</sub> NbO <sub>14</sub> , and HTi <sub>2</sub> NbO <sub>7</sub> . Auger transitions and XPS peaks are labeled accordingly. High resolution XPS spectra of (b) Ti 2p, (c) Nb 3d, (d) O 1s peaks for each chemistry. ....	38
Figure 27. BET isotherms and pore size distributions (insets) for (a) assembled exfoliated HTiNbO <sub>5</sub> , (b) exfoliated H <sub>3</sub> Ti <sub>5</sub> NbO <sub>14</sub> , and (c) exfoliated HTi <sub>2</sub> NbO <sub>7</sub> . Exfoliated suspensions were flocculated with Na <sub>2</sub> SO <sub>4</sub> , boiled in IPA, and subsequently heated to 400° C. Pore size distributions were calculated from BJH adsorption. ....	41
Figure 28. SEM image of freeze dried exfoliated and flocculated HTiNbO <sub>5</sub> assembly. ....	42
Figure 29. XRD patterns for exfoliated and flocculated HTiNbO <sub>5</sub> , H <sub>3</sub> Ti <sub>5</sub> NbO <sub>14</sub> , and HTi <sub>2</sub> NbO <sub>7</sub> assemblies. Suspensions were flocculated with Na <sub>2</sub> SO <sub>4</sub> to a concentration of 0.04M. Samples were measured in reflection geometry with variable slits. ....	42
Figure 30. XPS survey spectra of exfoliated and Na <sub>2</sub> SO <sub>4</sub> flocculated (a) HTiNbO <sub>5</sub> , H <sub>3</sub> Ti <sub>5</sub> NbO <sub>14</sub> , and HTi <sub>2</sub> NbO <sub>7</sub> . Auger transitions and XPS peaks are labeled accordingly. High resolution XPS spectra of (b) Ti 2p, (c) Nb 3d, (d) O 1s peaks. ....	44
Figure 31. UV-vis diffuse reflectance spectra for (a) KTiNbO <sub>5</sub> , K <sub>3</sub> Ti <sub>5</sub> NbO <sub>14</sub> , and CsTi <sub>2</sub> NbO <sub>7</sub> (b) exfoliated HTiNbO <sub>5</sub> , exfoliated H <sub>3</sub> Ti <sub>5</sub> NbO <sub>14</sub> , and exfoliated HTi <sub>2</sub> NbO <sub>7</sub> . ....	46
Figure 32: Diffuse reflectance UV-vis spectra for: (A) exfoliated HTiNbO <sub>5</sub> reassembled with HCl (●), LiOH (■), Na <sub>2</sub> SO <sub>4</sub> (◆), KCl (▲), and Cs <sub>2</sub> CO <sub>3</sub> (▼). Curves have been offset for clarity, and dashed lines were added to resolve band gap. (B) exfoliated HTiNbO <sub>5</sub> reassembled with BaSO <sub>4</sub> (●), La(NO <sub>3</sub> ) <sub>3</sub> (■), Mn(NO <sub>3</sub> ) <sub>2</sub> (◆), and Ni(NO <sub>3</sub> ) <sub>2</sub> (▲). ....	48
Figure 33. Hydrogen yields for nanosheet suspensions with 1% Pt and P25 with 1% Pt. ....	49

Figure 34. Hydrogen yields for P25, exfoliated HTiNbO <sub>5</sub> , and their composites with and without Pt. ....	51
Figure 35. UV-vis transmission spectra for (a) exfoliated HTiNbO <sub>5</sub> , (b) exfoliated H <sub>3</sub> Ti <sub>5</sub> NbO <sub>14</sub> , (c) exfoliated HTi <sub>2</sub> NbO <sub>7</sub> , (d) water and methylene blue, (e) rate law decoloration calculated from peak areas integrated between 400-800 nm in a-c. Correlation coefficients are provided in Table VII. ....	54

## ABSTRACT

Nanosheets are a class of materials defined by extreme anisotropy, typically with widths and thicknesses on the order of micrometers and nanometers, respectively. These materials are often synthesized from a bulk ceramic using soft-chemical processing to exfoliate individual sheets or clusters of sheets. Nanosheets are advantageous to applications dominated by surface chemistry, for example photocatalysis and electrochemistry. Titanate and niobate nanosheets have been extensively studied for these applications. The layered titanate-niobate nanosheets defined by the chemistries  $\text{HTiNbO}_5$ ,  $\text{H}_3\text{Ti}_5\text{NbO}_{14}$  and  $\text{HTi}_2\text{NbO}_7$  demonstrate photocatalytic behavior and interesting colloidal properties due to the liquid crystalline nature of nanosheet colloids. In this work, colloidal suspensions of single-layer titanate-niobate nanosheets were synthesized by exfoliation of the parent oxides. AFM showed single layer sheets to be between 1 and 2 nm thick, while XRD measurements showed a mean restacking distance between 2 and 2.5 nm. This restacking distance was shown to vary approximately 6 Å, presumably due to displacement of  $\text{H}_2\text{O}$  as suggested by FTIR. Nanosheet colloids displayed liquid crystalline behavior which could be eliminated in favor of new mesophases by reducing pH or by adding various salts such as  $\text{Na}_2\text{SO}_4$  in a process called reassembly. Adding acid resulted in gelled colloids defined by a sharp increase in viscosity below a critical pH of approximately 6. Rheological and diffraction measurements support a gelation mechanism resulting from the excluded volume effect and electrostatic repulsion between sheets. Adding a salt, however, resulted in flocculated nanosheets without an accompanying viscosity increase. Flocculation proceeds by some face-to-face restacking of neighboring nanosheets into tactoids which are themselves assembled into an edge-to-face 3D network. XRD patterns suggest tactoid thicknesses of 4-6 sheets. Powders prepared from assembled gels or floccules possessed unique mesostructures dependent on their colloidal processing as shown by BET and SEM. Assembled gels were found to be mostly mesoporous and dominated by small pores formed between restacked sheets, as indicated by average pore widths between 6-15 nm and large  $\text{N}_2$  adsorption hysteresis. Assembled floccules were significantly less mesoporous with essentially no adsorption hysteresis and larger pores averaging between 20-27 nm formed between linked tactoids. UV-visible adsorption spectra showed band gaps to be reduced from 4.1 eV for the parent phases to 3.6 eV for the exfoliated nanosheets. Reassembly with various cations raised the band gaps to 3.9-4.1 eV. Each chemistry demonstrated photocatalytic hydrogen production with a co-catalyst when exfoliated or reassembled. Exfoliated  $\text{H}_3\text{Ti}_5\text{NbO}_{14}$  producing the most hydrogen at a rate of 426  $\mu\text{mol H}_2/\text{hr/g}$ , whereas  $\text{HTiNbO}_5$  produced the least hydrogen. Assemblies of commercial  $\text{TiO}_2$  photocatalyst and exfoliated  $\text{HTiNbO}_5$  nanosheets were found to be highly photochemically active without an additional co-catalyst, producing 412  $\mu\text{mol H}_2/\text{hr/g}$ . Exfoliated nanosheets were also found to photocatalytically decompose methylene blue with exfoliated  $\text{H}_3\text{Ti}_5\text{NbO}_{14}$  demonstrating the highest decomposition rate. Photocatalytic behavior was therefore found to vary with nanosheet chemistry but not crystallographic motif.

## INTRODUCTION

The desire for high efficiency and environmentally benign energy sources has long prompted the development and study of novel materials. Photocatalysts in particular have received significant focus since the discovery of water splitting over  $\text{TiO}_2$  in the early 1970s.<sup>1,2</sup> Since then, applications have grown to include photocatalysts for chemical synthesis, bioremediation, solar energy conversion, and sensors.<sup>2,3,4,5</sup> Photocatalysis is the process where a photo-excited electron participates in or promotes a chemical reaction. If water is catalyzed, then the reaction  $2\text{H}_2\text{O} + \gamma \rightarrow 2\text{H}_2 + \text{O}_2$  requires a photon with an energy greater than 1.23 eV (photon wavelength of approximately 1  $\mu\text{m}$ ) to proceed.<sup>6</sup> No known materials are photocatalytic at this energy however. Instead, reported photocatalysts typically function in the near-UV to UV spectrum and with poor performance. Poor performance primarily results from a poor ability to generate electron-hole pairs, or the majority of photo-generated electron-hole pairs recombining due to an unfavorable environment for electron-hole separation. Therefore, the bulk of photocatalyst research is directed towards improving adsorption into the visible spectrum and improving efficiency. An assortment of techniques may be employed towards both ends. The formation of surface defect states may serve as electron or hole traps which complicate pair recombination. In a similar fashion, co-catalysts may be deposited on the photocatalyst surface to capture photo-generated electrons and promote a surface reaction.<sup>7,8,9</sup> Commonly used co-catalysts include NiO,  $\text{RuO}_2$ , Pt, and other precious metals.

The most promising photocatalysts employ multiple methods to promote catalysis and may be derived from novel materials such as nanoscrolls and nanosheets.<sup>10,9,11</sup> The latter have evolved from ceramic materials defined by a 2D layer structure which can be chemically processed to exfoliate and separate discrete sheets. Nanosheets intrinsically possess extremely high surface areas and anisotropy which facilitates rapid charge transfer from the bulk to reaction sites on the surface.<sup>12,13</sup> Moreover, their extreme anisotropy modifies the electronic structure through the phenomenon of quantum confinement which shifts the band edge relative to the bulk ceramic. Quantum confinement typically widens the bandgap; however, photocatalysis will be promoted if quantum confinement narrows the bandgap and enhances adsorption in the visible spectrum. Sarahan *et al.*<sup>14</sup> reported narrowed band gaps in exfoliated  $\text{K}_4\text{Nb}_6\text{O}_{14}$ , reporting band

gap energies of 3.56 eV for the parent phase, and 3.52 eV and 3.30 eV for tetrabutylammonium hydroxide (TBA) exfoliated nanosheets and nanoscrolls respectively. Allen *et al.*<sup>15</sup> reported a similar trend in layered titanates, reporting a band gap energy of 3.54 eV for  $K_2Ti_4O_9$  and 3.00 eV for the TBA exfoliated nanosheet. However, Sakai and others<sup>16,17</sup> have reported widened band gaps in exfoliated  $Ti_{0.91}O_2^{-0.36}$ , niobate, and titanate-niobate nanosheets.

To date, several nanosheet systems have been explored for photocatalysis and other applications. They include titanates<sup>15, 9, 18, 19, 20</sup>, niobates<sup>21, 22, 23, 24, 25, 26, 27, 28</sup>, layered double hydroxides and clays<sup>19, 29, 26</sup>, among many others. While these studies have driven our understanding of nanosheets and their photocatalytic behavior forward, few (if any) have explored the influence of chemistry among a mixed transition-metal system or the influence of motif on photochemical performance. The titanate-niobate nanosheets, whose parent phases are defined by the chemistries  $KTiNbO_5$ ,  $K_3Ti_5NbO_{14}$ , and  $CsTi_2NbO_7$ , are uniquely suited to explore both aspects. Each chemistry consists of metal-oxygen octahedra arranged in layers separated by A-site alkali atoms occupying the intersheet gallery. Polyhedra formed by Ti and Nb are arranged in doublets or triplets of edge-shared octahedra which are then corner shared. The three phases are therefore distinguished by the ratio of Ti to Nb and by the arrangement of metal-oxygen octahedra. Studying the photocatalytic behavior of each phase allows trends with chemistry or structure to be discerned.

Most studies report synthesizing nanosheets via soft-chemical exfoliation processes to form suspensions. The parent oxide is first ion-exchanged to incorporate protons into the intersheet gallery, followed by exfoliation with a cationic polymer such as tetrabutylammonium hydroxide. The resulting colloidal nanosheet suspensions demonstrate liquid crystalline behavior at appropriate volume loadings. In this state, the suspension may experience a nematic phase transitions in which nanosheets spontaneously align into semi-ordered domains upon the application of shear.<sup>30,17,9, 31,32,33</sup> Liquid crystalline nanosheet suspensions may then be processed to form nanosheet assemblies through the addition of acid, base, or salts.

The properties of layered oxides are highly dependent upon the interlayer cations and even interlayer water. Lucht *et al.*<sup>34</sup> used quantum simulations to show that the electronic structure of layered birnessite  $MnO_2$  may vary dramatically with different interlayer cations. By exfoliation and re-assembly, as well as by direct ion exchange<sup>24</sup>, one may alter the properties of layered oxides. Nanosheets may also be restacked with different nanosheets or assembled into

composites. Examples among the literature include assemblies of niobates,<sup>35, 36, 29, 37, 26, 38, 23, 39, 28</sup> titanates,<sup>31,19, 40,41</sup> layered double hydroxides,<sup>19</sup> graphene and graphene oxide,<sup>40,41</sup> aluminosilicate clays,<sup>29, 37, 26, 38</sup> and manganates.<sup>42, 43, 44</sup>

In general, the self-assembly of nanosheets may be classified as gelation or flocculation. Both mesophases have been extensively studied in the literature for various colloidal systems in addition to other nano-particle morphologies.<sup>45</sup> In this study, gelation refers to a high-viscosity colloid in which particle motion has been arrested, whereas flocculation is the apparent aggregation of particles without an increase in viscosity. Two microstructural schemes have been proposed to explain gelation in nanosheet systems. The first is the ‘house-of-cards’ structure composed of edge-to-face arranged sheet-like particles bound through electrostatic attraction and assembled into a long-range network.<sup>46, 47, 48, 49, 50</sup> The second is the excluded volume structure in which significant accumulation of charge to the nanosheet surface electrostatically repels particles and results in arrested motion.<sup>51, 52, 53, 54, 55, 56, 57, 58</sup> Several authors have reported the latter structure for gels in nanosheet systems.<sup>59, 37, 60, 61</sup>

In brief, nanosheet colloids may experience an isotropic to nematic phase transition in which the system transitions from a disordered state to a state where particles are arranged into domains of roughly parallel nanosheets. The phenomenon was explained first for rod-like particles by Onsager<sup>51</sup> who detailed the relationship between system entropy and the excluded volume. The excluded volume is the space surrounding a particle into which another particle is repelled and cannot enter. At high particle concentrations, the accumulated excluded volume results in the system attempting to minimize its free energy by maximizing free-volume entropy at the expense of translational and orientational entropy.<sup>51,52</sup> The result is arrested particle motion and particles adopting a parallel orientation. If instead the excluded volumes are expanded in a system of constant concentration, then a similar result may be achieved as shown in this study and for gels of other nanosheet systems.<sup>59, 37, 61, 60</sup>

Flocculation, however, is the result of an entirely different process. The most reasonable microstructure is the ‘house-of-cards’ structure composed of edge-to-face arranged particles bound through electrostatic attraction and assembled into a long-range network.<sup>46, 47, 48, 49, 50</sup> Gelled and flocculated mesophases therefore represent significantly different colloidal microstructures. Powders prepared from these assemblies should display microstructures reminiscent of the nanosheet colloid. The literature has provided no report specifically

investigating the relationship between colloidal behavior in nanosheets and the assembled nanosheet mesostructures.

Colloids of titanate and niobate nanosheets have been extensively studied in the literature.<sup>29, 37, 62, 26, 38</sup> However, colloidal mesophase behavior of exfoliated HTiNbO<sub>5</sub> has only been reported by Nakato *et al.*<sup>63</sup> who also demonstrated pH-induced gelation of exfoliated K<sub>4</sub>Nb<sub>6</sub>O<sub>17</sub> nanosheets.<sup>37</sup> Nakato proposed that the system gelled at low pH due to strong electrostatic repulsion between particles (the excluded volume microstructure). Nakato also noted flocculation with the addition of KCl but did not explore the phenomenon further. Colloidal behavior of the other layered titanate-niobates, K<sub>3</sub>Ti<sub>5</sub>NbO<sub>14</sub> and CsTi<sub>2</sub>NbO<sub>7</sub>, has not been investigated to date. The titanate-niobate nanosheets demonstrate behavior as photocatalysts,<sup>24, 64, 31</sup> electrochemistry,<sup>17, 33</sup> catalysts,<sup>65, 66</sup> and as dielectrics.<sup>67, 68, 69</sup>

Whereas these reports detail the extensive applications of titanate-niobate nanosheets, none endeavor to discuss their gelation and flocculation behavior and the resulting assemblies. This work reports how either gelation or flocculation may be induced in exfoliated titanate-niobate nanosheet suspensions by adjusting pH or by adding various salts or bases. Rheological studies were conducted to identify the critical pH below which gelation occurred. Flocculation was found to progress gradually with the addition of salts. X-ray diffraction (XRD) patterns of gelled and flocculated nanosheets were measured *in situ* to probe their short-range structure. Dry, powdered assemblies were formed from both mesophases by drying their respective suspensions. The mesostructures of gelled and flocculated assemblies were found to vary significantly, as documented by XRD, scanning electron microscopy (SEM), and specific surface area (BET) measurements. Gelled assemblies were found to be dominated by slit-like mesopores while flocculated assemblies possessed macropores. Photocatalytic and optical properties of liquid crystalline and assembled nanosheets were also explored. To that end, UV-vis spectra were collected on each chemistry's parent and exfoliated form to quantify changes in band gap and adsorption behavior. Optical adsorption spectra have also been collected on nanosheets assembled through gelation and various flocculants to quantify the band gaps dependence on the self-assembly process and the flocculating cation. Photochemical hydrogen production and methylene blue dye degradation tests were then performed to measure photocatalytic behavior of each chemistry. Lastly, a composite of commercial TiO<sub>2</sub> photocatalyst (P25) and exfoliated HTiNbO<sub>5</sub> was assembled and measured for hydrogen production. The composite was found to be

highly photochemically active without any additional co-catalyst. The ability to control the structure of titanate-niobate nanosheet assemblies is therefore demonstrated. Photocatalytic behavior of these nanosheets in their exfoliated form, assembled, and as composites is also demonstrated.

## EXPERIMENTAL

### A. Nanosheet Synthesis

Parent phases of  $\text{KTiNbO}_5$ ,  $\text{K}_3\text{Ti}_5\text{NbO}_{14}$ , and  $\text{CsTi}_2\text{NbO}_7$  were synthesized by reacting dry  $\text{TiO}_2$ ,  $\text{Nb}_2\text{O}_5$ ,  $\text{K}_2\text{CO}_3$ , and  $\text{Cs}_2\text{CO}_3$  powders. Starting materials were analyzed by XRD to confirm purity then blended in the appropriate molar ratios and vibratory milled in isopropanol (for  $\text{KTiNbO}_5$  and  $\text{K}_3\text{Ti}_5\text{NbO}_{14}$ ) or toluene (for  $\text{CsTi}_2\text{NbO}_7$  due to the solubility of  $\text{Cs}_2\text{CO}_3$  in isopropanol) for 60 minutes. Milled reagents were dried in air to recover powders, hand mixed for homogeneity, and calcined in a covered crucible to  $1100^\circ\text{C}$  for 24 hours. A sample of reacted powder was hand ground and analyzed by XRD. The reacted powders were then dispersed in isopropanol before vibratory milling for 60 minutes, dried, and recovered for the ion exchange step.

In a typical ion-exchange reaction, 0.5 g of reacted parent phase was dispersed in 50 ml 2N HCl, sealed in a 50 ml centrifuge tube, and ultrasonicated in a bath for 4 hours with frequent mixing to redispersed settled powder. The suspension was centrifuged and the supernatant replaced with 50 ml of fresh 2M HCl for an additional 4 hours ultrasonication. Suspensions were repeatedly centrifuged and rinsed with DI water until pH neutral. A small sample of the ion-exchanged suspension was analyzed by XRD to confirm a shift in the interlayer stacking distance caused by protonation. Tetrabutylammonium hydroxide was added to the protonated suspensions in a 1:1 TBA:H molar ratio (i.e. one mole TBA per mol  $\text{HTiNbO}_5$ , three moles TBA per mol  $\text{HTi}_5\text{NbO}_{14}$ , etc) and ultrasonicated for 4 hours. The exfoliated suspensions appeared opalescent when shaken or stirred. Suspensions were aged overnight allowing unexfoliated material to settle while nanosheets remained suspended. The supernatant was carefully decanted, preserved in a sealed tube, and stored in a dark environment. Small samples were dried onto zero background XRD holders and analyzed by XRD to confirm exfoliation. One milliliter samples were removed from each suspension and dried to  $500^\circ\text{C}$  in separate crucibles to measure solids concentration.

### B. Assembly

Gels were formed by adding 1 M HCl drop-wise to agitated suspensions until the viscosity increased dramatically or a desired pH was achieved. For XRD measurements of wet suspensions, gels were centrifuged to concentrate the solids then loaded into a zero background

holder with a 1 mm deep sample well. Moisture content in the suspended sample was not adjusted or controlled during the XRD measurement; however, samples remained wet and without signs of dry spots. Nanosheet films for XRD were prepared from gels by allowing small samples to dry in ambient conditions onto a zero background holder. Thermogravimetric analysis (TGA) samples were prepared by acidifying 1.5 ml samples to pH 1, centrifuging and rinsing with deionized H<sub>2</sub>O repeatedly, and allowing the centrifuged pellet to dry at 50° C. Dry assemblies were prepared by inducing gelation, centrifuging and rinsing until pH neutral, and allowing the final pellet to dry in air at 50° C.

Floccules were prepared by adding 1 M salt solution (Na<sub>2</sub>SO<sub>4</sub> in H<sub>2</sub>O unless stated otherwise) drop-wise while stirring until supernatants appeared clear. XRD measurements of wet suspensions were performed in the manner detailed previously. TGA samples were prepared by centrifuging and rinsing flocculated nanosheets five times and allowing the final pellet to dry at 50° C. Dry assemblies were prepared by adding salt until the supernatant appeared clear, centrifuging and rinsing with DI H<sub>2</sub>O three times and rinsing with isopropanol three times. The final centrifuged pellet was redispersed in isopropanol and boiled vigorously in a beaker covered with foil to produce fluffy powders. Dry gel and flocculated assemblies were hand milled and stored in static-free, sealed sample tubes in a dark, desiccated environment.

BET samples were prepared from the aforementioned gelled and flocculated powders. Fifty milligrams or more of powder was loaded into a dry sample tube of predetermined weight. Sample powders were further dried and de-aired at 150° C with flowing N<sub>2</sub> gas for 24 hours immediately before measurement. At least the minimum level of liquid nitrogen was maintained within the Dewar flask throughout measurement. BET samples prepared in this study were not de-gassed under vacuum or temperatures exceeding 150° C.

### **C. Photocatalysis**

For those samples with a co-catalyst, Pt nanoparticles were deposited at 1 weight percent by photocatalytic degradation of chloroplatinic acid (H<sub>2</sub>PtCl<sub>6</sub>•xH<sub>2</sub>O). Samples were suspended in de-oxygenated DI water, loaded into an Ar glove box, thoroughly mixed, and illuminated by a 500 W Xe lamp for one hour. The suspensions were centrifuged and rinsed with DI water thrice before photocatalysis measurements. All hydrogen evolution samples were suspended in solutions of 50 ml H<sub>2</sub>O and 2 ml glycerol (to scavenge photo-generated holes).<sup>70</sup>

Photocatalytically generated hydrogen was measured in a custom built recirculating gas system, wherein the sample was loaded into a sealed quartz vessel and stirred by a magnetic stir rod. The system was purged with N<sub>2</sub> until no atmospheric oxygen was detected by gas chromatograph (GC). Samples were illuminated by a Xe lamp operating at 500 W and otherwise shielded from ambient light. Evolved gasses were analyzed by GC.

Photocatalytic dye degradation was measured on 50 mg samples suspended in 50 ml of 150 μM methylene blue solution. Suspensions were allowed to equilibrate in the dark for at least one hour prior to measurements. Three ml of suspension was removed from the reaction vessel at specific times, loaded into a quartz cuvette, and analyzed for optical adsorption in transmission. First order kinetics were used to model decay behavior.

Band gaps and UV-Vis adsorption spectra were measured in diffuse-reflectance mode for powdered samples. A baseline spectrum was collected on a clean silicon wafer. Samples were then finely ground and dispersed in isopropanol by using an alumina mortar and pestle and deposited drop-wise onto the wafer for measurement. Suspended (exfoliated) samples were loaded into a quartz cuvette for transmission measurements. Baseline spectra were collected on quartz cuvettes loaded with the appropriate suspending fluid.

#### **D. Apparatuses**

XRD measurements were performed on a Bruker D8 Advance in coupled theta-2θ mode with Cu K<sub>α</sub> radiation. Samples were spun at 30 rpm. The X-ray source and detector were set to fixed-slit openings unless specified otherwise. SEM measurements were performed on a FEI Quanta 200F ESEM operating in high-vacuum mode with Au-Pd sputter coated samples. TGA measurements were performed on a TA Instruments SDT Q600 simultaneous TGA/DSC with flowing air atmosphere. FTIR was measured in transmission on thin powdered samples deposited onto a clean sapphire substrate. BET was performed with a Micromeritics Tristar II 3020 N<sub>2</sub> BET. Viscosity was measured on a TA Discovery rheometer in parallel-plate geometry with a 60 mm spindle and 1 mm separation gap. Steady-state shear rates were studied between 10<sup>5</sup>s<sup>-1</sup> - 10<sup>7</sup>s<sup>-1</sup> and at room temperature. XPS spectra were collected with a Phi Quantera SXM Scanning XPS/Microprobe with monochromatic Al k<sub>α</sub> radiation. Transmission and diffuse-reflectance UV-Vis spectra were collected on a Perkin Elmer Lambda 950 and 900, respectively.



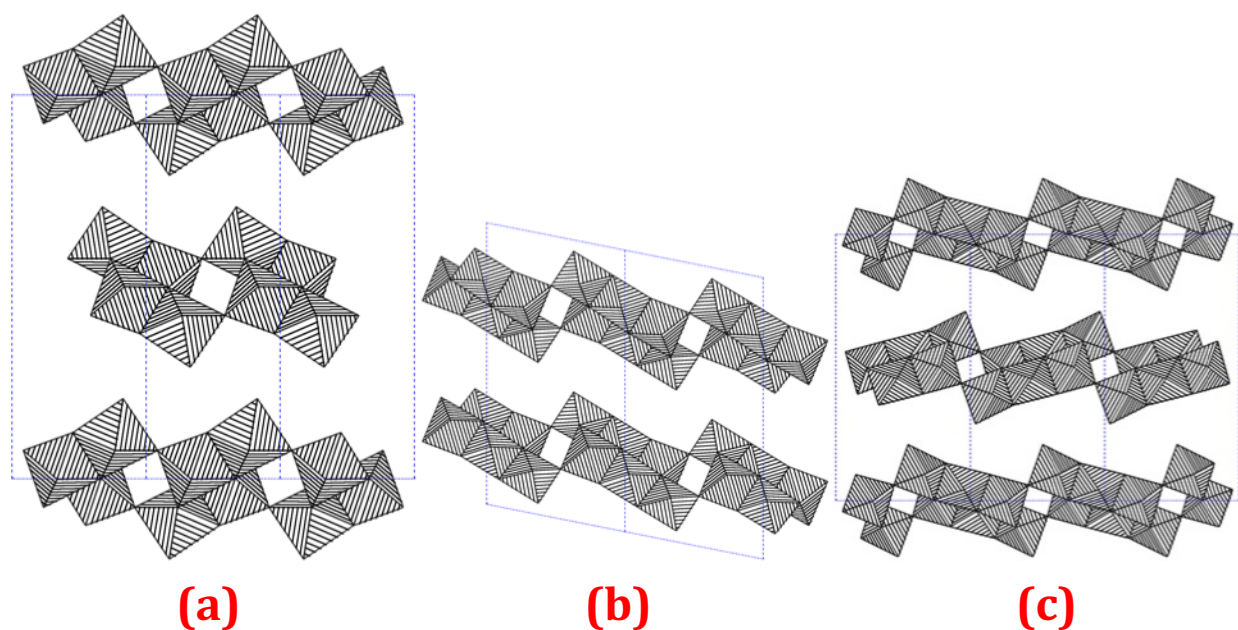
## RESULTS AND DISCUSSION

### A. Ion Exchange and Exfoliation

Unit cell data and illustrated crystal structures for each chemistry are provided in Table I and Figure 1a-c. Each chemistry consists of metal-oxygen octahedra arranged in layers separated by the A-site alkali atoms occupying the intersheet gallery. Ti and Nb are assumed to be randomly dispersed on the in-sheet metal sites. The polyhedra formed by Ti and Nb are arranged in doublets or triplets of edge-shared octahedra which are corner shared. Alkali ions compensate for the negative charge on each sheet. The three chemistries are therefore distinguished by the ratio of Ti to Nb and by the arrangement of metal-oxygen octahedra. Theoretical surface areas were calculated assuming full exfoliation into individual sheets (Table I).

**Table I: Structural Data For The Chemistries Employed In This Study. “Motif” Refers To The Grouping Of Edge-Shared (Ti,Nb)-O Polyhedra. Theoretical Specific Surface Area (tSSA) Considers Single Sheets As Flat Surfaces. Theoretical Specific Surface Charge (tSSC) Denotes The Charge Per Unit Area For One Sheet Only. Solids Loading Specifies Approximate Nanosheet Mass Per Volume As Measured Following Exfoliation.**

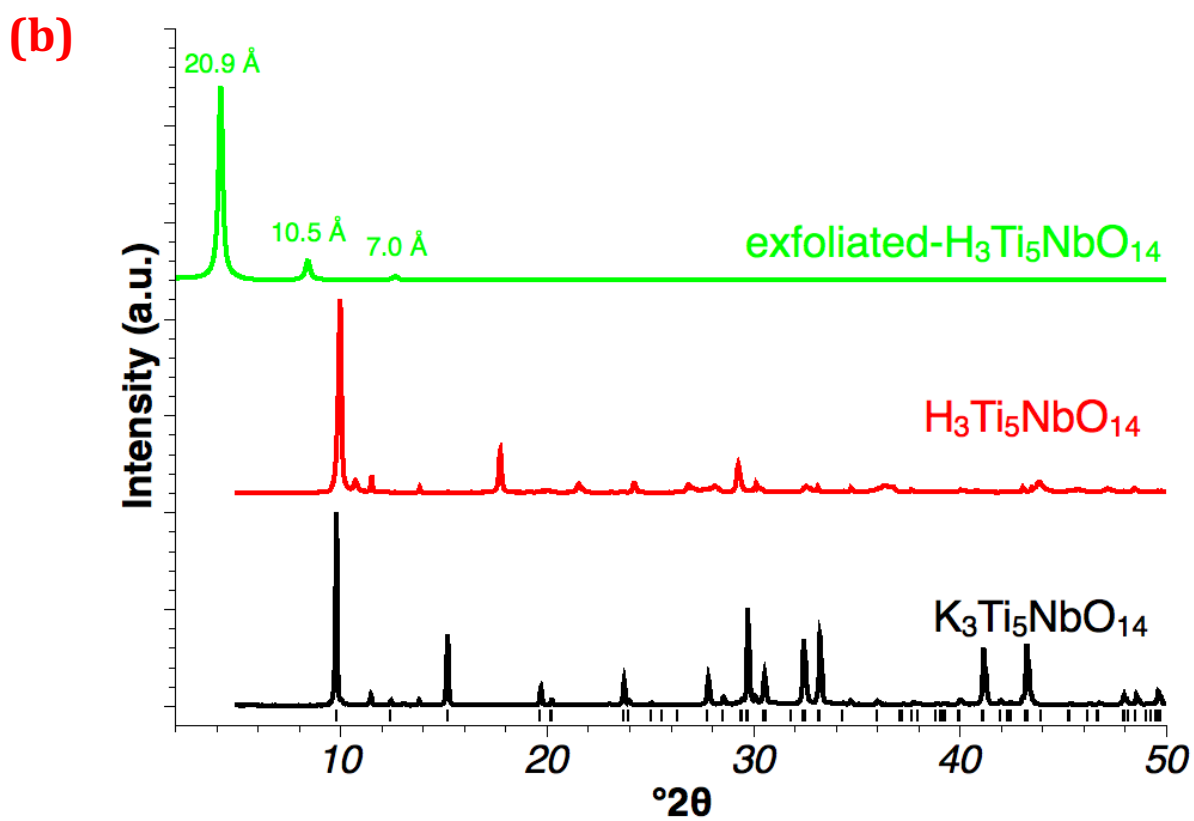
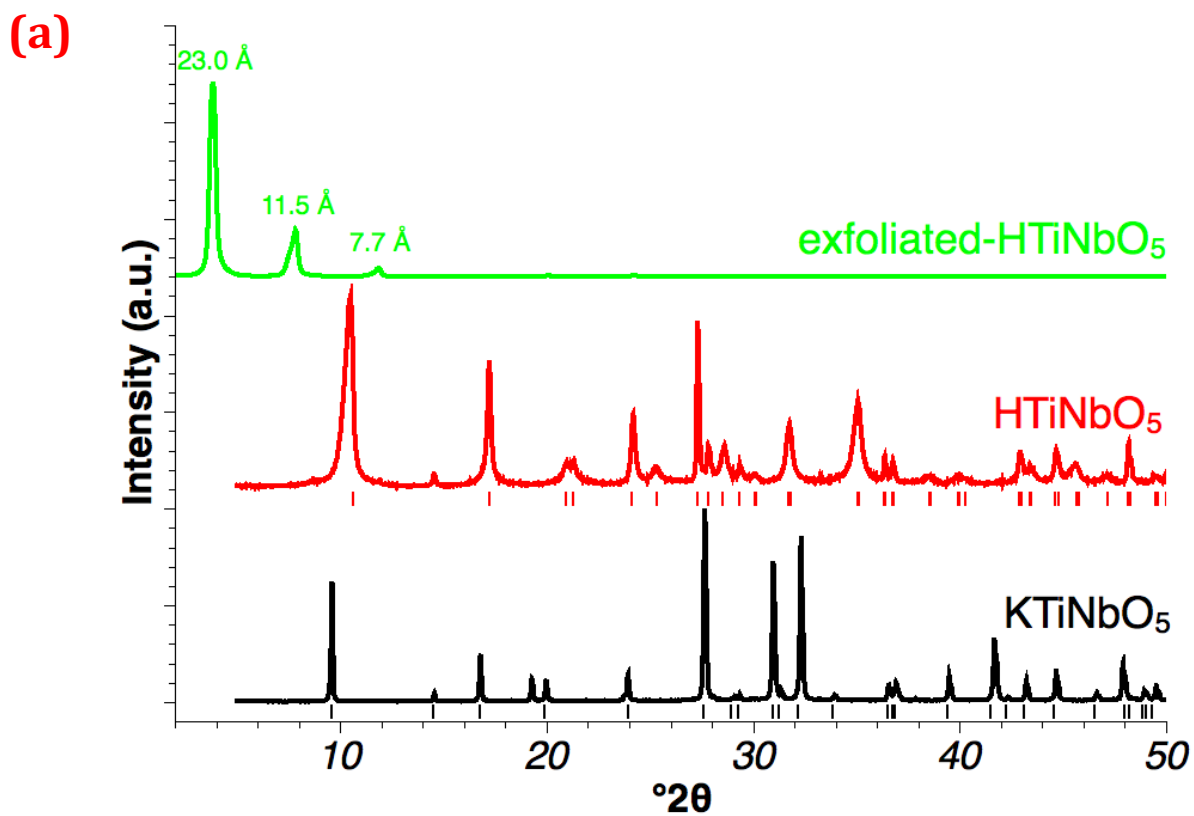
Chemistry	Space Group	a (Å)	b (Å)	c (Å)	tSSA (m <sup>2</sup> /g)	tSSC (C/g)	Concentration (mg/ml)
<b>KTiNbO<sub>5</sub></b>	Pnma	6.459	3.792	18.472	670	-436	6.2
<b>K<sub>3</sub>Ti<sub>5</sub>NbO<sub>14</sub></b>	C2/m	18.371	3.794	9.199	752	-519	2.2
<b>CsTi<sub>2</sub>NbO<sub>7</sub></b>	Pnam	9.326	18.412	3.798	707	-318	4.7



**Figure 1. Illustrated structures of (a)  $\text{KTiNbO}_5$ , (b)  $\text{K}_3\text{Ti}_5\text{NbO}_{14}$ , and (c)  $\text{CsTi}_2\text{NbO}_7$ . Interlayer alkali ions have been omitted for clarity. Dashed lines denote the unit cell.**

All three chemistries showed protonation following two ion exchange reactions and successful exfoliation with TBA, in agreement with earlier work.<sup>64, 31, 33, 68, 17</sup> XRD patterns demonstrating the protonation and exfoliation of  $\text{KTiNbO}_5$  are shown in Figure 2. Figure 2 shows only  $00l$  basal reflections from exfoliated nanosheet films due to restacking and preferred orientation that occurs during drying onto the sample holder, an effect also noted in earlier work.<sup>71</sup> Therefore, (001) reflections are only the result of the mean intersheet separation distance. Measured intersheet spacings varied between 2.0-2.5 nm, presumably due to varying amounts of interlayer water and the orientation of intercalated TBA. Atomic force microscopy (AFM) images shown in Figure 3 give nanosheet thickness between 1.2-1.7 nm, similar to the AFM profile measured by Osada *et al*<sup>68</sup>, corresponding to a nanosheet monolayer with a hydration shell. Fenter *et al* revealed the presence of adsorbed water extending 2.1 Å above the (110) surface of rutile and approximately 3 Å above the basal surface of muscovite.<sup>72</sup> Considering the high surface charges of the nanosheets employed in this study (see Table I) it is certain a similar water layer has been formed. Although the exact nature of the hydration layer was not explored, a rudimentary analysis reveals that a bare nanosheet approximately 10 Å thick flanked by two water layers 2-3 Å thick, totaling 14-16 Å, is feasible and explains the thicknesses measured by AFM. The proposed restacking scheme, presented in Figure 4, yields sheet thickness consistent

with XRD and AFM measurements. XRD measures the mean restacking distance between nanosheets, their hydration shells and intercalated TBA, which total approximately 23 Å. AFM measures the thickness of single sheets with only a hydration shell. Restacking behavior without additional processing was not found to vary significantly between the three chemistries used in the present study.



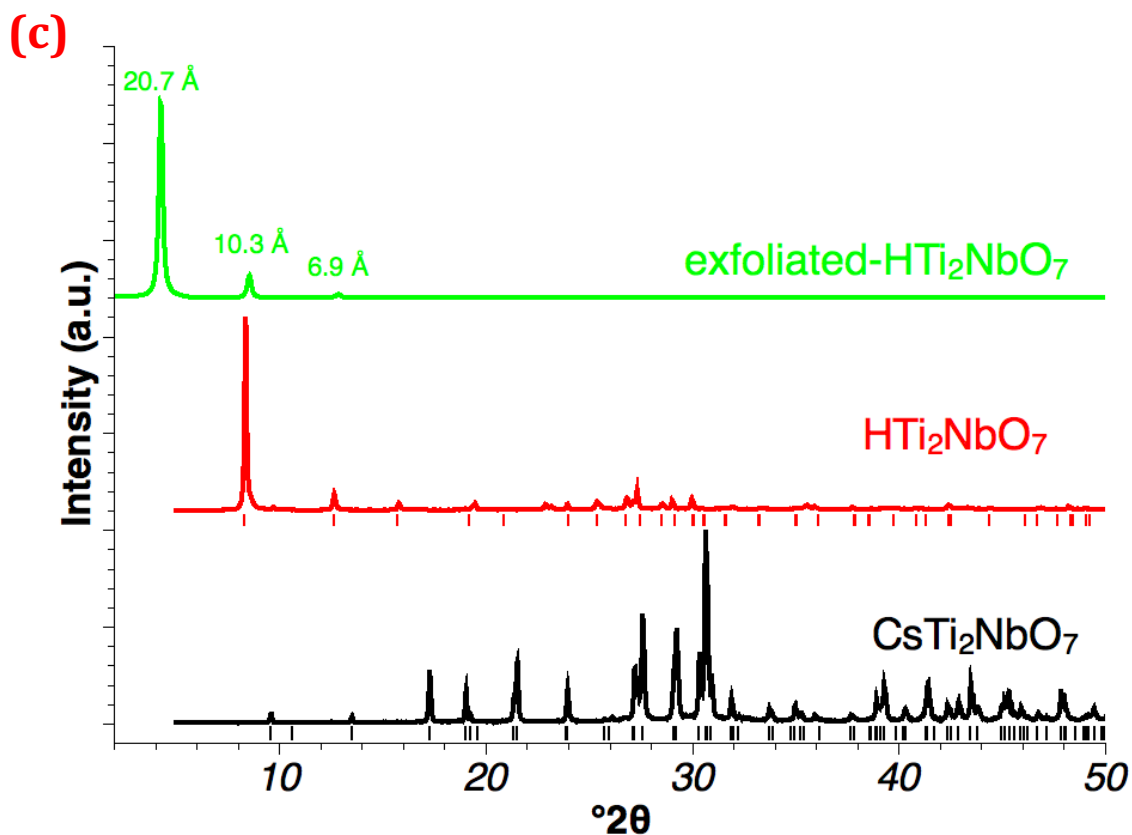


Figure 2. XRD patterns for (a)  $\text{KTiNbO}_5$ ,  $\text{HTiNbO}_5$ , and exfoliated  $\text{HTiNbO}_5$ ; (b)  $\text{K}_3\text{Ti}_5\text{NbO}_{14}$ ,  $\text{H}_3\text{Ti}_5\text{NbO}_{14}$ , and exfoliated  $\text{H}_3\text{Ti}_5\text{NbO}_{14}$ ; (c)  $\text{CsTi}_2\text{NbO}_7$ ,  $\text{HTi}_2\text{NbO}_7$ , and exfoliated  $\text{HTi}_2\text{NbO}_7$ . Exfoliated samples were dried at room temperature onto flat XRD sample holders. Peaks are denoted beneath patterns as tick marks from available PDF cards: ( $\text{KTiNbO}_5$ ) 04-009-8714, ( $\text{HTiNbO}_5$ ) 04-011-3432, ( $\text{K}_3\text{Ti}_5\text{NbO}_{14}$ ) 04-010-0680, ( $\text{CsTi}_2\text{NbO}_7$ ) 04-012-8410, and ( $\text{HTi}_2\text{NbO}_7$ ) 00-054-1154.

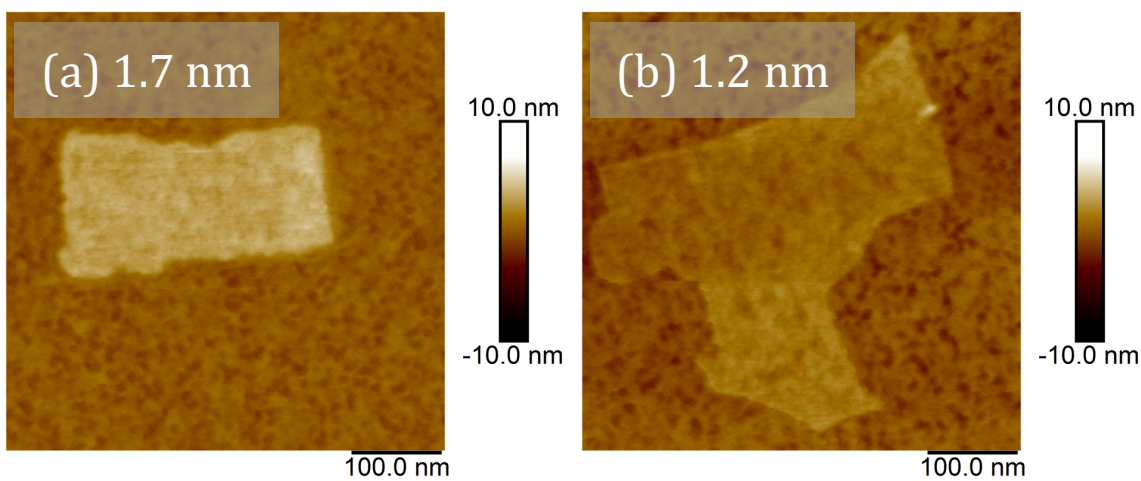
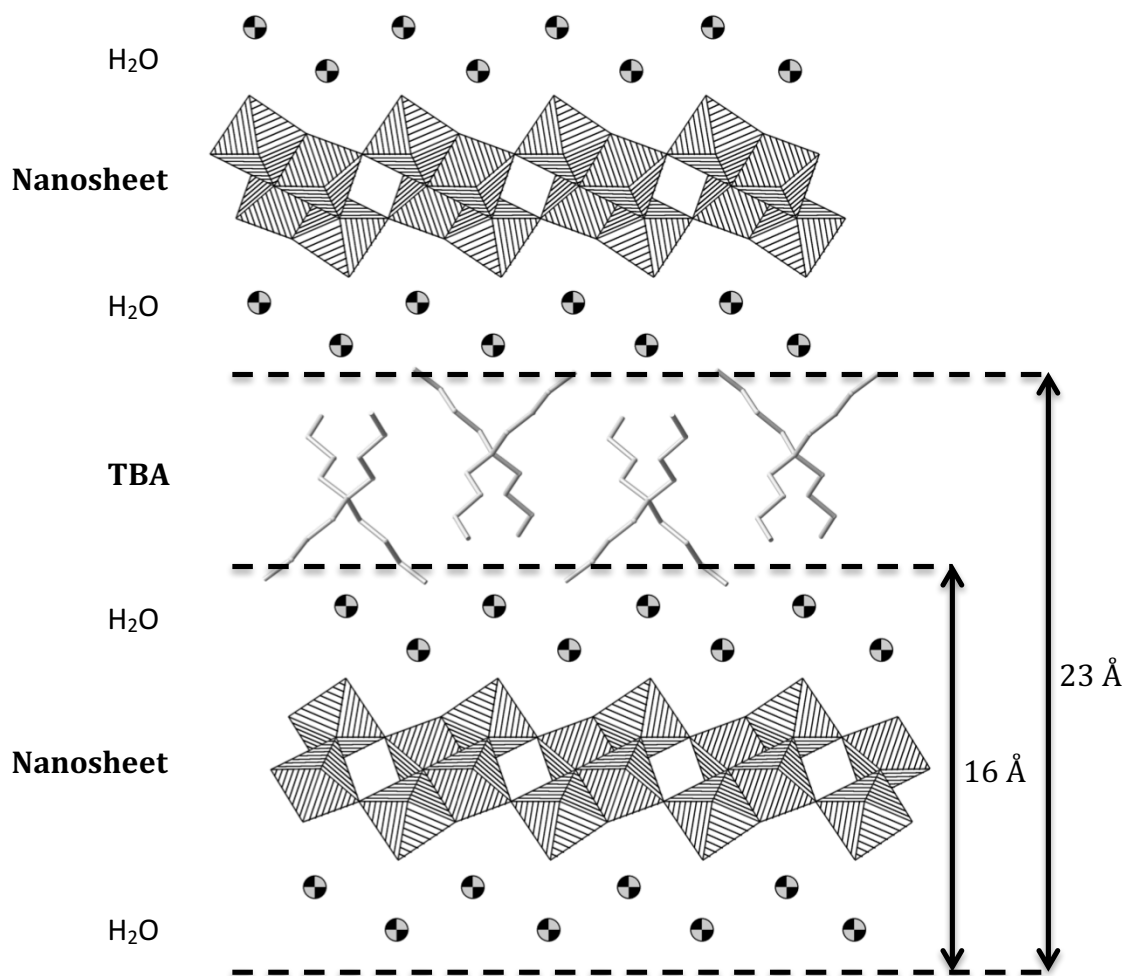


Figure 3. AFM images for exfoliated  $\text{HTi}_2\text{NbO}_7$  showing nanosheet thicknesses of (a) 1.7 nm and (b) 1.2 nm.



**Figure 4.** Proposed restacking scheme for the nanosheets studied using exfoliated HTiNbO<sub>5</sub> as a prototype, as measured by XRD and AFM. Ti/Nb-O octahedra are illustrated as polyhedra for clarity, however the model was constructed using space-filling atoms.

Heat treatment at 200° C and/or acid treatment to neutral pH reduced the  $d_{001}$  distance by approximately 5 Å, as shown by XRD patterns in Figure 5. Heat and reduced pH eliminate intergallery H<sub>2</sub>O and/or compress the hydration shell. Infrared spectra provided in Figure 6 show the C-H stretching bands centered at 2880 cm<sup>-1</sup> and 2970 cm<sup>-1</sup> remain following acid treatment, suggesting that TBA remains attached to the nanosheets throughout these processes. Intensities of the C-H stretching bands were reduced significantly for exfoliated HTiNbO<sub>5</sub> samples flocculated with Na<sub>2</sub>SO<sub>4</sub> and boiled in isopropanol. However, the broad -OH vibration band centered at 3350 cm<sup>-1</sup> suggests C-H stretching may be due to intercalated or latent alcohol used in the drying stage as discussed in detail later. Moreover, infrared spectra showed UV light to be inefficient for removing TBA by decomposition as shown by Figure 7. These results show

that intercalated TBA is not displaced during gelation, but may be displaced during flocculation. Exfoliated nanosheet suspensions appeared opalescent due to their liquid crystalline nature. Spontaneous alignment of particles under application of shear (e.g. stirring) results in interference as observed by the cross-polarized photograph in Figure 8. Inducing gelation or flocculation eliminated liquid crystalline behavior, and therefore these methods were pursued to facilitate assembly of the nanosheets with controlled mesostructures.

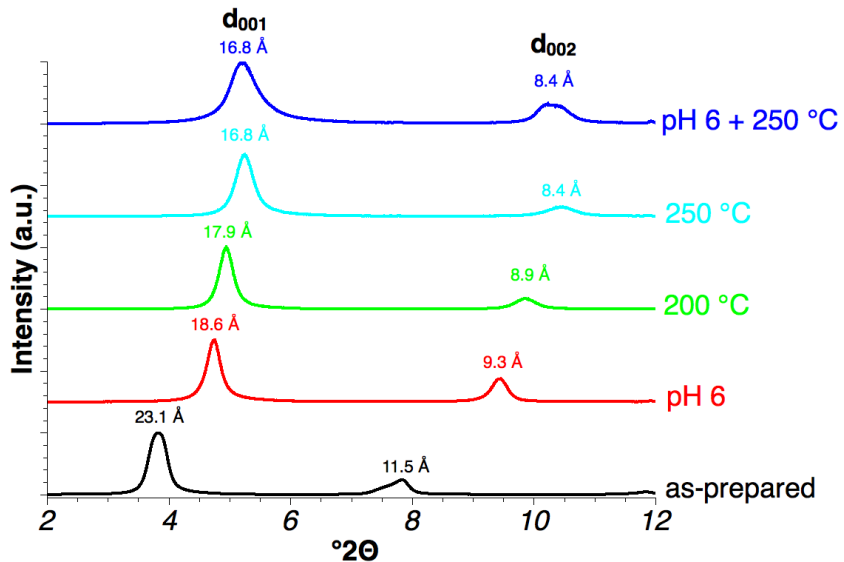


Figure 5. XRD patterns of exfoliated HTiNbO<sub>5</sub> dried as-prepared, following acid treatment to induce gelation at pH 6, heat treatment to 200 °C, 250 °C, and treated to pH 6 followed by 250 °C.

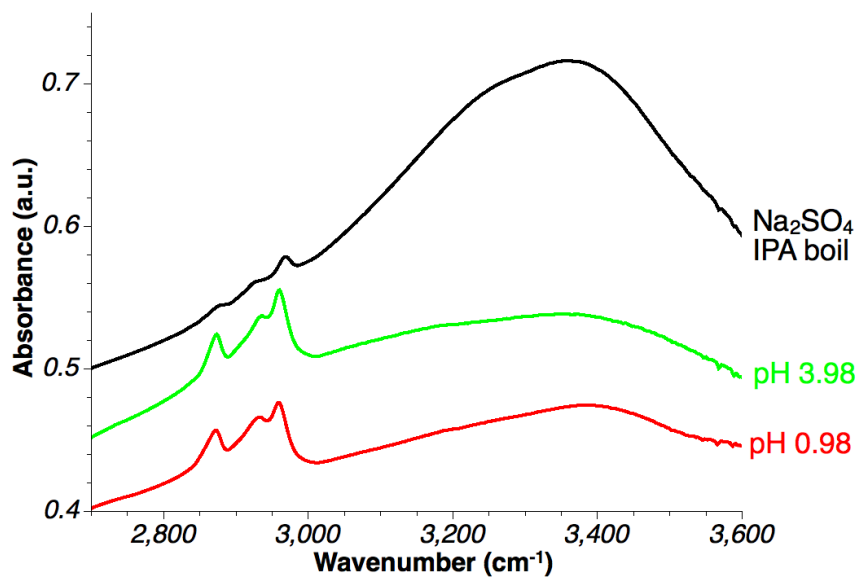


Figure 6. Infrared spectra for exfoliated HTiNbO<sub>5</sub>: Na<sub>2</sub>SO<sub>4</sub> flocculated and boiled in isopropanol, gelled with HCl at pH 3.98, and gelled at pH 0.98.

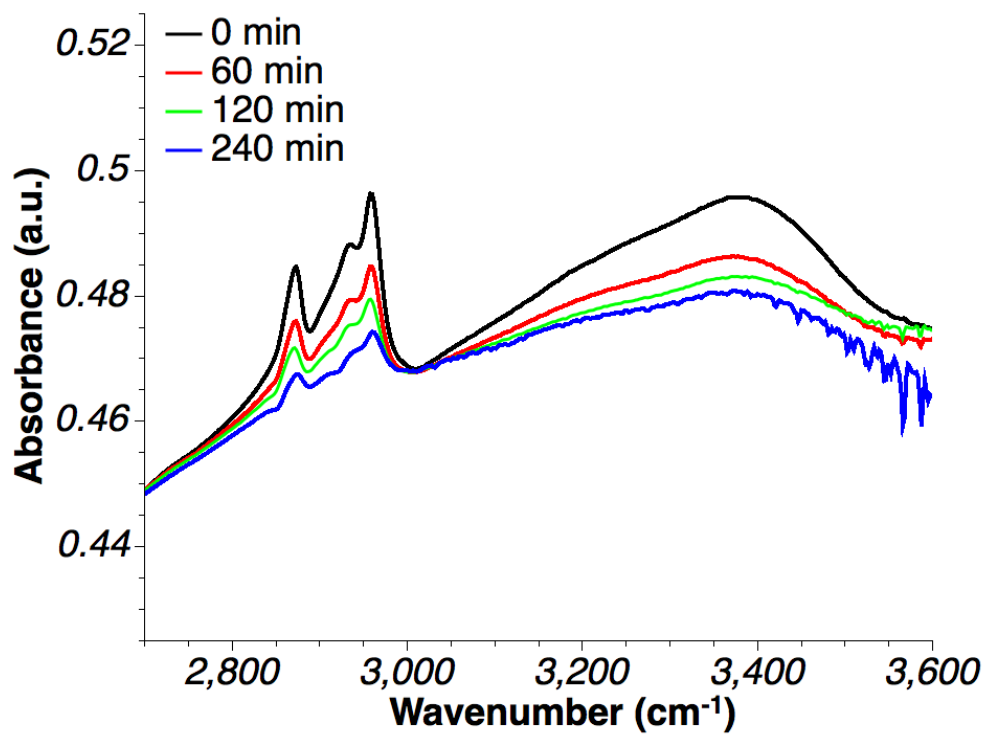


Figure 7. Infrared spectra for exfoliated HTiNbO<sub>5</sub> with intercalated TBA exposed to 500 W Xe lamp for 0, 60, 120, and 240 minutes.



Figure 8. Image of suspended exfoliated HTiNbO<sub>5</sub> under vigorous stirring as viewed through crossed polarizers. Image width corresponds to approximately 5 cm.

## B. Self-Assembly by Gelation and Flocculation

### 1. Gelation

Adding hydrochloric, nitric, or sulfuric acid to nanosheet suspensions resulted in a distinct viscosity increase and loss of liquid crystalline behavior below a critical pH. Figure 9 demonstrates the gelled system's resistance to flow compared to a flocculated suspension. The optical micrograph of gelled exfoliated HTiNbO<sub>5</sub> provided in Figure 10 shows a uniform dispersion of nanosheets in suspension. Viscosity curves provided in Figure 11 demonstrate the rapid onset of gelation below a pH of approximately 6. Further decreases in pH resulted in a maximum viscosity followed by a viscosity decrease without returning the system to a liquid crystalline state, a phenomenon also noted by Nakato.<sup>37</sup> Maximum viscosities were measured at pH values of 3.26, 4.50, and 4.02 for exfoliated HTiNbO<sub>5</sub>, H<sub>3</sub>Ti<sub>5</sub>NbO<sub>14</sub>, and HTi<sub>2</sub>NbO<sub>7</sub> nanosheets, respectively. These values roughly correlate with nanosheet concentration but not specific surface charge (See Table I). The suspension with the highest solids loading (exfoliated HTiNbO<sub>5</sub>), displayed a maximum viscosity at the lowest pH, whereas the lowest solids loading (exfoliated H<sub>3</sub>Ti<sub>5</sub>NbO<sub>14</sub>) displayed a maximum viscosity at the highest pH. To further test dependence on nanosheet concentration, an additional suspension of exfoliated HTiNbO<sub>5</sub> was diluted to one-fifth of the original solids loading and adjusted to various pH values. Considering one-fifth of the H<sub>3</sub>O<sup>+</sup> concentration at a pH of 3.26, the diluted suspension should display a maximum viscosity at approximately pH 3.96. Indeed, the maximum viscosity was observed near pH 4.00. The viscosity change is subtle at such low concentrations, however.

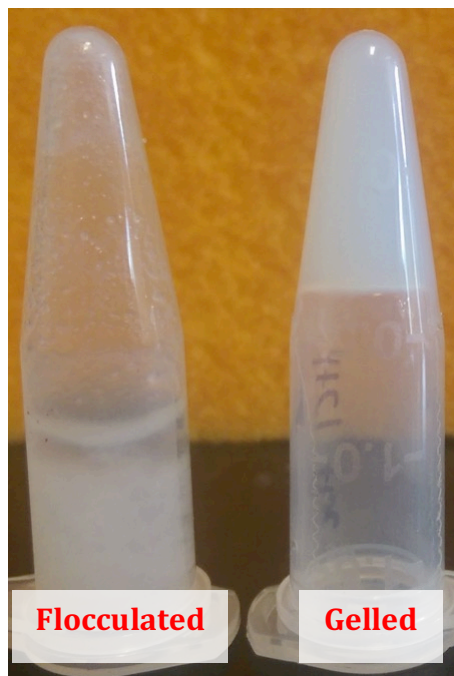


Figure 9. Image of exfoliated HTiNbO<sub>5</sub> flocculated with Na<sub>2</sub>SO<sub>4</sub> (left) and gelled with HCl (right). Tube height is approximately 3 cm. Concentration of Na<sub>2</sub>SO<sub>4</sub> was 0.04 M and pH of gelation was 1.5.

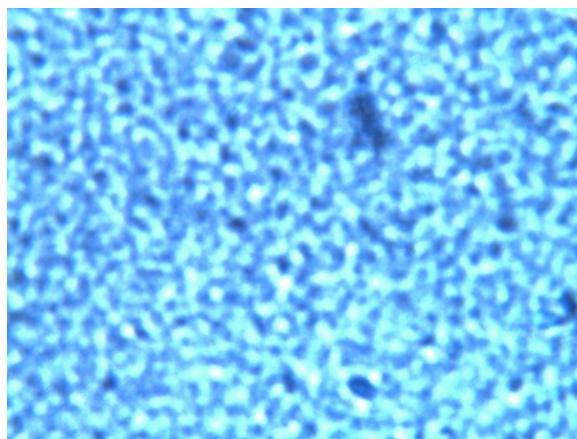


Figure 10. Optical micrograph of gelled exfoliated HTiNbO<sub>5</sub>. Image captured through a 40x objective and crossed polarizers.

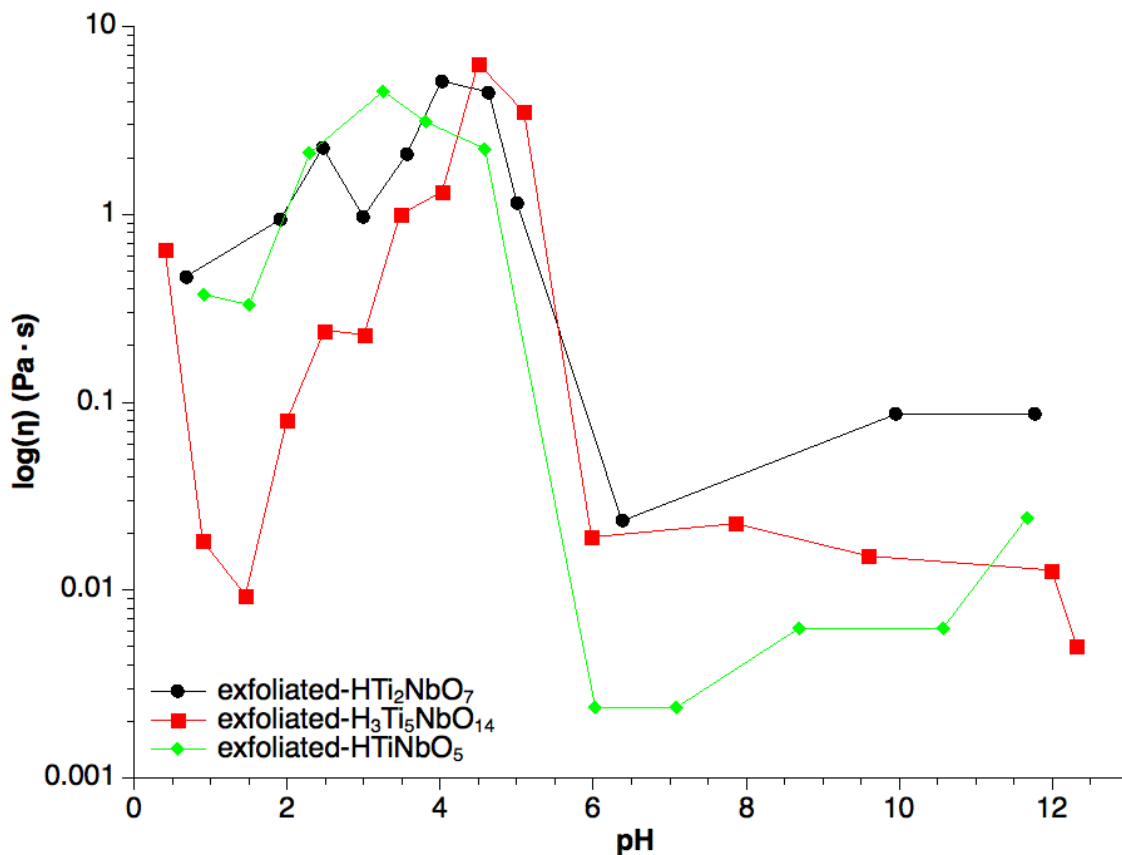
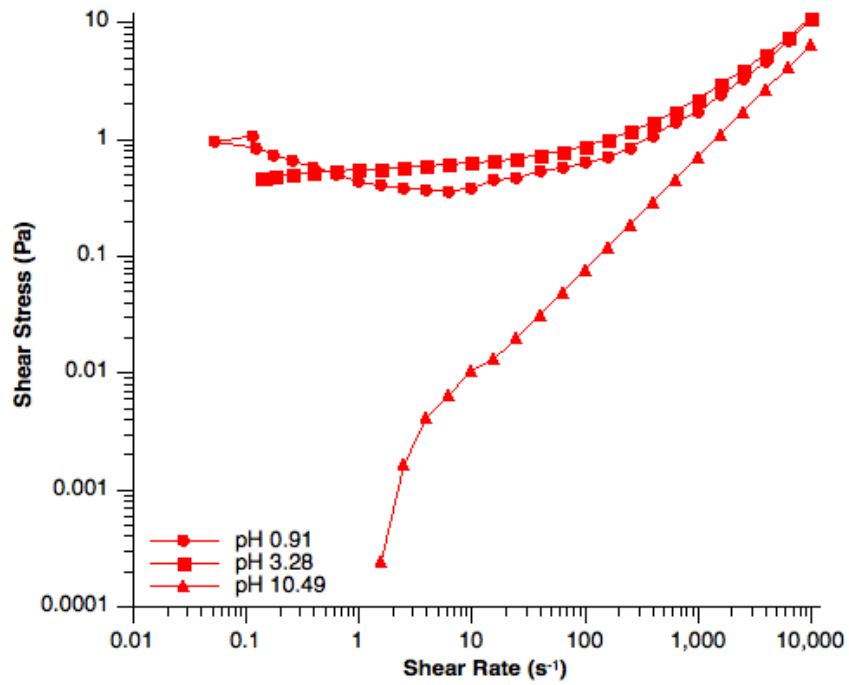


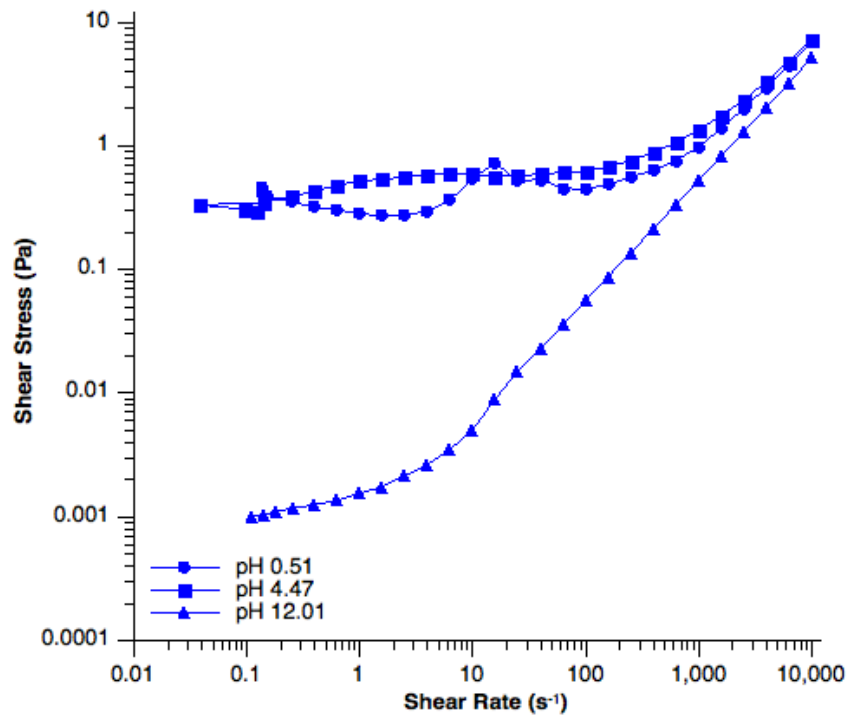
Figure 11. Viscosity at 0.1/s measured as a function of pH for suspensions of exfoliated HTiNbO<sub>5</sub> (diamonds), exfoliated H<sub>3</sub>TiNb<sub>5</sub>O<sub>14</sub> (squares), and exfoliated HTi<sub>2</sub>NbO<sub>7</sub> (circles).

Shear-stress viscosity curves were measured for nanosheet suspensions as prepared at high pH, pH at maximum viscosity, and at low pH, as shown in Figure 12. As-prepared nanosheets demonstrate weak connectivity as evidenced by low stresses throughout the measured shear-rate range. Further, the spontaneous arrangement of nanosheets into a discotic liquid crystalline mesophase at higher shear rates results in a linear relationship between stress and shear. Gelled nanosheets demonstrate high stresses throughout the measured shear-rate range due to intersheet connectivity and the same linear relationship at high shear rates. Measurements on the lowest pH gels revealed a discontinuity at approximately 10/s. This feature might be explained by shear banding, a rheological phenomenon due to competing colloidal interactions.<sup>73</sup>

(a)



(b)



(c)

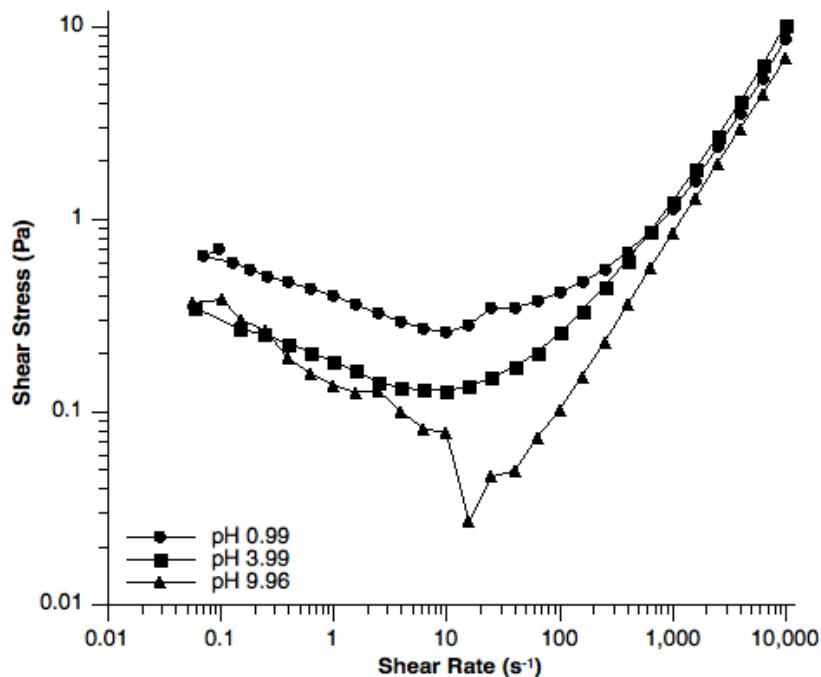


Figure 12. Stress curves measured as functions of shear rate and pH for suspensions of exfoliated HTiNbO<sub>5</sub> (a), exfoliated H<sub>3</sub>Ti<sub>5</sub>NbO<sub>14</sub> (b), and exfoliated HTi<sub>2</sub>NbO<sub>7</sub> (c).

X-ray diffraction patterns of wet suspensions was used to find evidence of nanosheet re-stacking in the suspensions. None of the gelled nanosheets investigated in this study displayed short-range restacking while in suspension as shown by the absence of (001) diffraction peaks in Figure 13. In-sheet  $hk0$  reflections are observed in Figure 13 since nanosheets are sufficiently large in lateral dimension to allow diffraction from in-plane crystallinity. The  $d_{002}$  and  $d_{022}$  for exfoliated H<sub>3</sub>Ti<sub>5</sub>NbO<sub>14</sub>, and  $d_{200}$  and  $d_{202}$  for exfoliated HTi<sub>2</sub>NbO<sub>7</sub> have negligible intensities based on diffraction patterns for the ion-exchanged phases, however the  $d_{200}$ ,  $d_{020}$ , and  $d_{220}$  for exfoliated HTiNbO<sub>5</sub> are expected to be observed. The broad hump between 10-55° 2 $\theta$  was the result of water scattering in the wet gel. Water scattering overwhelmed many diffracted intensities at the low solids concentrations used for these measurements.

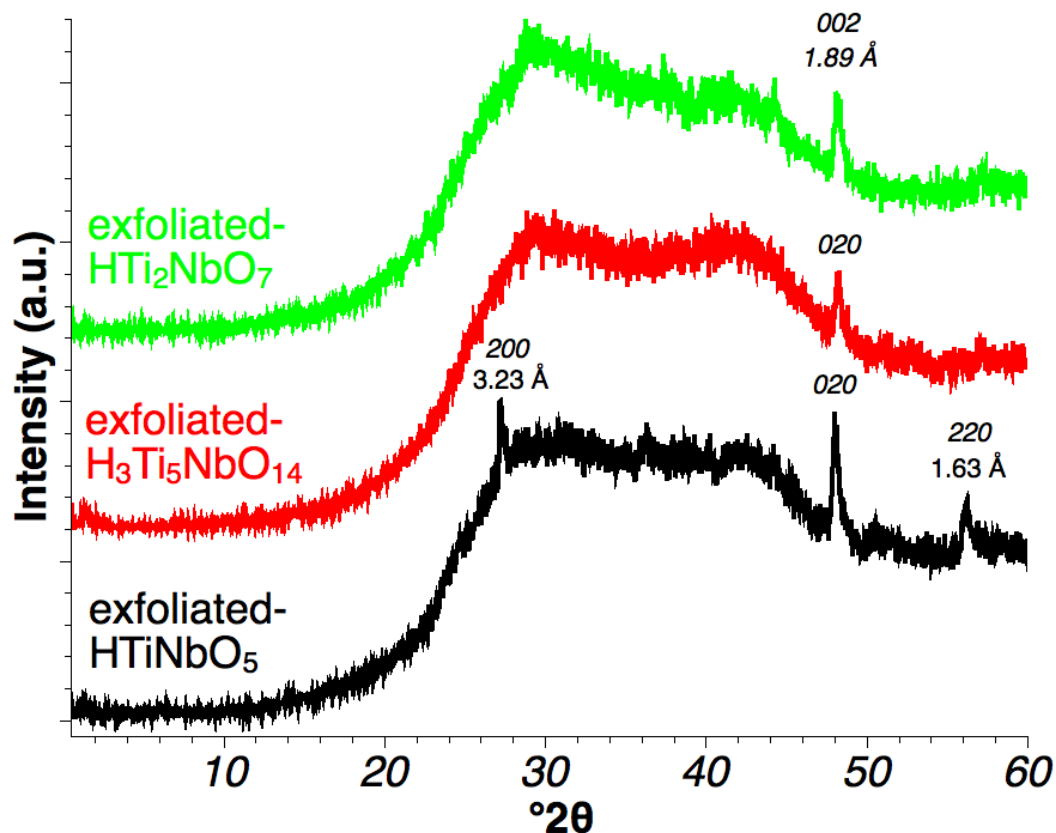


Figure 13. XRD patterns of wet suspensions of exfoliated  $\text{HTiNbO}_5$ , exfoliated  $\text{H}_3\text{Ti}_5\text{NbO}_{14}$ , and exfoliated  $\text{HTi}_2\text{NbO}_7$  gels. Suspension pH was approximately 1.5. Measured in reflection geometry with variable slit source and detector. D-spacings and Miller indices are labeled for observed reflections in accordance with the peak indices of the parent phases.

Gelled nanosheets restacked when dried as a film resulting in diffraction patterns containing only (001) reflections with locations that varied with pH, as shown in Figure 15- Figure 17. Preferred orientation implies sheets were repelled in suspension and could freely lay flat during drying. For exfoliated  $\text{HTiNbO}_5$ , shown in Figure 15, the  $d_{001}$  decreased by  $4.5 \text{ \AA}$  when pH was adjusted from 11 to pH 6, followed by another decrease of  $8 \text{ \AA}$  when pH was reduced from 6 to pH 0.99. Patterns measured at pH lower than 3.76 show systematically absent even- $d_{001}$  reflections. The change in interlayer configuration which occurred below pH 3.76 can be interpreted as ordering of neighboring nanosheets into coherently diffracting stacks, in other words, crystallization. Using the Scherrer formula,  $\tau = 0.89\lambda/\beta\cos(\theta)$ <sup>74, 75</sup>, the estimated thickness of these coherently diffracting stacks is  $79 \text{ \AA}$  or 7-8 sheets. In effect, sheets no longer restacked randomly but instead adopted a periodic restacking structure with an intersheet

distance ( $d_{001}$ ) of 10.6 Å by pH 0.99. Systematically absent even- $d_{001}$  reflections could only result from a recrystallized sample. Elucidating the exact behavior of these nanosheets at low pH was not a goal of the present study but should be considered for future work.

The decrease in interlayer spacing and crystallization could be interpreted as the expulsion of water and/or TBA from the interlayer gallery. At low pH, hydronium ( $H_3O^+$ ) ions adsorb onto the nanosheet and screen the negative surface charge, thereby eliminating the attractive potential among the sheet, water, and TBA. If TBA is ignored, then the number density of water ( $\rho_{H_2O,3D} = 33.4 \frac{H_2O}{nm^3}$ , where  $\rho_{H_2O,1D} = \rho_{H_2O,3D}^{\frac{1}{3}} = 3.2 \frac{H_2O}{nm}$ )<sup>72</sup> reveals that a decrease of 12.5 Å corresponds to a thickness of approximately 4 water molecules, behavior similar to the swelling of clays. Extending this argument reveals that 10 moles of  $H_2O$  are expelled per mole  $HTiNbO_5$  when decreasing the pH from 11 to 0.99. Applying this procedure to exfoliated  $HTi_2NbO_7$  reveals 6 moles of  $H_2O$  are expelled per mole  $HTi_2NbO_7$  when pH is reduced from 11 to 0.99. This behavior may be the result of changes in the surface functional groups because of the pH-dependent surface charge. For example, the rutile form of  $TiO_2$  is known to present a range of Ti-O and Ti-OH protonation states as the pH varies.<sup>72</sup> TGA measurements collected on exfoliated  $HTiNbO_5$  gelled at pH 1 revealed 13% mass loss between 100-800° C, as shown by Figure 14. This mass loss corresponds to approximately 1.8 moles  $H_2O$  per mol  $HTiNbO_5$ . This is greater than what's required for complete surface charge compensation (1 mol  $H_3O^+$ /mol  $HTiNbO_5$ ) suggesting that additional labile water is present. TGA measurements for gelled  $H_3Ti_5NbO_{14}$  and  $HTi_2NbO_7$  revealed mass losses corresponding to 4.5 and 2.5 moles  $H_2O$  per mole of nanosheet respectively. Both possessed approximately 1.5 additional moles of water than the minimum required to fully compensate for surface charge (assuming  $H_3O^+$ ). Flocculated nanosheets possessed similar, albeit slightly lesser, quantities of adsorbed water. TGA data on gelled and flocculated nanosheets shows that a significant quantity of water is bound to the nanosheets regardless of the colloidal processing technique. The data is summarized in Table II.

Restacking behaviors with pH for exfoliated  $H_3Ti_5NbO_{14}$  and exfoliated  $HTi_2NbO_7$  (Figure 15 and Figure 16 respectively) are more complex than for exfoliated  $HTiNbO_5$ . For both chemistries, the peak designated as the (001) shifted to shorter d-spacing with decreased pH. However, scattering at lower angles increased significantly below pH 5 for exfoliated  $H_3Ti_5NbO_{14}$  and below pH 3 for exfoliated  $HTi_2NbO_7$ . By pH 1, a new peak at approximately 36 Å had developed without corresponding higher-order peaks. This behavior suggests that low pH

modifies the nanosheet surface in some way to induce a complex restacking scheme which cannot be simply explained as water expulsion.

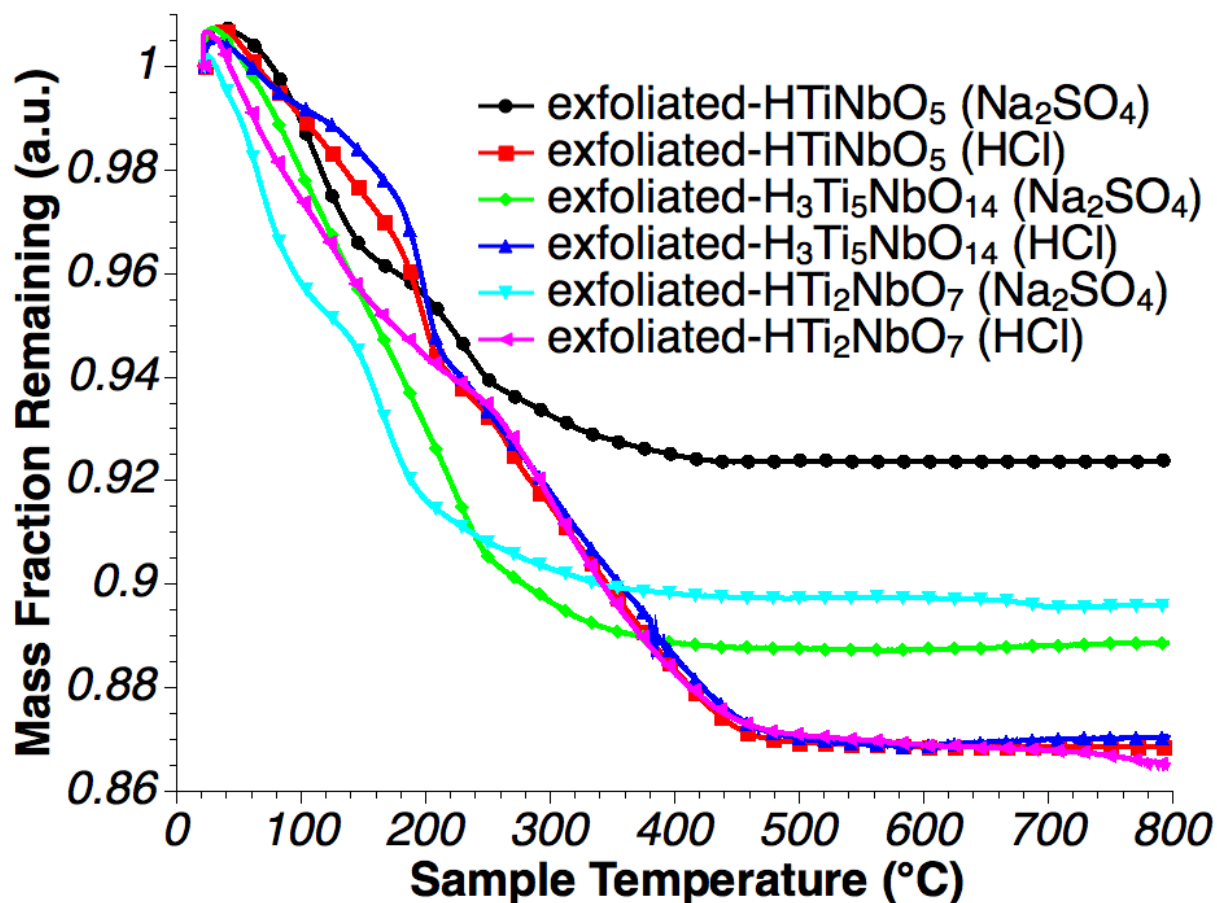


Figure 14. TGA curves for exfoliated HTiNbO<sub>5</sub>, exfoliated H<sub>3</sub>Ti<sub>5</sub>NbO<sub>14</sub>, and exfoliated HTi<sub>2</sub>NbO<sub>7</sub> reassembled with Na<sub>2</sub>SO<sub>4</sub> or HCl.

Table II: Summarized TGA Data For Exfoliated HTiNbO<sub>5</sub>, Exfoliated H<sub>3</sub>Ti<sub>5</sub>NbO<sub>14</sub>, And Exfoliated HTi<sub>2</sub>NbO<sub>7</sub> Reassembled With Na<sub>2</sub>SO<sub>4</sub> Or HCl.

Assembling Species	Mol <sub>H<sub>2</sub>O</sub> /mol <sub>nanosheet</sub>		
	HTiNbO <sub>5</sub>	H <sub>3</sub> Ti <sub>5</sub> NbO <sub>14</sub>	HTi <sub>2</sub> NbO <sub>7</sub>
Na <sub>2</sub> SO <sub>4</sub>	1.12	4.42	2.10
HCl	1.77	4.46	2.48

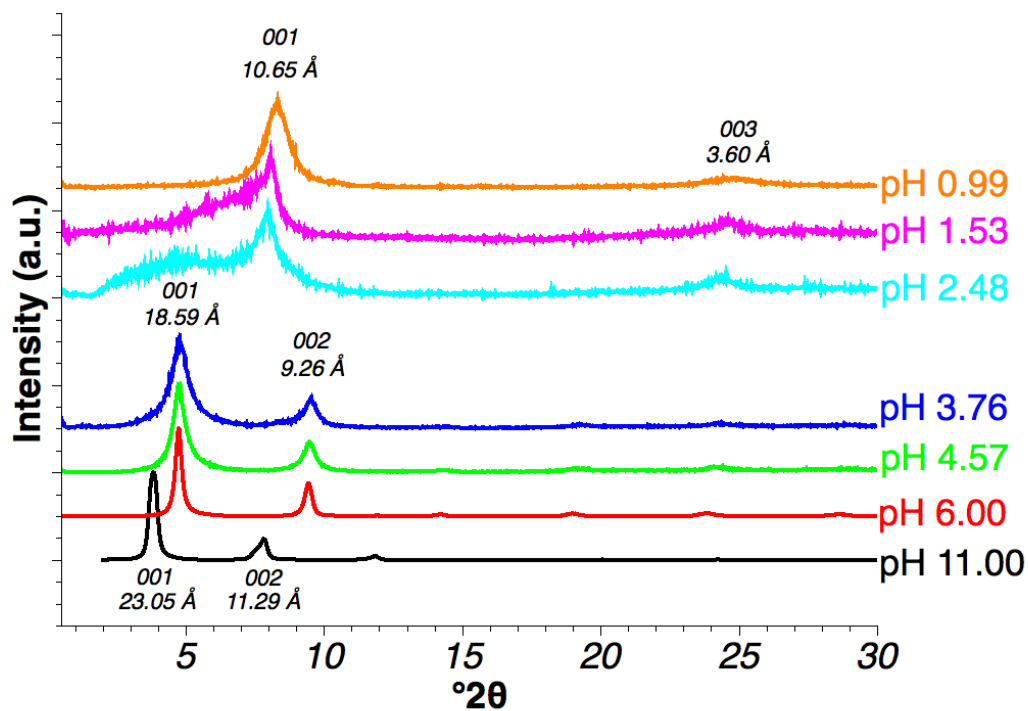


Figure 15. XRD patterns for dry films of exfoliated HTiNbO<sub>5</sub> treated to pH 11, pH 6.00, 4.57, 3.76, 2.48, 1.53, and 0.99. Measured in reflection geometry.

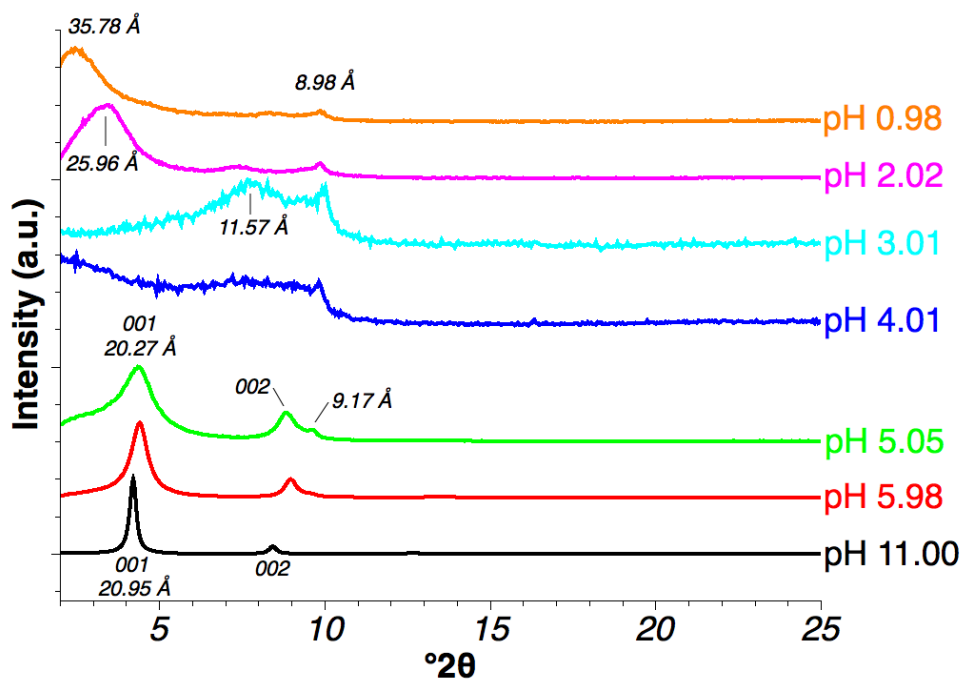


Figure 16. XRD patterns for dry films of exfoliated H<sub>3</sub>Ti<sub>5</sub>NbO<sub>14</sub> treated to pH 11, 5.98, 5.05, 4.01, 3.01, 2.02, and 0.98.

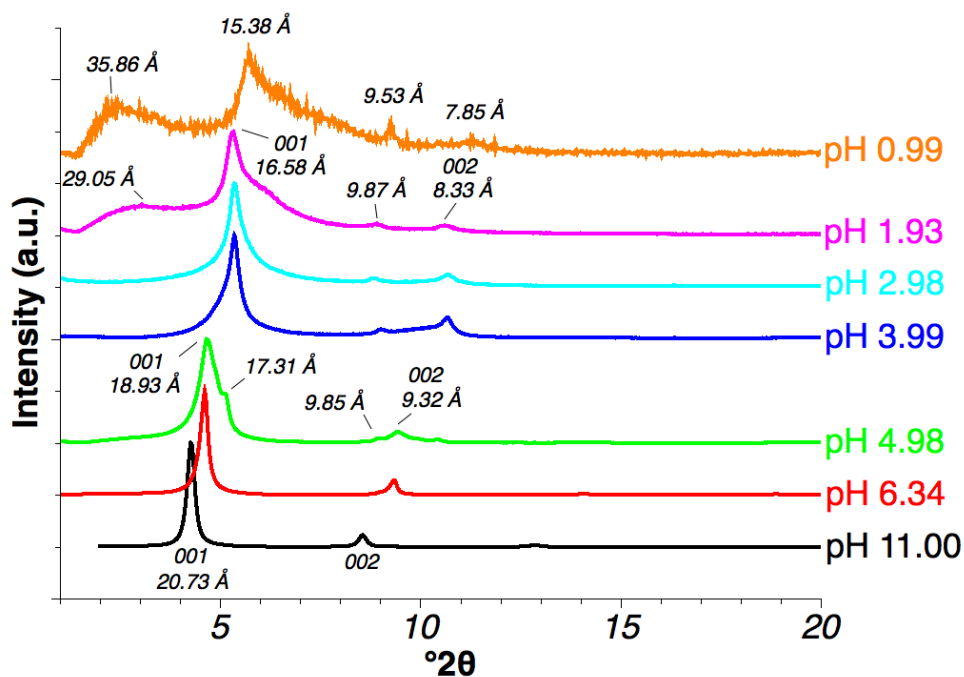
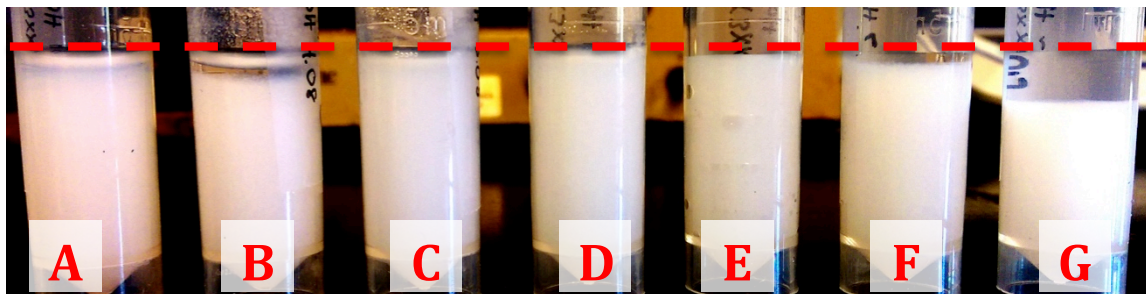


Figure 17. XRD patterns for dry films of exfoliated HTi<sub>2</sub>NbO<sub>7</sub> treated to pH 11, pH 6.34, 4.98, 3.99, 2.98, 1.93, and 0.99.

The data presented in Figure 9-Figure 17 provide strong evidence for gel microstructures similar to those noted in clay and niobate systems.<sup>25, 37, 26</sup> As opposed to the ‘house of cards’ microstructure formed through electrostatic attraction, strong electrostatic repulsion and the formation of an electric double layer bound to the nanosheet surface (i.e. the excluded volume) results in a mesophase transition at low pH. Overlapping double layers result in a jammed microstructure and arrested particles thereby producing a gel.<sup>59, 76, 60, 61, 37, 51</sup> Moreover, shear-stress curves reveal increasing stress at higher shear rates. If the sheets were assembled into a house-of-cards network, high shear rates would reduce network connectivity and result in lower stress. Increasing stress is likely due to electrostatically repelled sheets being forced into one another.

However, this explanation alone cannot explain why gelled nanosheets settle spontaneously (Figure 18a-g), can be centrifuged out of suspension, or form flocs when extremely dilute. It is speculated that nanosheet gels are instead the result of two contributions. First, the formation of an expansive double layer bound to the nanosheet surface leads to arrested particles through the previously defined mechanism. Second, the expansive double layer shifts the minimum energy (equilibrium) distance significantly far away from the nanosheet surface

resulting in microstructures nonetheless bound through electrostatic forces. Sufficiently low pH will compress the double layer, unjam the microstructure, and decrease viscosity thereby allowing electrostatically linked particles to settle.



**Figure 18.** Images of exfoliated  $\text{H}_3\text{Ti}_5\text{NbO}_{14}$  treated with HCl to pH 4.90 (a), 4.08 (b), 3.05 (c), 1.97 (d), 1.36 (e), 0.90 (f), and 0.38 (g) having been allowed to settle for 24 hours. The volume of each sample was approximately 4.5 ml. Dashed line denotes approximate liquid height.

## 2. Flocculation

The addition of non-acidic salts to nanosheet suspensions resulted in a system significantly different than a gel, as shown by optical images in Figure 19 and Figure 20. Flocculation begins immediately upon the addition of salt and proceeds gradually until all nanosheets have flocculated. A concentration of 0.034M  $\text{Na}^+$ , for example, was found to complete flocculation regardless of the chemistry or of the sodium salt used. It should be noted that this concentration of salt is less than that predicted for complete screening by the DLVO theory (approximately 0.1M).<sup>77</sup> Tested salts include LiOH,  $\text{Li}_2\text{CO}_3$ ,  $\text{Li}_2\text{SO}_4$ , NaOH,  $\text{Na}_2\text{SO}_4$ , KCl,  $\text{Cs}_2\text{CO}_3$ ,  $\text{BaSO}_4$ , and the nitrates of La, Ni, and Mn. At similar concentrations as Na salts, KCl was found to flocculate exfoliated  $\text{HTiNbO}_5$  and exfoliated  $\text{HTi}_2\text{NbO}_7$ , but not exfoliated  $\text{H}_3\text{Ti}_5\text{NbO}_{14}$ .  $\text{Cs}_2\text{CO}_3$  was found to be ineffective as a flocculating agent (as discussed in the following section). Flocculation did not result in a viscosity change until the flocculates were concentrated following centrifugation. X-ray diffraction patterns of flocculated systems show characteristic  $hk0$  peaks corresponding to in-sheet reflections and a broad reflection at low angle roughly corresponding to a (001) spacing of 18 Å. Figure 21 shows these patterns.



**Figure 19.** Image of exfoliated HTiNbO<sub>5</sub> flocculated with Na<sub>2</sub>SO<sub>4</sub>. Image corresponds to a length of approximately 5 cm. No additional processing had been performed after flocculation.

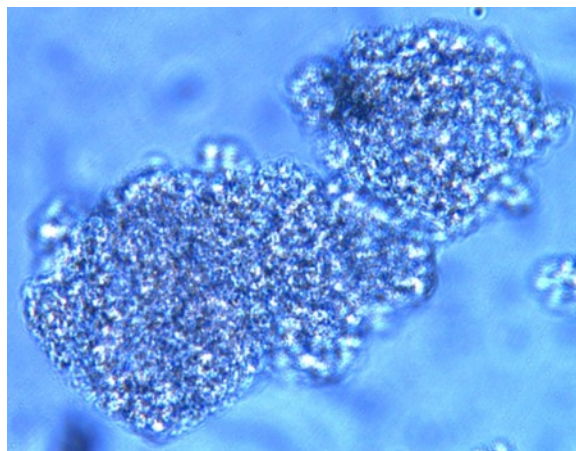


**Figure 20.** Optical micrograph of exfoliated HTiNbO<sub>5</sub> flocculated with Na<sub>2</sub>SO<sub>4</sub>. Image captured through a 40x objective and crossed polarizers.

The presence of a broad (001) peak at approximately 18 Å for wet flocculated exfoliated HTiNbO<sub>5</sub> indicates restacking normal to the [001] direction. This peak was observed at slightly different positions between measurements, most likely due to varying quantities of interlayer water. Using the Scherrer formula, the measured tactoid thickness is 66 Å or roughly five to six sheets. By comparison, Onoda *et al.* simulated restacked Ca<sub>2</sub>Nb<sub>3</sub>O<sub>10</sub> nanosheets to be seven sheets thick based on a random restacking model.<sup>71</sup> Similar stacking thicknesses have also been reported by Gunjakar *et al.*<sup>19</sup> who reported 4-7 layers in layered-double-hydroxide/titanate hybrids and by Kobayashi *et al.*<sup>11</sup> who reported crystallite sizes of 4-5 nm in scrolled niobates. Flocculated nanosheets of exfoliated HTi<sub>2</sub>NbO<sub>7</sub> showed an extremely weak (001) reflection, while exfoliated H<sub>3</sub>Ti<sub>5</sub>NbO<sub>14</sub> did not appear to display an (001) reflection at all. Each chemistry possessed a reflection at approximately 48° 2θ which corresponds to the short axis of each unit

cell (see Table I). The peak at  $27^\circ 2\theta$  for flocculated exfoliated  $\text{HTiNbO}_5$  corresponds to the (200) reflection.

Flocculation is proposed as a two-step process mediated by the cation. First, the positively charged ions accumulate on the nanosheet surface and neutralize the negative sheet charge, allowing neighboring sheets to restack into tactoids thereby lowering system entropy. Second, the significantly reduced double-layer allows neighboring tactoids to link edge-to-face. The result is an apparent aggregation of restacked nanosheets into a house-of-cards type structure. Curiously, heating a suspension of exfoliated  $\text{HTiNbO}_5$ , for example, also resulted in flocculation which reversed upon cooling. The zeta-potential's dependence on temperature has been reported previously and may partially explain this phenomenon.<sup>78,79</sup>

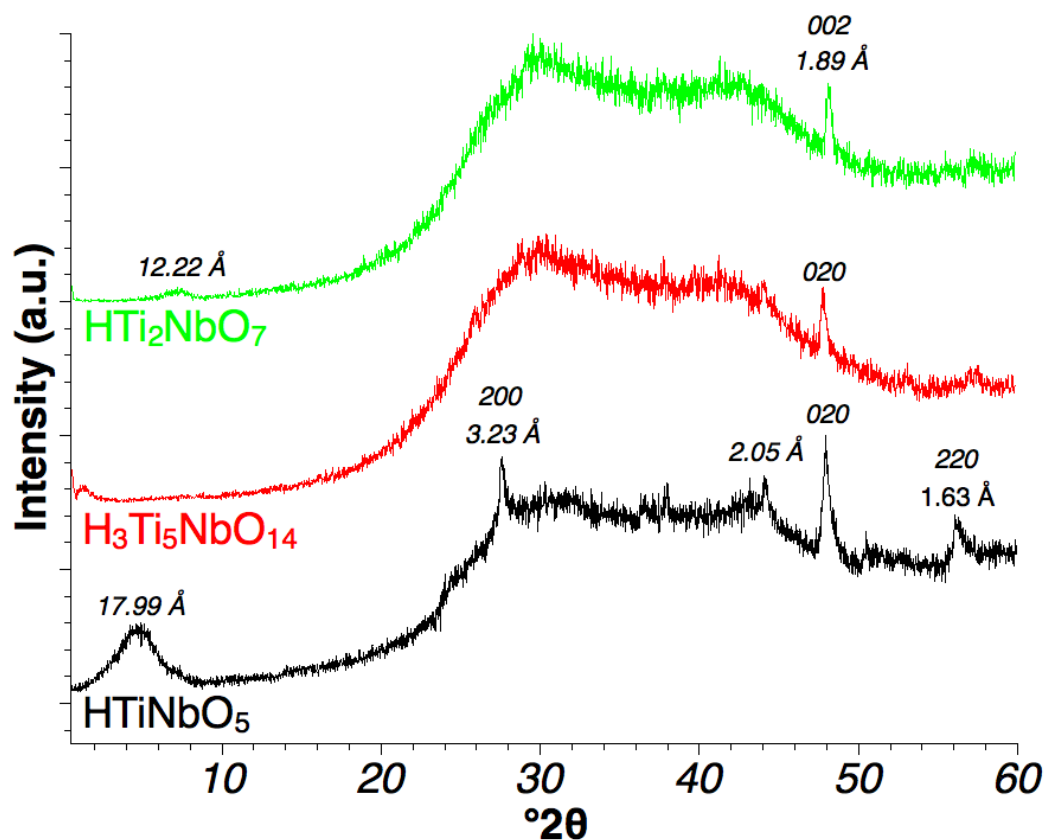


Figure 21. XRD patterns of exfoliated  $\text{HTiNbO}_5$ , exfoliated  $\text{H}_3\text{Ti}_5\text{NbO}_{14}$ , and exfoliated  $\text{HTi}_2\text{NbO}_7$  flocculated with  $\text{Na}_2\text{SO}_4$ , rinsed, and suspended in  $\text{H}_2\text{O}$ . Concentration of  $\text{Na}_2\text{SO}_4$  in the suspension was approximately 0.04 molar. Measured in reflection geometry with variable divergence slits.

### 3. Liquid crystals

The addition of a high atomic number alkali cation such as  $\text{Cs}^+$  for exfoliated  $\text{HTiNbO}_5$  and exfoliated  $\text{HTi}_2\text{NbO}_7$  or  $\text{K}^+$  for exfoliated  $\text{H}_3\text{Ti}_5\text{NbO}_{14}$  resulted in an enhanced liquid crystalline state that was neither gelled or flocculated. Like flocculation, the process proceeded gradually until the concentration of salt exceeded approximately 0.04M. This state was observed as having noticeably increased opalescence relative to as-prepared nanosheet suspensions. Diffraction patterns of suspended and dry  $\text{Cs}_2\text{CO}_3$  treated exfoliated  $\text{HTiNbO}_5$  are shown in Figure 22. Suspended nanosheets show typical  $hk0$  peaks from in-plane diffraction and weak (001) diffraction at 12.1 Å. Allowing suspensions to dry with complete preferred orientation resulted in (001) reflections with a  $d_{001}$  of 12.1 Å. These observations suggest the formation of tactoids with inter-sheet distances of 12.1 Å. Estimated crystallite size via the Scherrer formula is 89 Å or approximately seven sheets. While small alkali cations with high charge densities promote restacking of nanosheets,  $\text{K}^+$  and  $\text{Cs}^+$  cations have low charge densities and therefore may be unable to link neighboring tactoids. Different behavior between chemistries with respect to the introduced salt is likely the result of differing sheet charge and hydration shells.

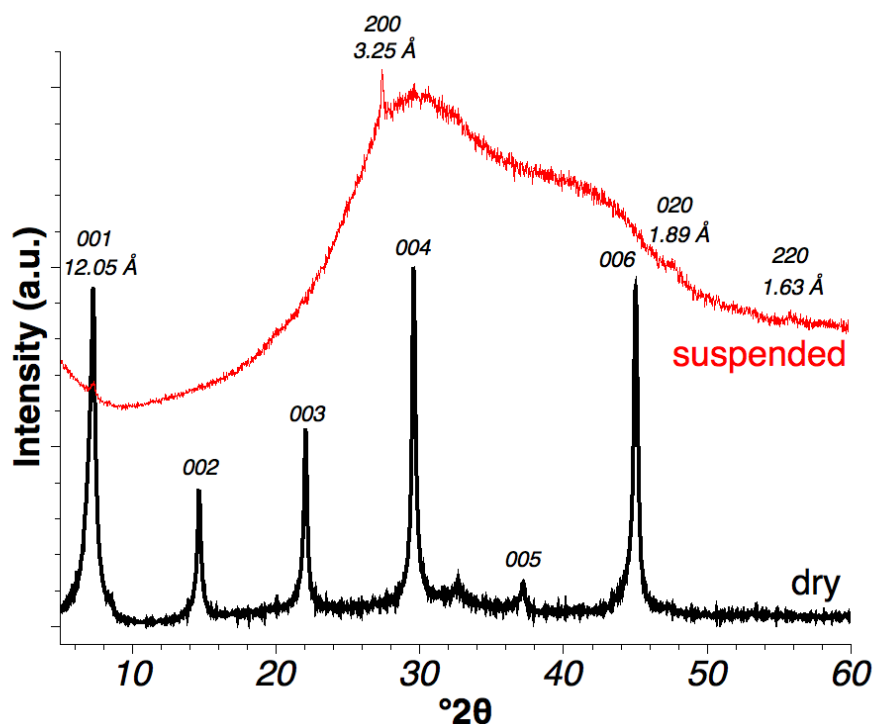


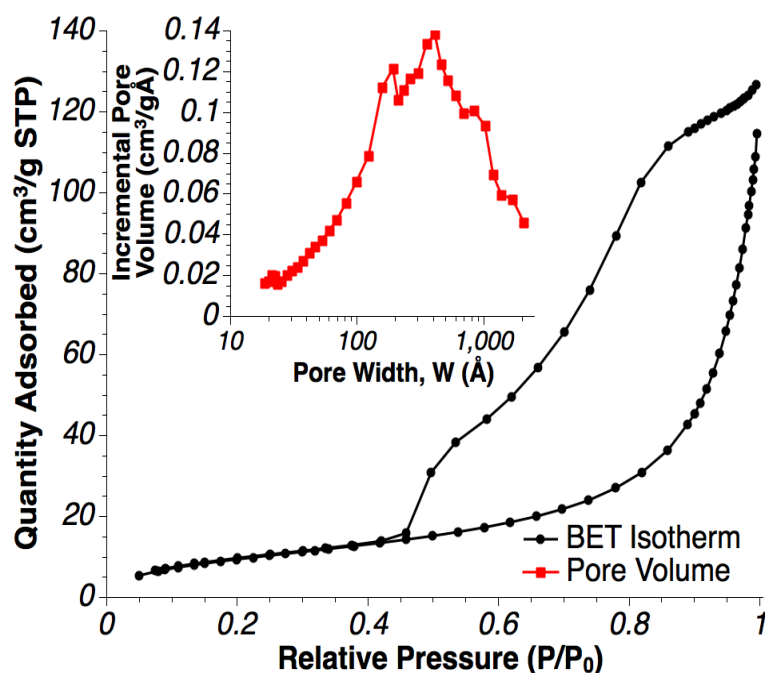
Figure 22. XRD patterns for exfoliated  $\text{HTiNbO}_5$  treated with  $\text{Cs}_2\text{CO}_3$  in suspension and dried as a film. Concentration of  $\text{Cs}_2\text{CO}_3$  was approximately 0.04 molar.

## C. Self-Assembled Microstructures

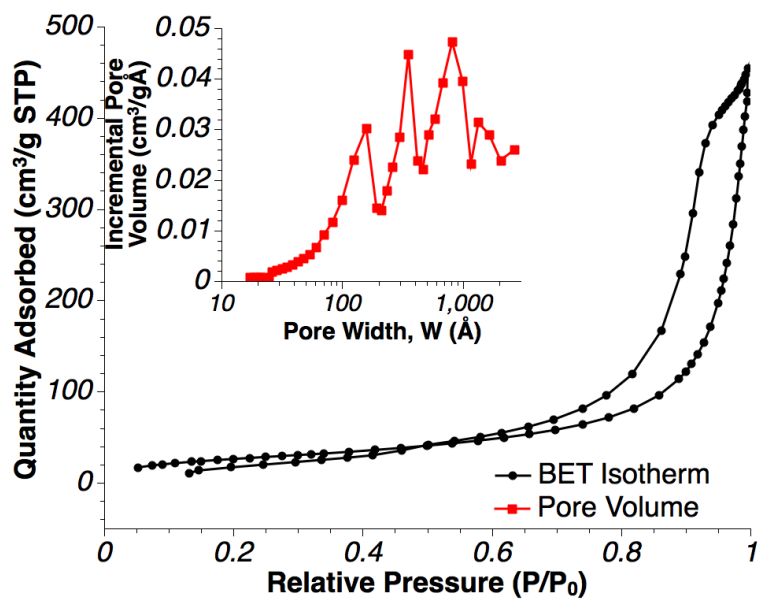
### 1. Gelation

A gelled suspension composed of electrostatically repelled sheets should form a microstructure dominated by face-to-face restacking once dried. As a result, the dry assembled gel should possess significant mesoporosity from the pores formed between restacked sheets. A BET adsorption/desorption isotherm, pore size distribution, and SEM micrographs for gelled exfoliated HTiNbO<sub>5</sub>, shown in Figure 23 and Figure 24, respectively, support this hypothesis. Measured specific surface areas for an assembled exfoliated HTiNbO<sub>5</sub> gel was 37 m<sup>2</sup>/g. The type IV isotherm and large type H4 hysteresis loop shown in Figure 23 indicate mesoporosity due to agglomerates of plate-like particles and slit-like pores, according to the IUPAC classification.<sup>80</sup> The pore size distribution also provided in Figure 23 reveals the majority of pores ranged from 15-85 nm indicating a substantially mesoporous structure. Pores of this size would not be formed between perfectly parallel restacked sheets, however. They are therefore likely the result of misaligned or crumpled sheets that have generally adopted face-to-face restacking, thereby producing narrow slit-like pores. SEM images in Figure 24 show this crumpled type of microstructure.

(a)



(b)



(c)

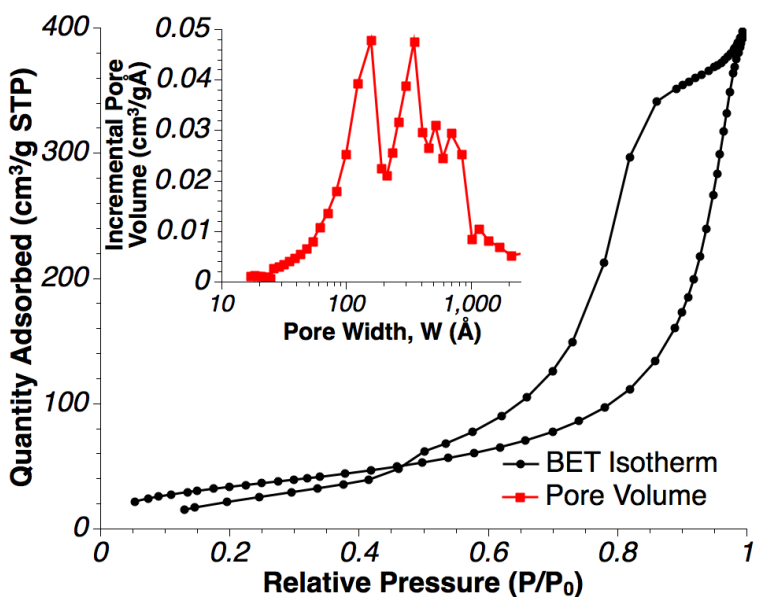
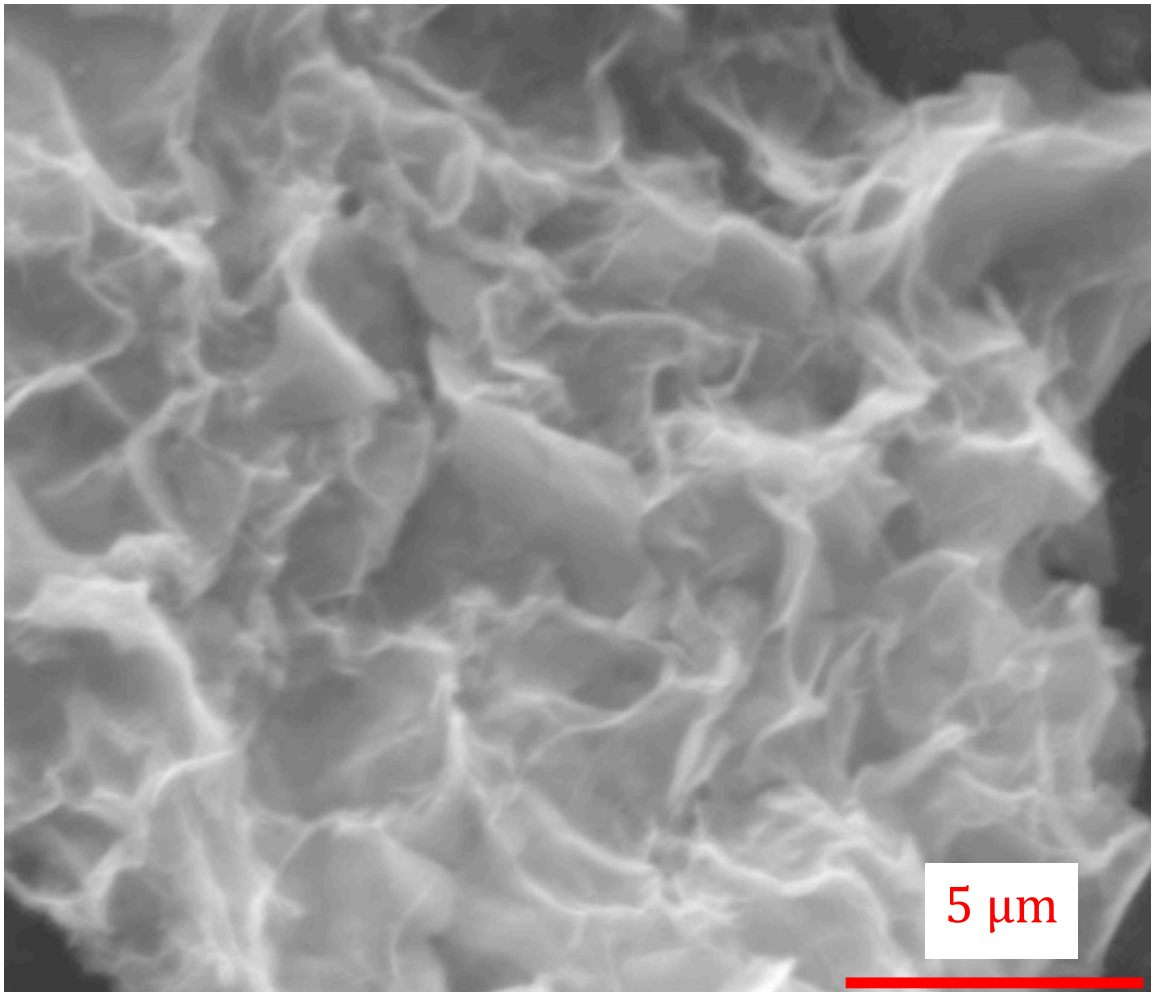


Figure 23. BET isotherms and pore size distributions (insets) for (a) assembled exfoliated HTiNbO<sub>5</sub>, (b) exfoliated H<sub>3</sub>Ti<sub>5</sub>NbO<sub>14</sub>, and (c) exfoliated HTi<sub>2</sub>NbO<sub>7</sub> gels. Pore size distributions were calculated from the BJH adsorption with a Halsey:Faas correction.



**Figure 24. SEM image of freeze dried exfoliated and gelled  $\text{HTi}_2\text{NbO}_7$  assembly.**

XRD patterns collected from powdered gels show poorly crystalline structures. Estimated crystallite sizes range from 7-9 nm. Observed peaks roughly correspond to the original axes perpendicular to the stacking direction and the measured (00l) located between  $5\text{-}10^\circ 2\theta$ . Explicit pattern indexing was not possible; however, the patterns did not correspond to the decomposition products of each chemistry. XPS spectra shown in Figure 26 reveal the chemistry of assembled gels to be composed of Ti, Nb, and O without any other major elements. No K peaks were observed for exfoliated  $\text{HTiNbO}_5$  or exfoliated  $\text{H}_3\text{Ti}_5\text{NbO}_{14}$ , while a trace quantity of Cs was observed for exfoliated  $\text{HTi}_2\text{NbO}_7$ . No significant shifts in peak shapes corresponding to changes in the valence state of Ti or Nb were observed between chemistries.

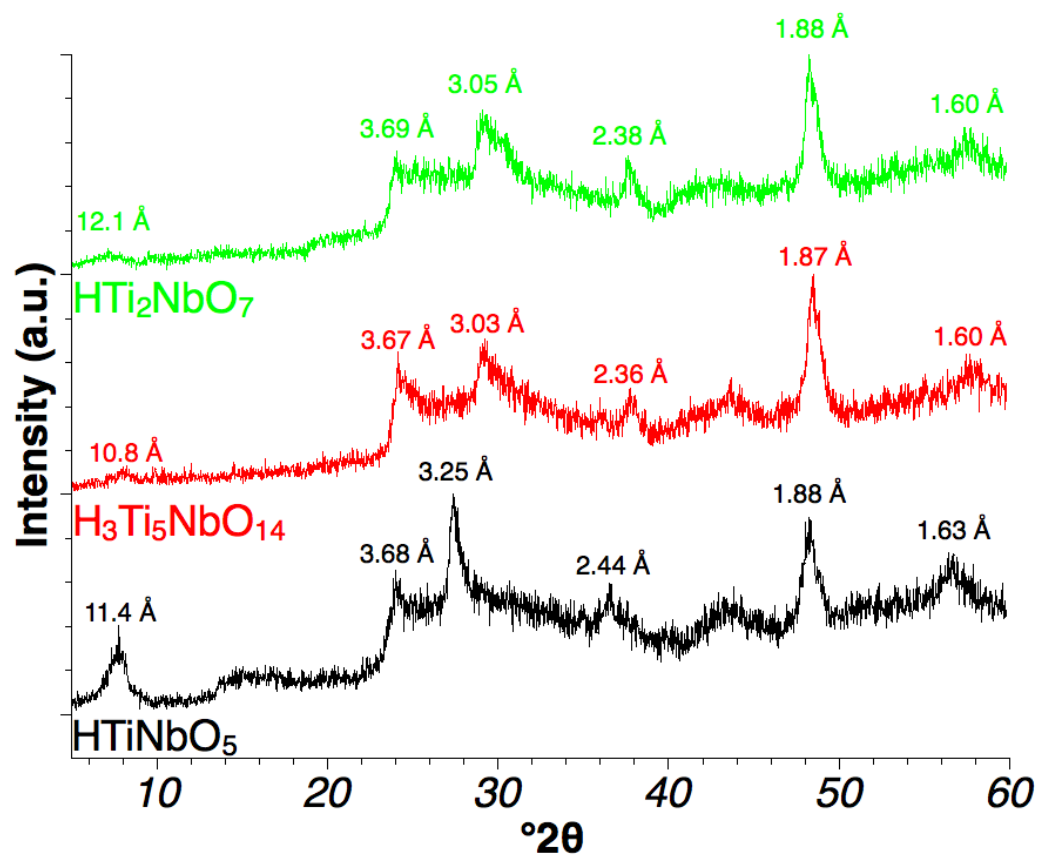
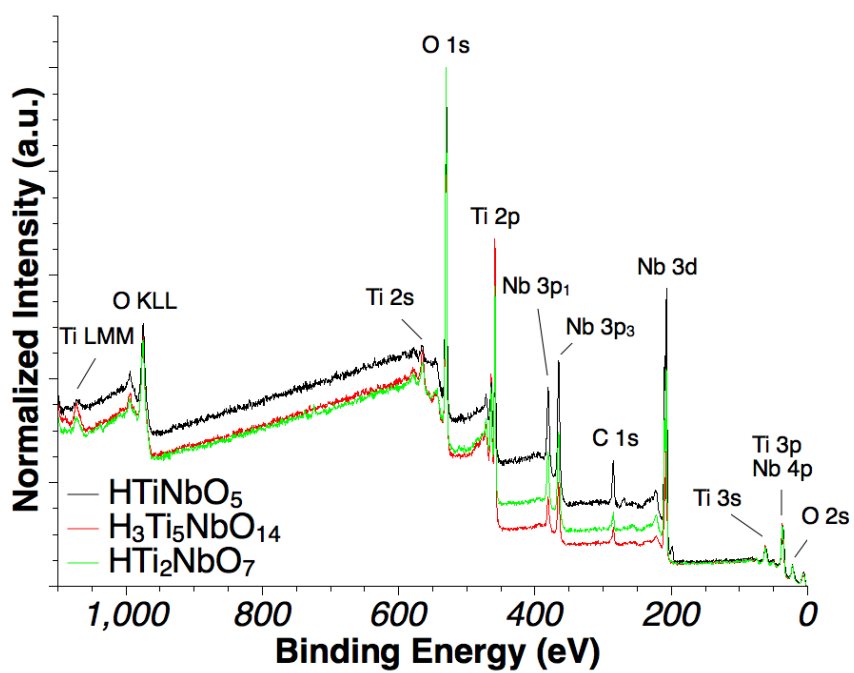
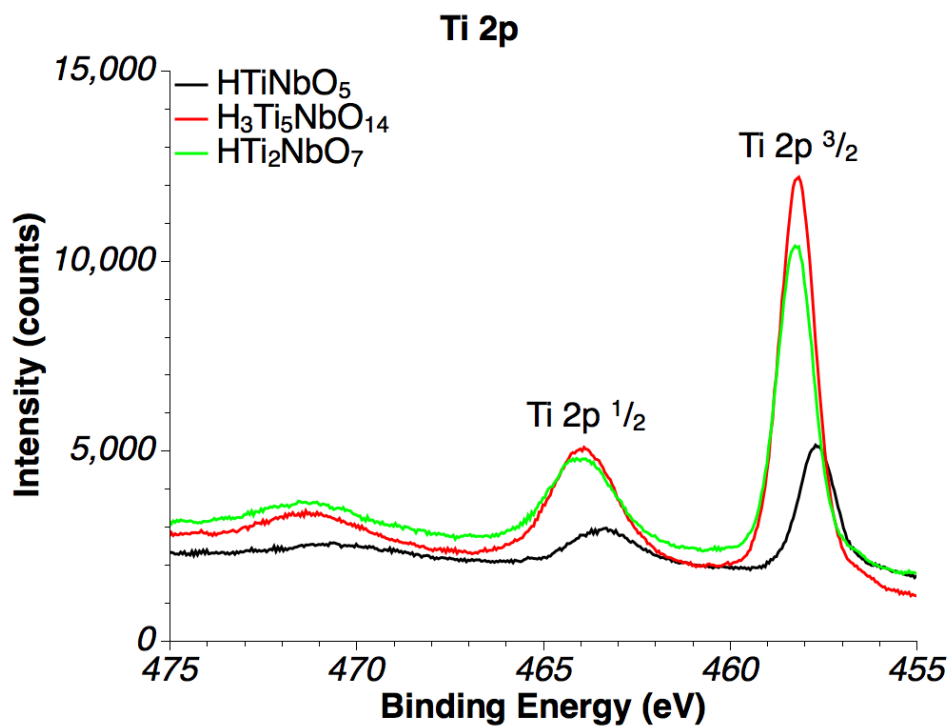


Figure 25. XRD patterns for assemblies of exfoliated and gelled HTiNbO<sub>5</sub>, H<sub>3</sub>Ti<sub>5</sub>NbO<sub>14</sub>, HTi<sub>2</sub>NbO<sub>7</sub> powders dried at 75° C. D-spacings are provided for primary peaks. Samples were measured in reflection geometry with variable divergence slits.

(a)



(b)



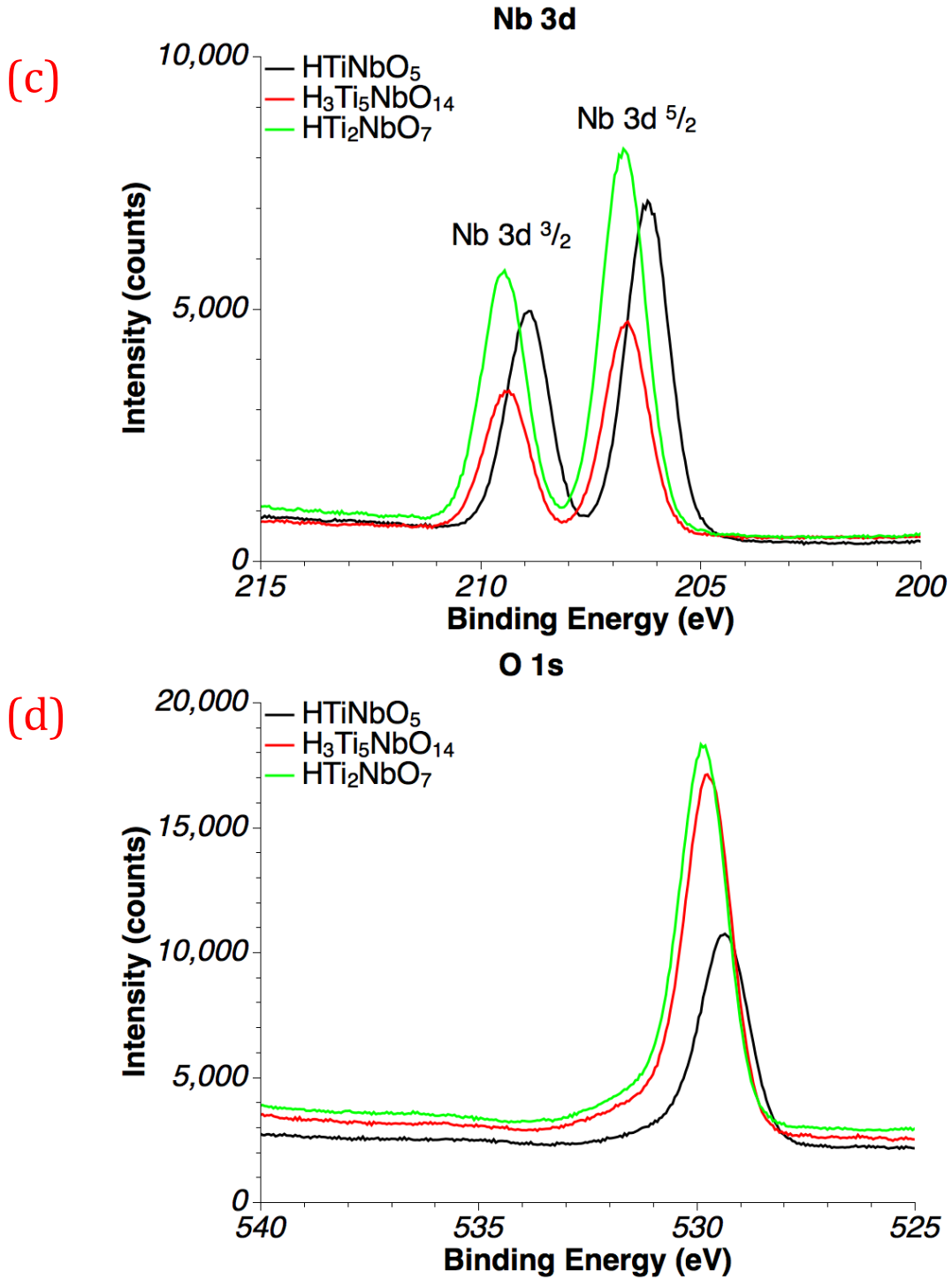


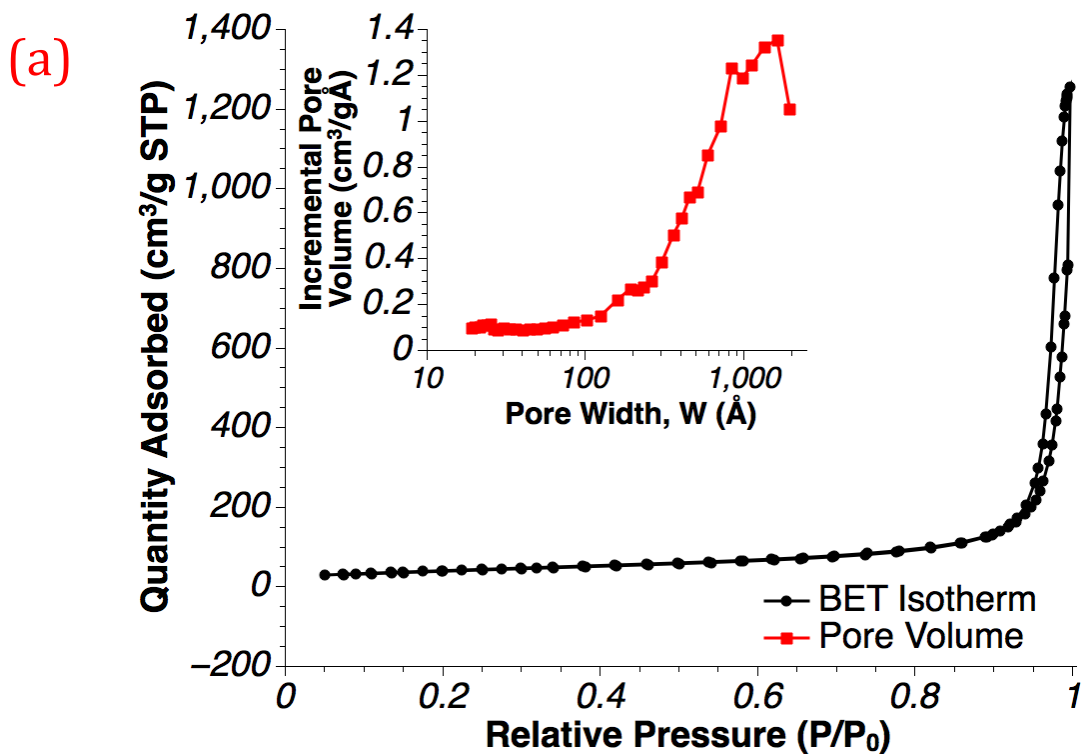
Figure 26. XPS survey spectra of exfoliated and HCl gelled (a) HTiNbO<sub>5</sub>, H<sub>3</sub>Ti<sub>5</sub>NbO<sub>14</sub>, and HTi<sub>2</sub>NbO<sub>7</sub>. Auger transitions and XPS peaks are labeled accordingly. High resolution XPS spectra of (b) Ti 2p, (c) Nb 3d, (d) O 1s peaks for each chemistry.

## 2. Flocculation

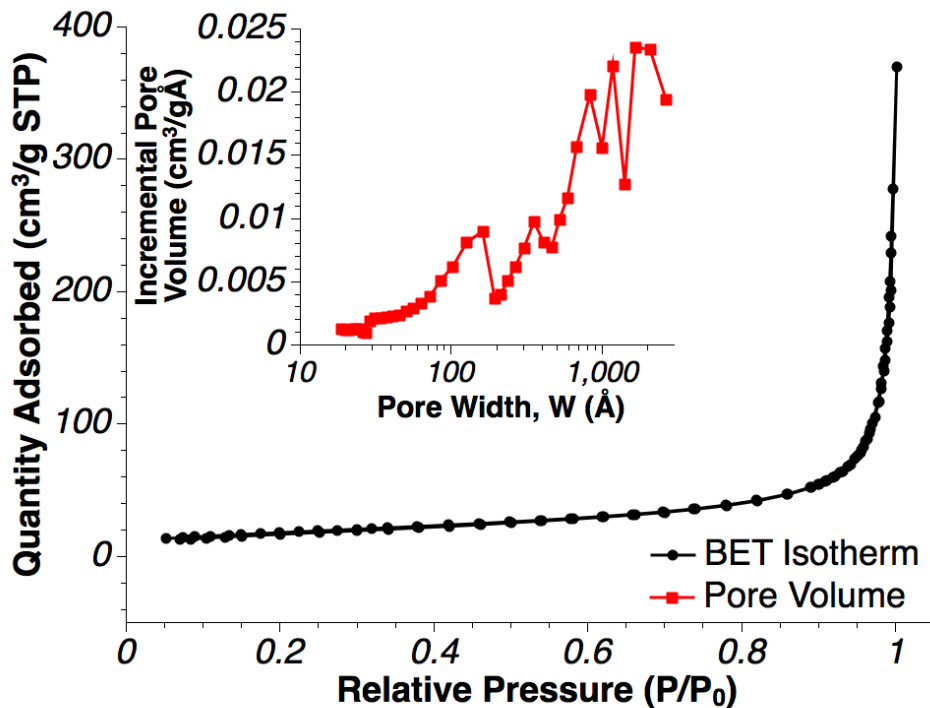
In contrast to a gel, flocculated nanosheets dominated by edge-to-face restacking should possess very little mesoporosity given the assumption that measured mesoporosity is the interlayer galleries formed by restacked nanosheets sheets. The BET measurements and SEM images provided in Figure 27 and Figure 28 respectively confirm this hypothesis. BET isotherms show minimal hysteresis, implying an open network of larger pores. Pore size distributions revealed a significant quantity of pores greater than 50 nm, indicating a macroporous structure. BET data for gelled and flocculated samples are summarized in Table III. Whereas the small mesopores in gelled assemblies are the result of restacked sheets, the large macropores observed in flocculated assemblies are produced by the interstices between significantly misaligned sheets in a house-of-cards type assembly. The absence of a mesoporous structure dominated by large pores is observed in Figure 28, contrary to the gelled assemblies. Similar to gelled assemblies, diffraction patterns of assembled flocculated nanosheets reveal a poorly crystalline solid with estimated crystallite sizes ranging between 7-9 nm (Figure 29). Observed peaks roughly correspond to the original axes perpendicular to the stacking direction and the measured intersheet separation distance located between 5-12° 2 $\theta$ . XPS spectra shown in Figure 30 reveal the chemistry of assembled floccules to be composed of Ti, Nb, O, and Na (primarily observed by its Auger transition at 496 eV) without any other major elements. No K peaks were observed for exfoliated HTiNbO<sub>5</sub> or exfoliated H<sub>3</sub>Ti<sub>5</sub>NbO<sub>14</sub>, while a trace quantity of Cs was observed for exfoliated HTi<sub>2</sub>NbO<sub>7</sub>. The small O 1s peak at 535 eV in Figure 30d is most likely due to intercalated isopropanol and not water due to this peaks absence in Figure 26d. The O 1s peak from Na-O bonding overlap the primary Ti/Nb-O peak at 530 eV.

Table III: Specific surface area, average pore width, and specific pore volume (BJH adsorption) for gelled and flocculated exfoliated nanosheets.

Assembly	Chemistry	BET SSA (m <sup>2</sup> /g)	Average Pore Width (nm)	Specific Pore Volume (cm <sup>3</sup> /g)
Gelled	HTiNbO <sub>5</sub>	37	5.8	0.2
	H <sub>3</sub> Ti <sub>5</sub> NbO <sub>14</sub>	126	8.0	0.6
	HTi <sub>2</sub> NbO <sub>7</sub>	147	14.7	0.7
Flocculated	HTiNbO <sub>5</sub>	72	26.7	0.4
	H <sub>3</sub> Ti <sub>5</sub> NbO <sub>14</sub>	116	26.1	0.8
	HTi <sub>2</sub> NbO <sub>7</sub>	63	20.1	0.3



(b)



(c)

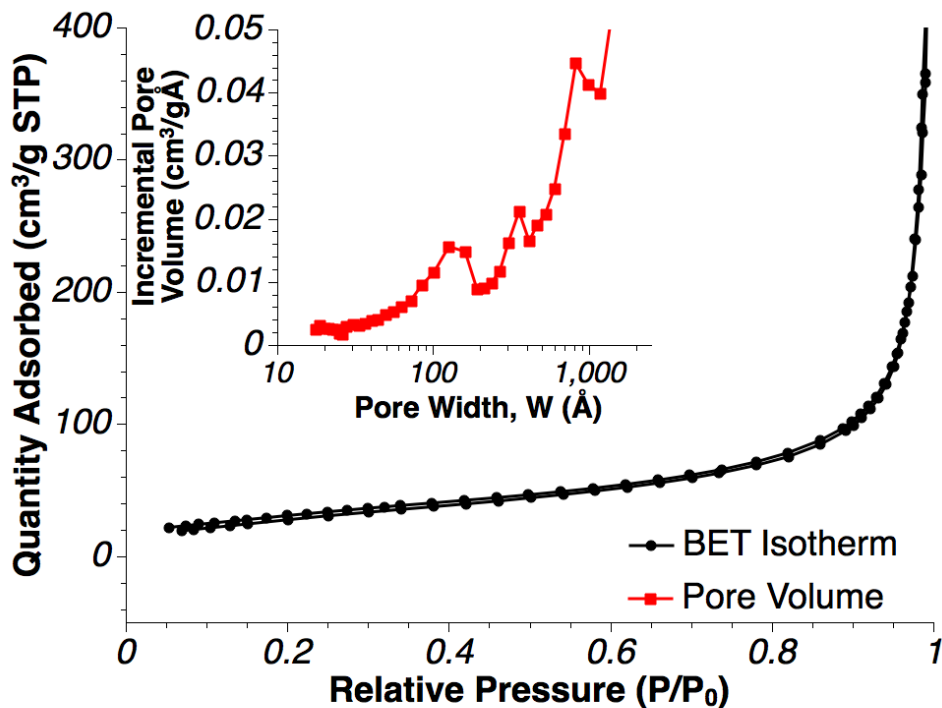


Figure 27. BET isotherms and pore size distributions (insets) for (a) assembled exfoliated  $\text{HTiNbO}_5$ , (b) exfoliated  $\text{H}_3\text{Ti}_5\text{NbO}_{14}$ , and (c) exfoliated  $\text{HTi}_2\text{NbO}_7$ . Exfoliated suspensions were flocculated with  $\text{Na}_2\text{SO}_4$ , boiled in IPA, and subsequently heated to  $400^\circ\text{C}$ . Pore size distributions were calculated from BJH adsorption.

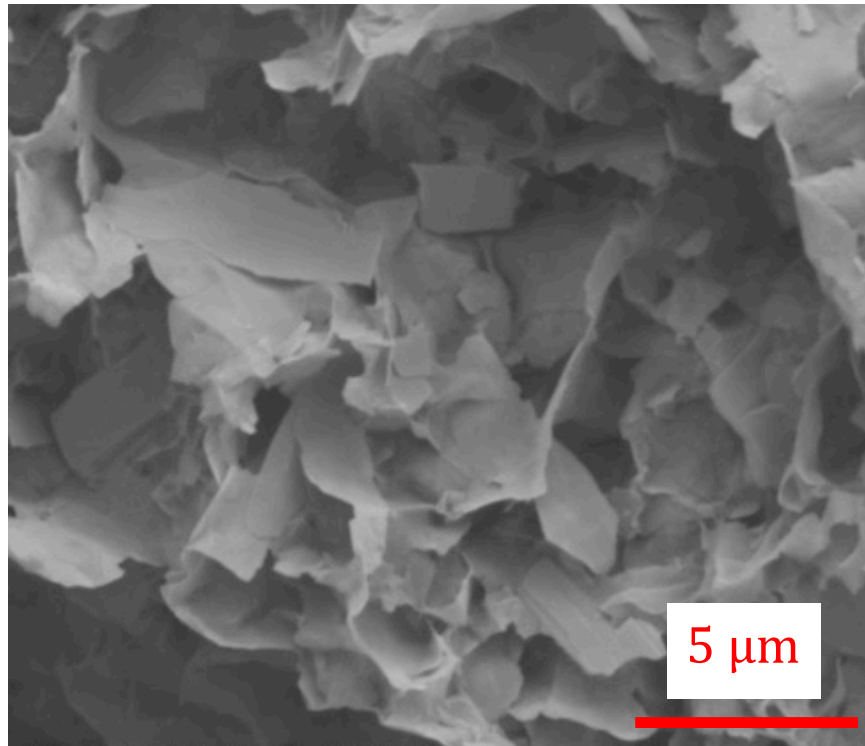


Figure 28. SEM image of freeze dried exfoliated and flocculated HTiNbO<sub>5</sub> assembly.

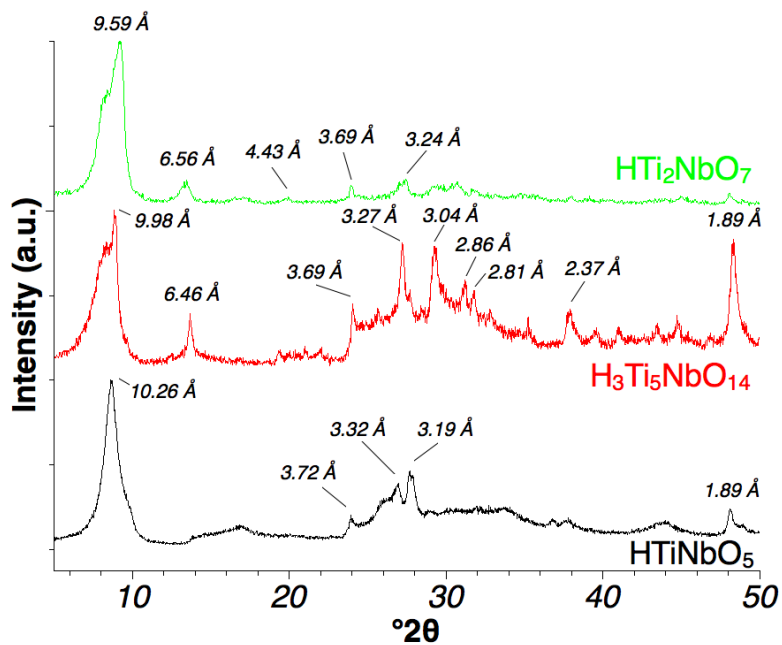
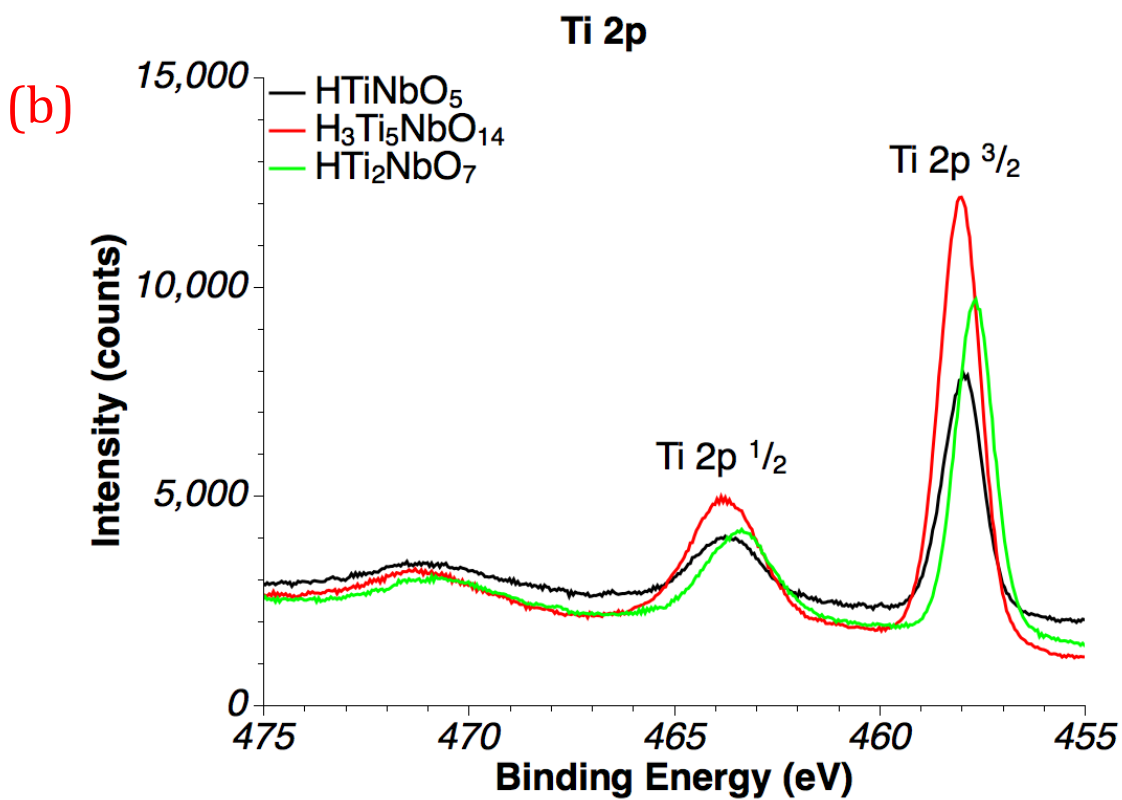
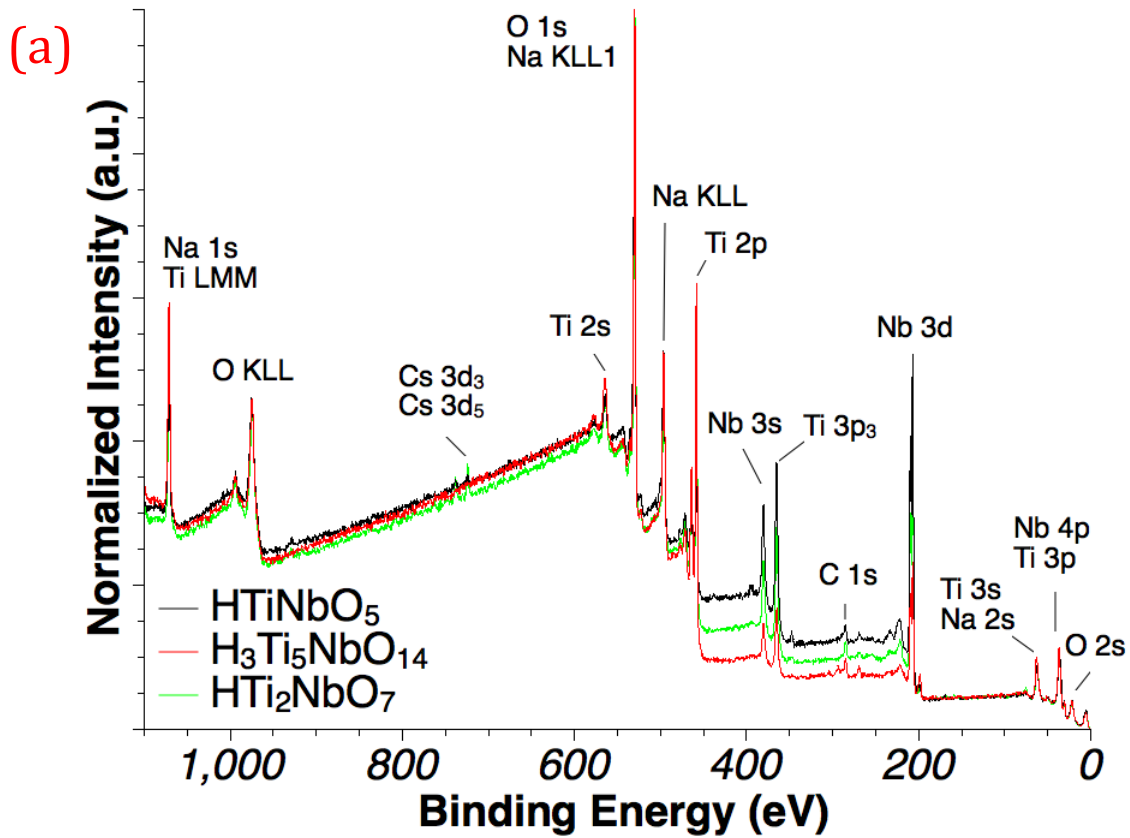


Figure 29. XRD patterns for exfoliated and flocculated HTiNbO<sub>5</sub>, H<sub>3</sub>Ti<sub>5</sub>NbO<sub>14</sub>, and HTi<sub>2</sub>NbO<sub>7</sub> assemblies. Suspensions were flocculated with Na<sub>2</sub>SO<sub>4</sub> to a concentration of 0.04M. Samples were measured in reflection geometry with variable slits.



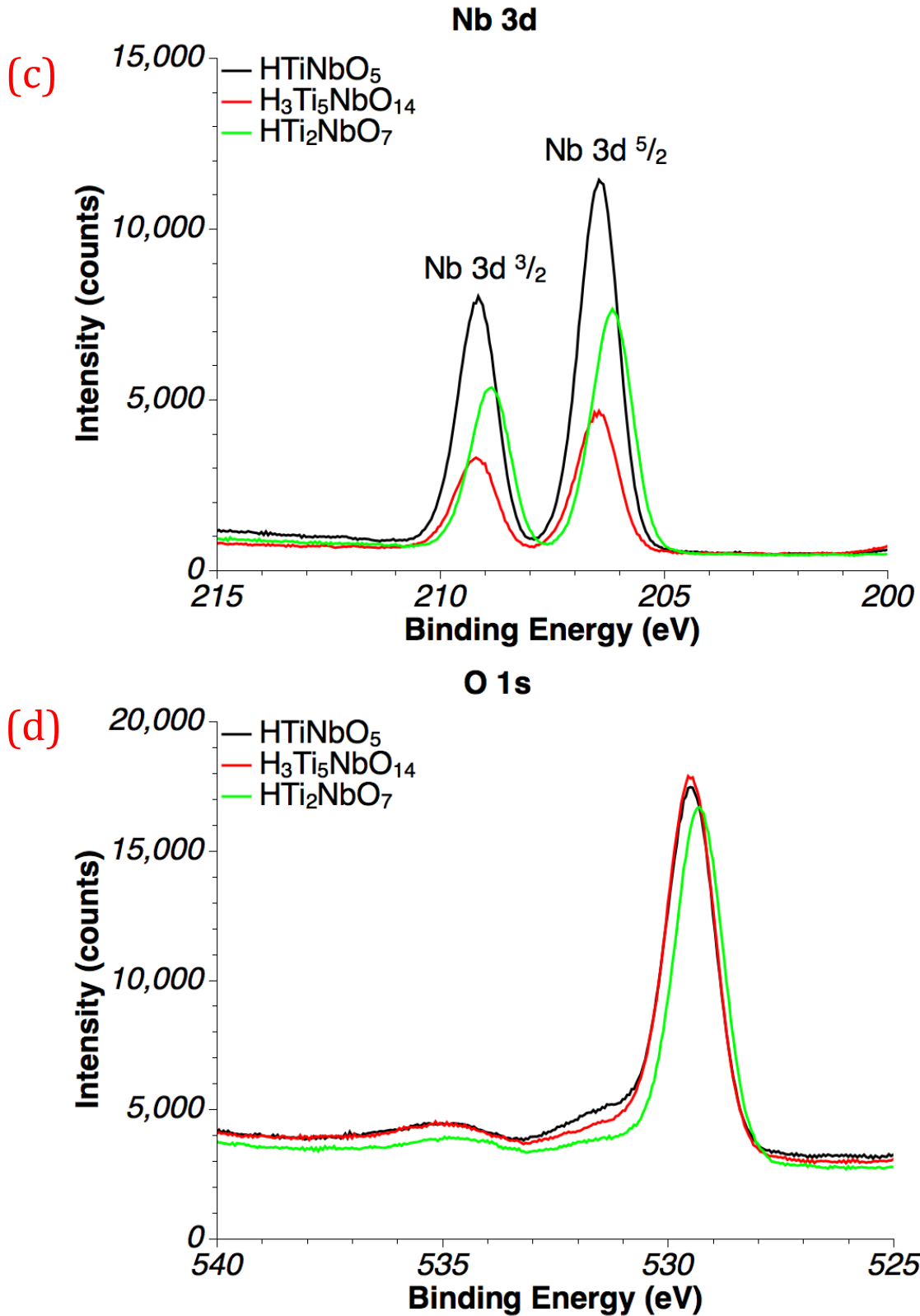


Figure 30. XPS survey spectra of exfoliated and Na<sub>2</sub>SO<sub>4</sub> flocculated (a) HTiNbO<sub>5</sub>, H<sub>3</sub>Ti<sub>5</sub>NbO<sub>14</sub>, and HTi<sub>2</sub>NbO<sub>7</sub>. Auger transitions and XPS peaks are labeled accordingly. High resolution XPS spectra of (b) Ti 2p, (c) Nb 3d, (d) O 1s peaks.

## D. Photocatalysis

### 1. Optical Properties of Nanosheets

Diffuse reflectance UV-vis spectra demonstrated unique absorbance in the UV and visible range once phases were exfoliated as shown in Figure 31a and b. Measured band gaps are summarized in Table IV. Exfoliated nanosheets possessed band gaps reduced from approximately 4.1 eV for their parent phases to approximately 3.6 eV due to the quantum confinement effect. For comparison, Akatsuka *et al.* found the chemistries  $\text{TiNbO}_5^-$ ,  $\text{Ti}_2\text{NbO}_7^-$ , and  $\text{Ti}_5\text{NbO}_{14}^{3-}$  to have band gap energies between 3.7-3.5 eV.<sup>17</sup> The band gaps of the parent oxides have been reported elsewhere as between 3.5-3.6 eV, however.<sup>81,17</sup> Although the quantum confinement effect is often used to widen the band gap, thereby preventing electron-hole recombination in photocatalytic systems, a reduced band gap allows more wavelengths to be adsorbed and may improve photocatalysis.

**Table IV: Summarized Band Gap Energies For Parent And Exfoliated Phases.**

<b>Phase</b>	<b>Parent <math>E_g</math> (eV)</b>	<b>Exfoliated <math>E_g</math> (eV)</b>
<b><math>\text{ATiNbO}_5</math></b>	4.1	3.6
<b><math>\text{A}_3\text{Ti}_5\text{NbO}_{14}</math></b>	4.1	3.6
<b><math>\text{ATi}_2\text{NbO}_7</math></b>	4.1	3.6

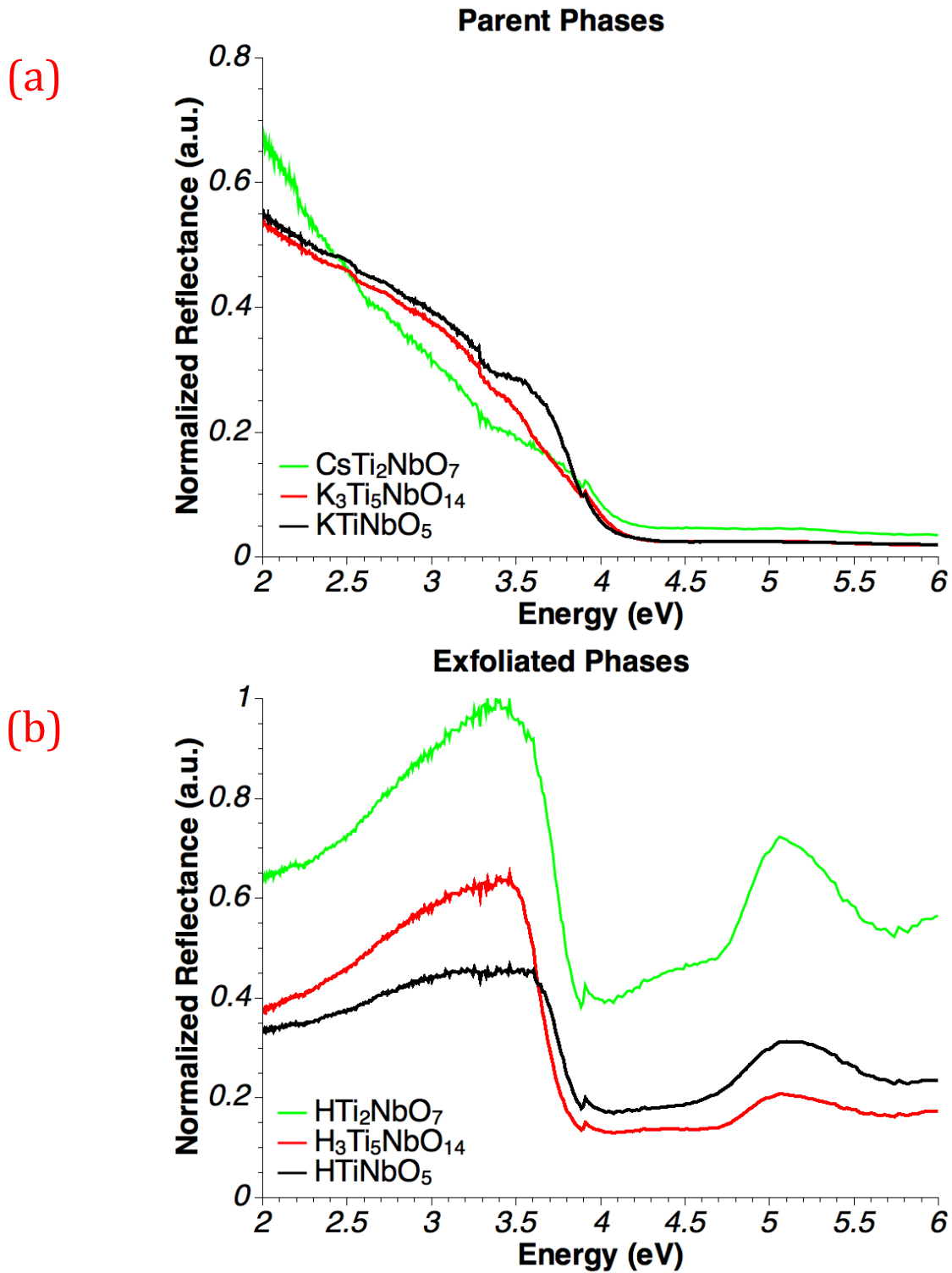


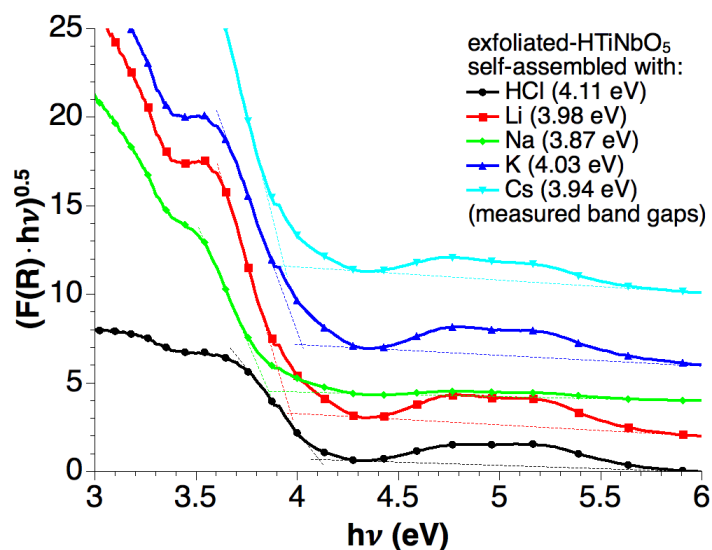
Figure 31. UV-vis diffuse reflectance spectra for (a)  $\text{KTiNbO}_5$ ,  $\text{K}_3\text{Ti}_5\text{NbO}_{14}$ , and  $\text{CsTi}_2\text{NbO}_7$  (b) exfoliated  $\text{HTiNbO}_5$ , exfoliated  $\text{H}_3\text{Ti}_5\text{NbO}_{14}$ , and exfoliated  $\text{HTi}_2\text{NbO}_7$ .

In other systems, the band gap varies significantly with different A-site cations.<sup>7,34</sup> Lucht *et al.* demonstrated this behavior in birnessite manganese oxides, showing direct and indirect band gap shifts of over half an eV for certain intercalated cations.<sup>34</sup> Therefore, reassembling nanosheets with various electrolytes may allow control over the band gap, while also introducing unique adsorption features. Successful reassembly was demonstrated with acid (via HCl) resulting in a gel, while Li, Na, K, Cs, Mn, Ni, La, and Ba salts resulted in flocculates. Although reassembled nanosheets possessed larger band gaps increased relative to films prepared without an electrolyte, no significant trend could be discerned among the studied intercalated cations.

Diffuse reflectance UV spectra are provided for exfoliated HTiNbO<sub>5</sub> as a prototype in Figure 32. Figure 32a shows band gaps between 3.9 eV and 4.1 eV for exfoliated HTiNbO<sub>5</sub> treated with various alkali salts. Figure 32b further shows that the exfoliated HTiNbO<sub>5</sub> band gap does not vary significantly from approximately 3.95 eV when reassembled with Mn, Ni, La, or Ba salts. Ni and Mn flocculated HTiNbO<sub>5</sub> nanosheets turned pale green and black respectively once repeatedly rinsed with H<sub>2</sub>O and dried, suggesting the formation of a surface oxide layer or color centers which may give rise to other interesting properties.

The poor dependence of band gap on intercalated cation may be due in part to the microstructure of the reassembled flocculates. As detailed in the previous sections, flocculated nanosheets form tactoids several nanometers thick composed of several face-to-face restacked nanosheets. The tactoids then restack edge-to-face forming a long range network structure which is not entirely eliminated when dried. This structure differs from those of Kato and Lucht who explored band gap energies in bulk materials.<sup>7, 34</sup> Therefore, the quantum confinement effect which initially reduced the band gap is not totally eliminated and the measured band gap depends not only on the flocculating cation, but also the tactoid size and network structure.

(a)



(b)

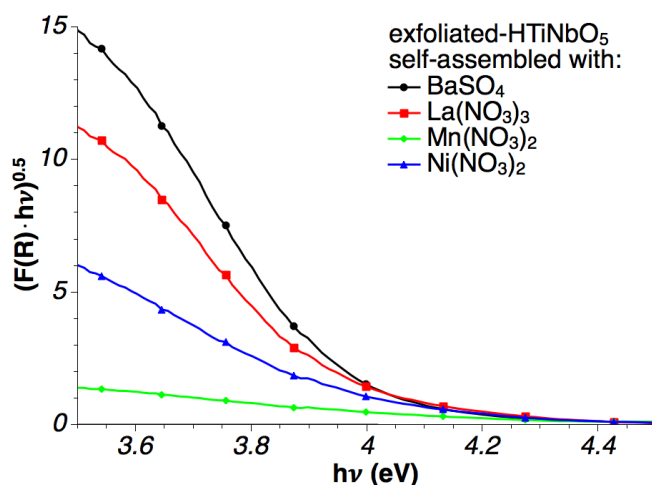


Figure 32: Diffuse reflectance UV-vis spectra for: (A) exfoliated HTiNbO<sub>5</sub> reassembled with HCl (●), LiOH (■), Na<sub>2</sub>SO<sub>4</sub> (◆), KCl (▲), and Cs<sub>2</sub>CO<sub>3</sub> (▼). Curves have been offset for clarity, and dashed lines were added to resolve band gap. (B) exfoliated HTiNbO<sub>5</sub> reassembled with BaSO<sub>4</sub> (●), La(NO<sub>3</sub>)<sub>3</sub> (■), Mn(NO<sub>3</sub>)<sub>2</sub> (◆), and Ni(NO<sub>3</sub>)<sub>2</sub> (▲).

## 2. Photocatalytic Hydrogen Production

Nanosheets and P25 without Pt co-catalyst produced little hydrogen after four hours. However, Figure 33 shows a significant improvement in yields after loading 1 weight % Pt. Exfoliated H<sub>3</sub>Ti<sub>5</sub>NbO<sub>14</sub> showed the largest hydrogen evolution rate at 426.0 μmol H<sub>2</sub>/hr/g followed by exfoliated HTi<sub>2</sub>NbO<sub>7</sub> and exfoliated HTiNbO<sub>5</sub> at 117.1 and 24.6 μmol H<sub>2</sub>/hr/g respectively. This result suggests a trend may exist with Ti:Nb ratio and therefore chemistry, but not crystallographic motif. Evolution rates of H<sub>2</sub> are summarized in Table V. It should be noted

that in addition to adding a co-catalyst, Pt loading also replaced the suspension medium with fresh DI water free of soluble ions. It is not clearly understood how TBA interferes with photocatalytic reactions. However, assembling (flocculating) nanosheets with aqueous salts such as  $\text{Na}_2\text{SO}_4$  allowed nanosheets to be centrifuged from suspension and rinsed. Flocculated and rinsed exfoliated  $\text{HTiNbO}_5$  produced hydrogen at a rate of  $4.2 \mu\text{mol H}_2/\text{hr/g}$ . In contrast, Pt-loaded and flocculated exfoliated  $\text{HTiNbO}_5$  resulted in an improved hydrogen yield, whereas Pt-loaded exfoliated  $\text{H}_3\text{Ti}_5\text{NbO}_{14}$  and exfoliated  $\text{HTi}_2\text{NbO}_7$  produced less hydrogen after flocculating. These yields are tabulated in Table V. Flocculating nanosheets with transition metals did not improve photocatalytic hydrogen yields.

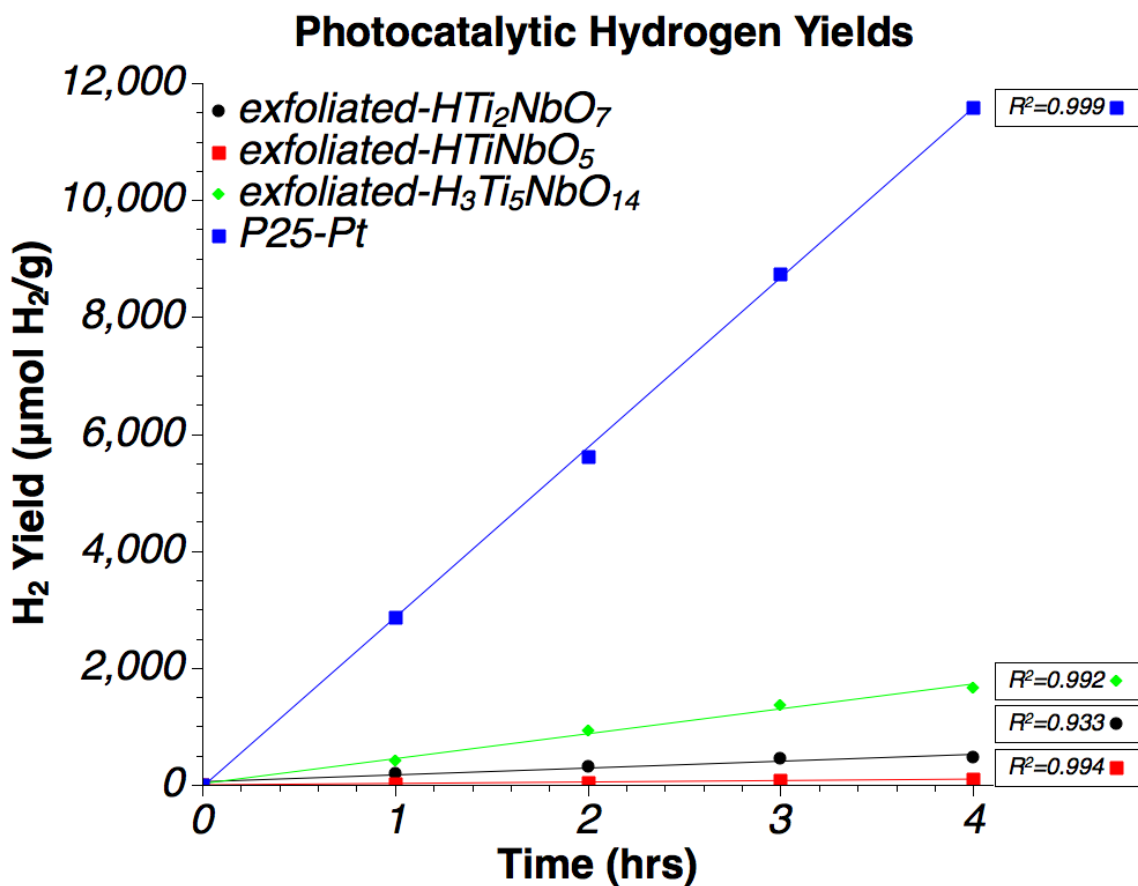


Figure 33. Hydrogen yields for nanosheet suspensions with 1% Pt and P25 with 1% Pt.

**Table V: Measured Hydrogen Rates For P25, Exfoliated HTiNbO<sub>5</sub>, Exfoliated H<sub>3</sub>Ti<sub>5</sub>NbO<sub>14</sub>, and Exfoliated HTi<sub>2</sub>NbO<sub>7</sub> Nanosheets With And Without Pt Co-Catalyst.**

Phase	H <sub>2</sub> Yield (μmol H <sub>2</sub> /hr/g)		
	No Pt (unfloculated)	1% Pt (unfloculated)	1% Pt (floculated)
P25	22.4	2905.6	NA
Exfoliated HTiNbO <sub>5</sub>	1.1	24.6	58.4
Exfoliated H <sub>3</sub> Ti <sub>5</sub> NbO <sub>14</sub>	11.9	426.0	196.1
Exfoliated HTi <sub>2</sub> NbO <sub>7</sub>	7.4	117.1	47.5

Self-assembly of flocculated nanosheets allows solids to be collected and dried into a high surface area powder. Hydrogen evolution rates are provided for these powders in Table VI. With the exception of exfoliated HTiNbO<sub>5</sub>, less hydrogen was evolved from the flocculates compared to the original suspended nanosheets. Further heating the flocculates produced no significant change in hydrogen evolution rates. Decreased rates are most likely due to the diminished surface area and increased band gap of flocculated powders compared to as-prepared (discrete) nanosheets. Heating of nanosheet assemblies has been shown elsewhere to improve photo-activity.<sup>10</sup>

**Table VI: Measured hydrogen rates for exfoliated HTiNbO<sub>5</sub>, exfoliated H<sub>3</sub>Ti<sub>5</sub>NbO<sub>14</sub>, and exfoliated HTi<sub>2</sub>NbO<sub>7</sub> flocculated with Na<sub>2</sub>SO<sub>4</sub>, rinsed, boiled in IPA to produce a high surface area powder, heated to temperature, dispersed in H<sub>2</sub>O, then loaded with 1% Pt.**

Chemistry	H <sub>2</sub> Yield (μmol H <sub>2</sub> /hr/g)		
	1% Pt (unfloculated & suspended)	Dry (75° C)	Dry (400° C)
Exfoliated HTiNbO <sub>5</sub>	24.6	47.4	28.6
Exfoliated H <sub>3</sub> Ti <sub>5</sub> NbO <sub>14</sub>	426.0	21.2	37.6
Exfoliated HTi <sub>2</sub> NbO <sub>7</sub>	117.1	16.4	14.7

Having demonstrated that flocculated nanosheets yield less hydrogen than the initial suspension, their primary benefit may be to produce composites with other materials. For example, a composite of P25 and exfoliated HTiNbO<sub>5</sub> mixed in a 4:1 ratio can be readily flocculated with Na<sub>2</sub>SO<sub>4</sub>, rinsed, and dried into a homogeneous powder which remained stable

when redispersed in H<sub>2</sub>O. This composite produced 412 μmol H<sub>2</sub>/hr/g without the addition of any co-catalyst as shown in Figure 34. Loading this composite with 1% Pt increased the hydrogen yield to 2112 μmol H<sub>2</sub>/hr/g, which represents a slightly lesser yield than P25-Pt alone. The improved performance of P25-nanosheet composite may be explained as follows. The small bandgap of P25 (rutile specifically) enhances photogeneration compared to the HTiNbO<sub>5</sub> nanosheet. The photogenerated electron may then migrate from rutile to electron traps located in anatase before finally migrating to electron traps and reaction sites located on the nanosheet surface.<sup>82</sup> Intimate mixing and the high surface areas of both P25 and the nanosheets facilitates charge transfer between different particles. Excellent P25 performance with Pt, but poor performance without suggests that P25 photogenerates electron-hole pairs well, but fails to prevent recombination or migrate electrons to the surface for catalysis unless a suitable co-catalyst exists. Meanwhile, the HTiNbO<sub>5</sub> nanosheets offer poor performance independent of whether a co-catalyst is used or not, suggesting that the nanosheet does not possess a suitable environment for photogenerating electron-hole pairs. Therefore, the nanosheets in a P25 composite do not act as generating sites, but instead act only as electron traps and reaction sites. When Pt is added to the composite, the need to migrate electrons to the nanosheet is rendered irrelevant since electrons generated within the P25 can readily transfer to the Pt surface sites.

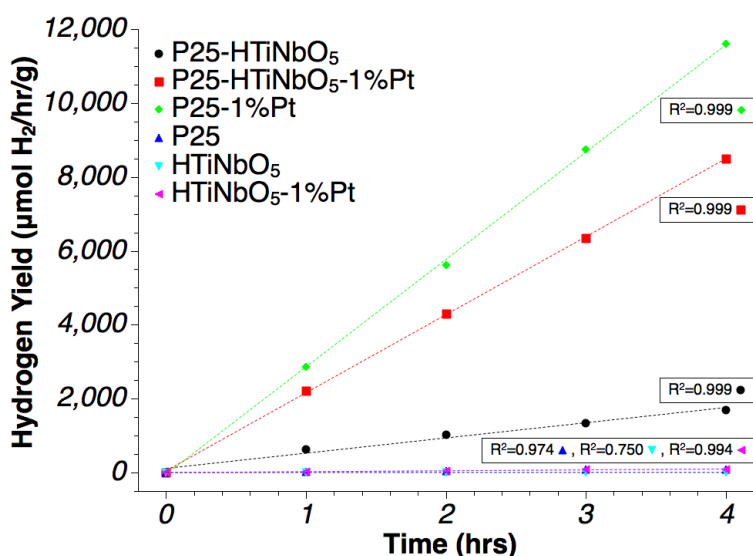
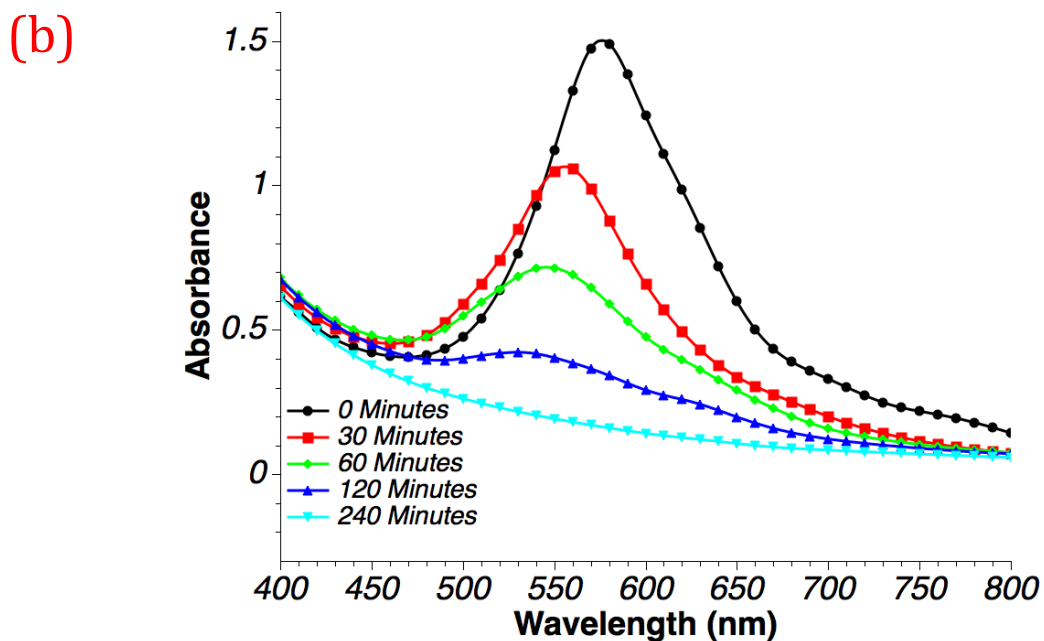
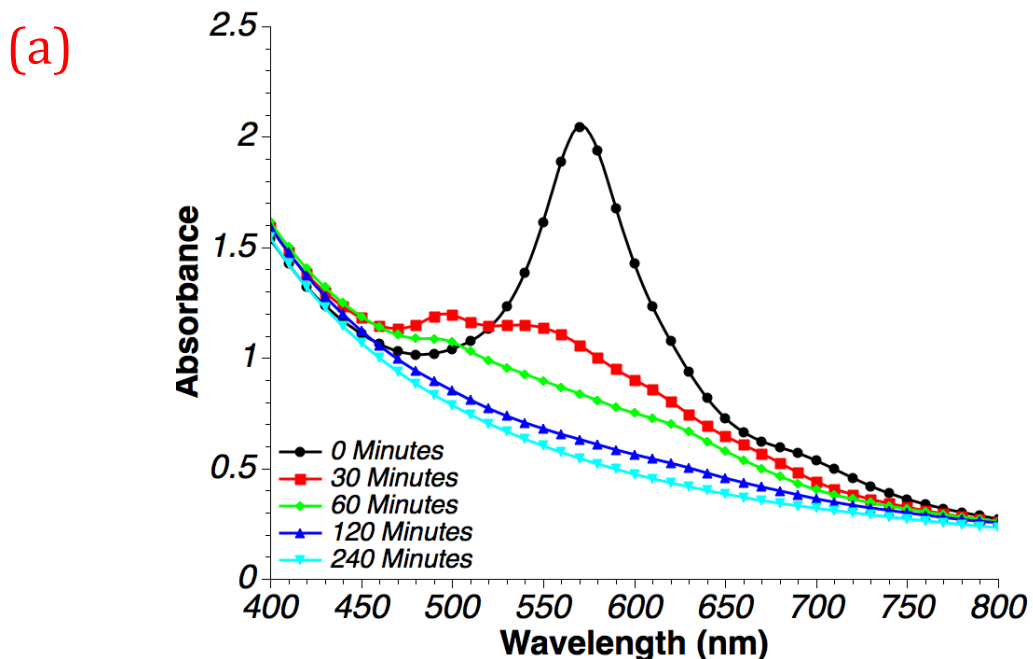


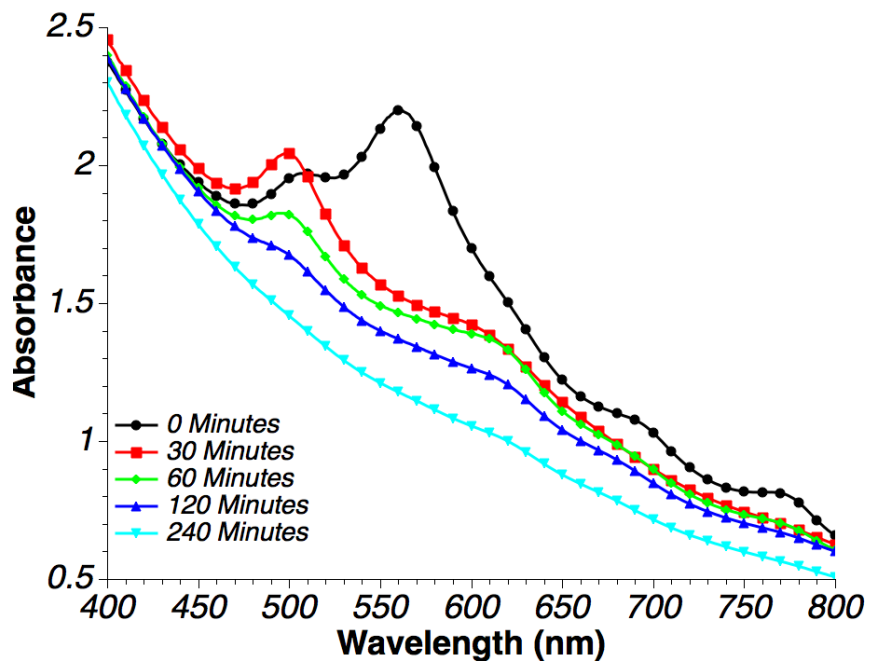
Figure 34. Hydrogen yields for P25, exfoliated HTiNbO<sub>5</sub>, and their composites with and without Pt.

### 3. Methylene Blue Dye Degradation

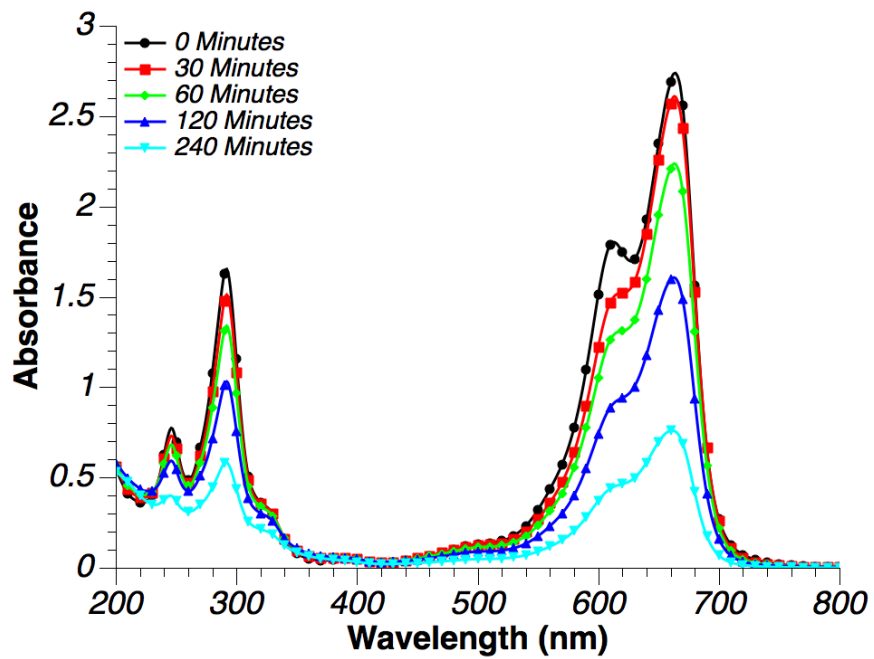
Methylene blue may be used as an indicator molecule to test reactivity towards organic contaminants.<sup>10</sup> Resulting UV-vis spectra and percent methylene blue are provided in Figure 35a-e and summarized in Table VII. Adsorption peaks were integrated to find intensities rather than using absorbance maxima due to the dynamic nature of the absorption peaks.



(c)



(d)



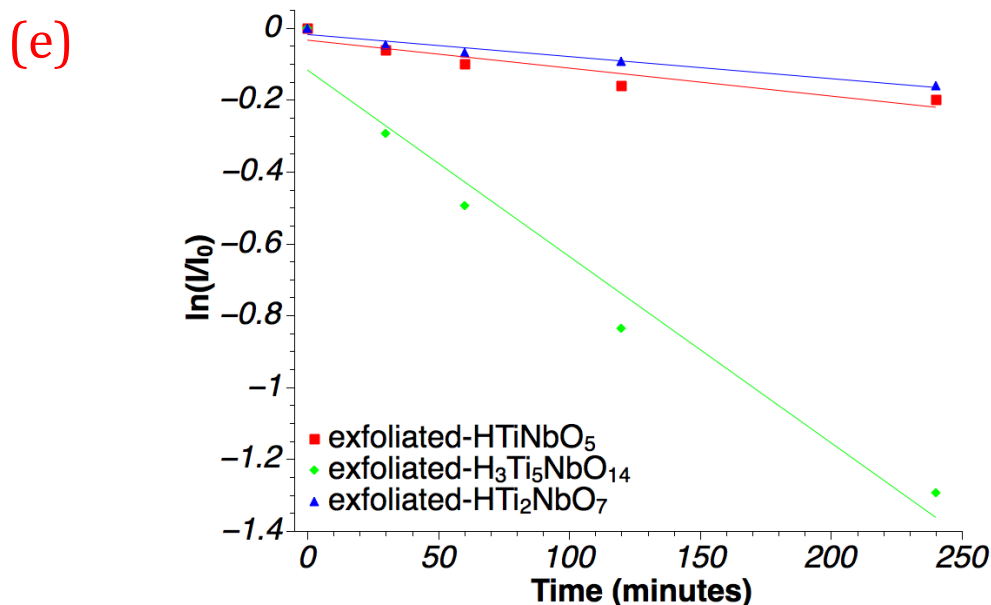


Figure 35. UV-vis transmission spectra for (a) exfoliated HTiNbO<sub>5</sub>, (b) exfoliated H<sub>3</sub>Ti<sub>5</sub>NbO<sub>14</sub>, (c) exfoliated HTi<sub>2</sub>NbO<sub>7</sub>, (d) water and methylene blue, (e) rate law decoloration calculated from peak areas integrated between 400-800 nm in a-c. Correlation coefficients are provided in Table VII.

Table VII: Methylene Blue Decomposition Rates, Correlation Coefficients, Theoretical Specific Surface Area, and Theoretical Specific Surface Charge For Each Chemistry.

	Exfoliated HTiNbO <sub>5</sub>	Exfoliated H <sub>3</sub> Ti <sub>5</sub> NbO <sub>14</sub>	Exfoliated HTi <sub>2</sub> NbO <sub>7</sub>
Rate [ $\ln(\frac{I}{I_0}) 10^3$ ]	-1.935	-4.566	-1.157
R <sup>2</sup>	0.875	0.967	0.957
tSSA (m <sup>2</sup> /g)	670	752	707
tSSC (C/g)	-436	-519	-318

Nanosheets suspensions turned violet when combined with methylene blue which shifted the adsorption spectra significantly compared to methylene blue without nanosheets, suggesting that methylene blue was adsorbed onto the nanosheets surface. Strong adsorption may alter the electronic structure of the nanosheet and result in non-linear reaction rates. The adsorption peak at approximately 300 nm (Figure 35d) was overwhelmed by nanosheet band gap adsorption and the primary methylene blue adsorption peak at 660 nm (Figure 35d) was blue-shifted approximately 100 nm (as indicated by 0 min spectra in (Figure 35a-c)). After 30 minutes, this peak was further blue-shifted or eliminated altogether in the case of exfoliated HTi<sub>2</sub>NbO<sub>7</sub>.

All nanosheet phases demonstrated exponentially decaying adsorption allowing for these systems to be evaluated by a first order kinetics model. Rate constants provided in Table VII show exfoliated  $\text{H}_3\text{Ti}_5\text{NbO}_{14}$  to be most active, followed by exfoliated  $\text{HTiNbO}_5$  and then exfoliated  $\text{HTi}_2\text{NbO}_7$ . The significantly stronger decomposition of methylene blue by exfoliated  $\text{H}_3\text{Ti}_5\text{NbO}_{14}$  compared to the other chemistries further suggest motif has little to no contribution on photocatalytic behavior. Unlike photocatalytic hydrogen production however, methylene blue decomposition did not suggest a definitive trend with chemistry (i.e. ratio of Ti:Nb). With that said, the highest ratio chemistry,  $\text{H}_3\text{Ti}_5\text{NbO}_{14}$ , decomposed methylene blue at a significantly greater rate than the other chemistries. This behavior has been reported elsewhere, for example by Akatsuka, who ascribes electron-hole recombination centers to the presence of multiple metal cations.<sup>17</sup>

## CONCLUSION

Nanosheets of  $\text{HTiNbO}_5$ ,  $\text{H}_3\text{Ti}_5\text{NbO}_{14}$ , and  $\text{HTi}_2\text{NbO}_7$  were synthesized by protonation and exfoliation of their ceramic parent phase. The resulting nanosheet suspensions appeared opalescent due to their liquid crystalline nature which facilitated controlled reassembly with acidic or cationic species. Reducing the pH of the nanosheet suspensions resulted in a gelled mesophase in which the effect of overlapping excluded volumes arrested particle motion and therefore yielded a high viscosity colloid. The viscosity was only found to increase below a critical pH (between 5-6). Diffraction patterns of gelled nanosheets revealed no short-range intersheet reflections but possessed in-sheet reflections reminiscent of the parent unit cells. Restacking schemes as explored by XRD were also found to vary as pH was reduced. The decrease in interlayer spacing and apparent recrystallization may possibly be due, in part, to the expulsion of interlayer species and/or hydronium.

Adding various salts to the nanosheet suspensions resulted in flocculation which occurred without an increase in viscosity. The flocculated mesophase, in contrast to a gel, is suggested as the result of restacked nanosheet clusters bound together into a long-range network via edge-to-face attraction between clusters. It was hypothesized that the structure of dry nanosheet assemblies should be reminiscent of the gelled or flocculated mesophases which produced them. BET measurements on dry gels revealed strong hysteresis and mesoporosity due to the formation of small slit-like pores formed between restacked sheets. Floccules, however, revealed very little hysteresis and much larger pores due to the formation of voids between tactoids.

X-ray diffraction patterns of gelled and flocculated powders could be roughly indexed in terms of the parent phase unit cells. band gap energies of the parent phases, exfoliated, and reassembled nanosheets were studied using diffuse-reflectance UV-Vis spectroscopy. The band edges were found to decrease from approximately 4.1 to 3.6 eV after exfoliation. Band gaps increased to energies between 3.8-4.1 eV when reassembled with various cations, although no clear trend could be discerned with the flocculating cation used. The exfoliated nanosheets were found to be weakly photoactive without a Pt co-catalyst as measured by  $\text{H}_2$  yield. However, photoactivity improved more than an order-of-magnitude with 1 wt% Pt co-catalyst. Photodegradation also revealed activity towards methylene blue. In both cases, exfoliated  $\text{H}_3\text{Ti}_5\text{NbO}_{14}$  demonstrated the highest activity due to the high ratio of Ti:Nb. Composites were formed by

flocculating P25 and exfoliated HTiNbO<sub>5</sub> nanosheets according to the methods detailed in this study. The composite demonstrated significantly improved H<sub>2</sub> production without Pt co-catalyst compared to P25 or exfoliated HTiNbO<sub>5</sub>. The present study has therefore demonstrated reliably controlled HTiNbO<sub>5</sub>, H<sub>3</sub>Ti<sub>5</sub>NbO<sub>14</sub>, and HTi<sub>2</sub>NbO<sub>7</sub> nanosheet assemblies via their colloidal processing. The photoactivity of titanate-niobate nanosheets and their assemblies has also been demonstrated. Nanosheet reassembly with various metal cations may allow for unique properties - photocatalytic, optical, or otherwise - to be discovered and exploited.

## FUTURE WORK

Explicitly studying the long-range structure and connectivity of gelled and flocculated titanate-niobate nanosheets is an interesting, albeit underdeveloped, aspect of this study. To that end, small angle x-ray and neutron scattering have been successfully employed to study other colloidal systems and could be applied to the mesophases reported here.<sup>83,84,45,85,30,60,61,47,86,59,37,87,88</sup> Using these techniques in conjunction allows the shape and size of sheets, nanosheet clusters, and arrangement of sheets to be studied in great detail. The evolution of a nanosheet colloid from isotropic to gelled may also be studied by measuring small angle patterns at various pHs, much like this evolution has been studied as a function of concentration and aspect ratio for other systems.<sup>87</sup> Neutron total scattering and x-ray reflectivity (XRR, following Fenter *et al.*<sup>72</sup>) may also be employed to study the hydration behavior of these nanosheets. X-ray reflectivity requires samples with restacked sheets and is therefore appropriate to study films (e.g. Figure 15-Figure 17) but not colloidal suspensions (e.g. Figure 13 and Figure 21). One particularly interesting application of both neutron scattering and XRR would be the restacking behavior of titanate-niobate nanosheets as a function of pH. Figure 15 through Figure 17 reveal peculiar restacking and morphological changes when pH is sufficiently reduced. Neutron scattering and XRR may be used to study water and other intercalated species (especially organics, for example TBA) between sheets, while x-ray scattering would be better suited to explore the nanosheet structure itself. Such a study should include assemblies carefully produced at various pHs, allowing BET to explore the mesostructure of assembled nanosheets throughout their structural evolution from high to low pH.

Various changes in the nanosheets from high to low pH, and perhaps by other treatments as well, may yield properties advantageous to photochemistry and electrochemistry. Explicitly linking improvements in photochemical yield to structural (or electronic) changes within the nanosheet or on the nanosheet surface will benefit the development of future catalysts. An investigation of electrochemical behavior is absent from this study due to the difficulty in producing repeatable and reliable electrochemical cells from low conductivity nanosheets. An industrious investigator may discover interesting behavior in titanate-niobate nanosheets by employing and expanding upon the various techniques presented in this study. Of particular interest is the role crystallographic motif and chemistry (Ti/Nb ratio) play in promoting

electrochemical intercalation. X-ray scattering and NMR or neutron scattering (depending on the intercalating species) are ideal techniques to probe the nanosheet surface structure at various stages of the electrochemical cycle. Concurrently, XPS and XANES should be used to study the redox behavior of Ti and Nb in these nanosheets.

## REFERENCES

1. A. Fujishima and K. Honda, "Electrochemical Evidence for the Mechanism of the Primary Stage of Photosynthesis," *Bull. Chem. Soc. Jpn.*, **44** [4] 1148-50 (1971).
2. A. Fujishima and K. Honda, "TiO<sub>2</sub> Photoelectrochemistry and Photocatalysis," *Nature*, **238** [5358] 37-8 (1972).
3. C. A. Martínez-Huitle and E. Brillas, "Decontamination of Wastewaters Containing Synthetic Organic Dyes by Electrochemical Methods: A General Review," *Appl. Catal., B*, **87** [3] 105-45 (2009).
4. M. R. Hoffmann, S. T. Martin, W. Choi, and D. W. Bahnemann, "Environmental Applications of Semiconductor Photocatalysis," *Chem. Rev.*, **95** [1] 69-96 (1995).
5. A. A. Ismail and D. W. Bahnemann, "Mesoporous Titania Photocatalysts: Preparation, Characterization and Reaction Mechanisms," *J. Mater. Chem.*, **21** [32] 11686-707 (2011).
6. A. J. Bard and M. A. Fox, "Artificial Photosynthesis: Solar Splitting of Water to Hydrogen and Oxygen," *Acc. Chem. Res.*, **28** [3] 141-5 (1995).
7. H. Kato and A. Kudo, "Water Splitting into H<sub>2</sub> and O<sub>2</sub> on Alkali Tantalate Photocatalysts ATaO<sub>3</sub> (a= Li, Na, and K)," *J. Phys. Chem. B*, **105** [19] 4285-92 (2001).
8. H. Kato, K. Asakura, and A. Kudo, "Highly Efficient Water Splitting into H<sub>2</sub> and O<sub>2</sub> over Lanthanum-Doped NaTaO<sub>3</sub> Photocatalysts with High Crystallinity and Surface Nanostructure," *J. Am. Chem. Soc.*, **125** [10] 3082-9 (2003).
9. X. Chen and S. S. Mao, "Titanium Dioxide Nanomaterials: Synthesis, Properties, Modifications, and Applications," *Chem. Rev.*, **107** [7] 2891-959 (2007).
10. V. L. Blair, E. J. Nichols, J. Liu, and S. T. Misture, "Surface Modification of Nanosheet Oxide Photocatalysts," *Appl. Surf. Sci.*, **268** 410-5 (2013).
11. Y. Kobayashi, H. Hata, M. Salama, and T. E. Mallouk, "Scrolled Sheet Precursor Route to Niobium and Tantalum Oxide Nanotubes," *Nano Lett.*, **7** [7] 2142-5 (2007).
12. M. Anpo, T. Shima, S. Kodama, and Y. Kubokawa, "Photocatalytic Hydrogenation of Propyne with Water on Small-Particle Titania: Size Quantization Effects and Reaction Intermediates," *J. Phys. Chem.*, **91** [16] 4305-10 (1987).
13. L. Kavan, T. Stoto, M. Graetzel, D. Fitzmaurice, and V. Shklover, "Quantum Size Effects in Nanocrystalline Semiconducting Titania Layers Prepared by Anodic

- Oxidative Hydrolysis of Titanium Trichloride," *The J. Phys. Chem.*, **97** [37] 9493-8 (1993).
14. M. C. Sarahan, E. C. Carroll, M. Allen, D. S. Larsen, N. D. Browning, and F. E. Osterloh, "K<sub>4</sub>Nb<sub>6</sub>O<sub>17</sub>-Derived Photocatalysts for Hydrogen Evolution from Water: Nanoscrolls Versus Nanosheets," *J. Solid State Chem.*, **181** [7] 1678-83 (2008).
  15. M. R. Allen, A. Thibert, E. M. Sabio, N. D. Browning, D. S. Larsen, and F. E. Osterloh, "Evolution of Physical and Photocatalytic Properties in the Layered Titanates A<sub>2</sub>Ti<sub>4</sub>O<sub>9</sub> (a= K, H) and in Nanosheets Derived by Chemical Exfoliation†," *Chem. Mater.*, **22** [3] 1220-8 (2009).
  16. N. Sakai, Y. Ebina, K. Takada, and T. Sasaki, "Electronic Band Structure of Titania Semiconductor Nanosheets Revealed by Electrochemical and Photoelectrochemical Studies," *J. Am. Chem. Soc.*, **126** [18] 5851-8 (2004).
  17. K. Akatsuka, G. Takanashi, Y. Ebina, M.-a. Haga, and T. Sasaki, "Electronic Band Structure of Exfoliated Titanium-and/or Niobium-Based Oxide Nanosheets Probed by Electrochemical and Photoelectrochemical Measurements," *The J. Phys. Chem. C*, **116** [23] 12426-33 (2012).
  18. K. Chen, Z. Jiang, J. Qin, Y. Jiang, R. Li, H. Tang, and X. Yang, "Synthesis and Improved Photocatalytic Activity of Ultrathin TiO<sub>2</sub> Nanosheets with Nearly 100% Exposed (001) Facets," *Ceram. Int.*, **40** [10] 16817-23 (2014).
  19. J. L. Gunjekar, T. W. Kim, H. N. Kim, I. Y. Kim, and S.-J. Hwang, "Mesoporous Layer-by-Layer Ordered Nanohybrids of Layered Double Hydroxide and Layered Metal Oxide: Highly Active Visible Light Photocatalysts with Improved Chemical Stability," *J. Am. Chem. Soc.*, **133** [38] 14998-5007 (2011).
  20. L. Wang and T. Sasaki, "Titanium Oxide Nanosheets: Graphene Analogues with Versatile Functionalities," *Chem. Rev.*, **114** [19] 9455-86 (2014).
  21. M. A. Bizeto and V. R. Constantino, "Structural Aspects and Thermal Behavior of the Proton-Exchanged Layered Niobate K<sub>4</sub>Nb<sub>6</sub>O<sub>17</sub>," *Mater. Res. Bull.*, **39** [11] 1729-36 (2004).
  22. M. A. Bizeto and V. R. Constantino, "Layered H<sub>2</sub>K<sub>2</sub>Nb<sub>6</sub>O<sub>17</sub> Exfoliation Promoted by N-Butylamine," *Mater. Res. Bull.*, **39** [12] 1811-20 (2004).
  23. Y. Ebina, T. Sasaki, M. Harada, and M. Watanabe, "Restacked Perovskite Nanosheets and Their Pt-Loaded Materials as Photocatalysts," *Chem. Mater.*, **14** [10] 4390-5 (2002).
  24. J. He, A. Xu, L. Hu, N. Wang, W. Cai, B. Wang, J. Hu, and Z. Li, "Layered KTiNbO<sub>5</sub> Photocatalyst Modified with Transitional Metal Ions (Mn 2+, Ni 2+): Investigation of

- Microstructure and Photocatalytic Reaction Pathways for the Oxidation of Dimethyl Sulfide and Ethyl Mercaptan," *Powder Technol.*, **270** 154-62 (2015).
25. N. Miyamoto and T. Nakato, "Liquid Crystalline Nanosheet Colloids with Controlled Particle Size Obtained by Exfoliating Single Crystal of Layered Niobate  $K_4Nb_6O_{17}$ ," *J. Phys. Chem. B*, **108** [20] 6152-9 (2004).
  26. T. Nakato, Y. Yamada, and N. Miyamoto, "Photoinduced Charge Separation in a Colloidal System of Exfoliated Layered Semiconductor Controlled by Coexisting Aluminosilicate Clay," *The J. Phys. Chem. B*, **113** [5] 1323-31 (2009).
  27. E. M. Sabio, M. Chi, N. D. Browning, and F. E. Osterloh, "Charge Separation in a Niobate Nanosheet Photocatalyst Studied with Photochemical Labeling," *Langmuir*, **26** [10] 7254-61 (2010).
  28. U. Unal, Y. Matsumoto, N. Tamoto, M. Koinuma, M. Machida, and K. Izawa, "Visible Light Photoelectrochemical Activity of  $K_4Nb_6O_{17}$  Intercalated with Photoactive Complexes by Electrostatic Self-Assembly Deposition," *J. Solid State Chem.*, **179** [1] 33-40 (2006).
  29. N. Miyamoto and T. Nakato, "Liquid Crystalline Colloidal System Obtained by Mixing Niobate and Aluminosilicate Nanosheets: A Spectroscopic Study Using a Probe Dye," *Langmuir*, **19** [19] 8057-64 (2003).
  30. J. Mang, S. Kumar, and B. Hammouda, "Discotic Micellar Nematic and Lamellar Phases under Shear Flow," *EPL (Europhys. Lett.)*, **28** [7] 489 (1994).
  31. X. Fan, B. Lin, H. Liu, L. He, Y. Chen, and B. Gao, "Remarkable Promotion of Photocatalytic Hydrogen Evolution from Water on  $TiO_2$ -Pillared Titanoniobate," *Int. J. Hydrogen Energy*, **38** [2] 832-9 (2013).
  32. T. Sasaki and M. Watanabe, "Osmotic Swelling to Exfoliation. Exceptionally High Degrees of Hydration of a Layered Titanate," *J. Am. Chem. Soc.*, **120** [19] 4682-9 (1998).
  33. O. Zhang, B.-Z. Lin, Y.-L. Chen, B.-F. Gao, L.-M. Fu, and B. Li, "Electrochemical and Photoelectrochemical Characteristics of  $TiNbO_5$  Nanosheet Electrode," *Electrochim. Acta*, **81** 74-82 (2012).
  34. K. P. Lucht and J. L. Mendoza-Cortes, "Birnessite: A Layered Manganese Oxide to Capture Sunlight for Water-Splitting Catalysis," *The J. Phys. Chem. C*, **119** [40] 22838-46 (2015).
  35. S. Adireddy, C. E. Carbo, Y. Yao, J. M. Vargas, L. Spinu, and J. B. Wiley, "High-Yield Solvothermal Synthesis of Magnetic Peapod Nanocomposites Via the Capture of

- Preformed Nanoparticles in Scrolled Nanosheets," *Chem. Mater.*, **25** [19] 3902-9 (2013).
36. S. Adireddy, C. E. Carbo, T. Rostamzadeh, J. M. Vargas, L. Spinu, and J. B. Wiley, "Peapod - Type Nanocomposites through the in Situ Growth of Gold Nanoparticles within Preformed Hexaniobate Nanoscrolls," *Angew. Chem., Int. Ed.*, **53** [18] 4614-7 (2014).
  37. T. Nakato, N. Miyamoto, A. Harada, and H. Ushiki, "Sol-Gel Transition of Niobium Oxide Nanosheet Colloids: Hierarchical Aspect of a Novel Macroscopic Property Appearing in Colloidally Dispersed States of Layered Niobate  $K_4Nb_6O_{17}$ ," *Langmuir*, **19** [8] 3157-63 (2003).
  38. T. Nakato, Y. Yamada, M. Nakamura, and A. Takahashi, "Photoinduced Electron Accumulation in Colloidally Dispersed Wide Band-Gap Semiconductor Nanosheets," *J. Colloid Interface Sci.*, **354** [1] 38-44 (2011).
  39. K. Maeda and T. E. Mallouk, "Comparison of Two-and Three-Layer Restacked Dion-Jacobson Phase Niobate Nanosheets as Catalysts for Photochemical Hydrogen Evolution," *J. Mater. Chem.*, **19** [27] 4813-8 (2009).
  40. R. Liu, W. Guo, B. Sun, J. Pang, M. Pei, and G. Zhou, "Composites of Rutile  $TiO_2$  Nanorods Loaded on Graphene Oxide Nanosheet with Enhanced Electrochemical Performance," *Electrochim. Acta*, **156** 274-82 (2015).
  41. X. Luan, M. T. G. Wing, and Y. Wang, "Enhanced Photocatalytic Activity of Graphene Oxide/Titania Nanosheets Composites for Methylene Blue Degradation," *Mater. Sci. Semicond. Process.*, **30** 592-8 (2015).
  42. T. W. Kim, T. S. Jung, S.-H. Hyun, and S.-J. Hwang, "Mesoporous Assembly of 2d Manganate Nanosheets Intercalated with Cobalt Ions," *Mater. Lett.*, **64** [5] 565-8 (2010).
  43. Y. R. Lee, I. Y. Kim, T. W. Kim, J. M. Lee, and S. J. Hwang, "Mixed Colloidal Suspensions of Reduced Graphene Oxide and Layered Metal Oxide Nanosheets: Useful Precursors for the Porous Nanocomposites and Hybrid Films of Graphene/Metal Oxide," *Chem. Eur. J.*, **18** [8] 2263-71 (2012).
  44. M.-S. Song, K. M. Lee, Y. R. Lee, I. Y. Kim, T. W. Kim, J. L. Gunjekar, and S.-J. Hwang, "Porously Assembled 2d Nanosheets of Alkali Metal Manganese Oxides with Highly Reversible Pseudocapacitance Behaviors," *The J. Phys. Chem. C*, **114** [50] 22134-40 (2010).

45. P. A. Heiney, R. J. Butera, J. D. Londono, R. V. Davidson, and S. Mazur, "Network Growth in the Flocculation of Concentrated Colloidal Silica Dispersions," *J. Phys. Chem. B*, **104** [37] 8807-21 (2000).
46. H. Van Olphen, "Rheological Phenomena of Clay Sols in Connection with the Charge Distribution on the Micelles," *Discuss. Faraday Soc.*, **11** 82-4 (1951).
47. P. Mongondry, J. F. Tassin, and T. Nicolai, "Revised State Diagram of Laponite Dispersions," *J. Colloid Interface Sci.*, **283** [2] 397-405 (2005).
48. F. Pignon, A. Magnin, J.-M. Piau, B. Cabane, P. Lindner, and O. Diat, "Yield Stress Thixotropic Clay Suspension: Investigations of Structure by Light, Neutron, and X-Ray Scattering," *Phys. Rev. E*, **56** [3] 3281 (1997).
49. S. L. Tawari, D. L. Koch, and C. Cohen, "Electrical Double-Layer Effects on the Brownian Diffusivity and Aggregation Rate of Laponite Clay Particles," *J. Colloid Interface Sci.*, **240** [1] 54-66 (2001).
50. T. Nicolai and S. Cocard, "Dynamic Light-Scattering Study of Aggregating and Gelling Colloidal Disks," *J. Colloid Interface Sci.*, **244** [1] 51-7 (2001).
51. L. Onsager, "The Effects of Shape on the Interaction of Colloidal Particles," *Ann. N. Y. Acad. Sci.*, **51** [4] 627-59 (1949).
52. G. J. Vroege and H. N. Lekkerkerker, "Phase Transitions in Lyotropic Colloidal and Polymer Liquid Crystals," *Rep. Prog. Phys.*, **55** [8] 1241 (1992).
53. S. C. McGrother, D. C. Williamson, and G. Jackson, "A Re-Examination of the Phase Diagram of Hard Spherocylinders," *J. Chem. Phys.*, **104** [17] 6755-71 (1996).
54. D. Costa, F. Micali, F. Saija, and P. Giaquinta, "Entropy and Correlations in a Fluid of Hard Spherocylinders: The Onset of Nematic and Smectic Order," *J. Phys. Chem. B*, **106** [47] 12297-306 (2002).
55. H. Wensink, "Columnar Versus Smectic Order in Systems of Charged Colloidal Rods," *J. Chem. Phys.*, **126** [19] 194901 (2007).
56. J. Veerman and D. Frenkel, "Phase Behavior of Disklike Hard-Core Mesogens," *Phys. Rev. A*, **45** [8] 5632 (1992).
57. M. A. Bates, "Influence of Particle Shape on the Nematic—Isotropic Transition of Colloidal Platelet Systems," *J. Chem. Phys.*, **111** [4] 1732-6 (1999).
58. M. Bier, L. Harnau, and S. Dietrich, "Free Isotropic-Nematic Interfaces in Fluids of Charged Plate-like Colloids," *J. Chem. Phys.*, **123** [11] 114906 (2005).

59. V. V. Naik and S. Vasudevan, "Sol–Gel Transition in Dispersions of Layered Double-Hydroxide Nanosheets," *Langmuir*, **27** [21] 13276-83 (2011).
60. L. J. Michot, I. Bihannic, S. Maddi, C. Baravian, P. Levitz, and P. Davidson, "Sol/Gel and Isotropic/Nematic Transitions in Aqueous Suspensions of Natural Nontronite Clay. Influence of Particle Anisotropy. 1. Features of the I/N Transition," *Langmuir*, **24** [7] 3127-39 (2008).
61. L. J. Michot, C. Baravian, I. Bihannic, S. Maddi, C. Moyne, J. F. Duval, P. Levitz, and P. Davidson, "Sol– Gel and Isotropic/Nematic Transitions in Aqueous Suspensions of Natural Nontronite Clay. Influence of Particle Anisotropy. 2. Gel Structure and Mechanical Properties," *Langmuir*, **25** [1] 127-39 (2008).
62. T. Nakato, Y. Yamashita, and K. Kuroda, "Mesophase of Colloidally Dispersed Nanosheets Prepared by Exfoliation of Layered Titanate and Niobate," *Thin Solid Films*, **495** [1] 24-8 (2006).
63. T. Nakato, N. Miyamoto, and A. Harada, "Stable Liquid Crystalline Phases of Colloidally Dispersed Exfoliated Layered Niobates," *Chemical communications*, [1] 78-9 (2004).
64. H.-Y. Lin and Y.-S. Chang, "Photocatalytic Water Splitting on Au/HTiNbO<sub>5</sub> Nanosheets," *Int. J. Hydrogen Energy*, (2014).
65. A. Takagaki, M. Sugisawa, D. Lu, J. N. Kondo, M. Hara, K. Domen, and S. Hayashi, "Exfoliated Nanosheets as a New Strong Solid Acid Catalyst," *J. Am. Chem. Soc.*, **125** [18] 5479-85 (2003).
66. A. Takagaki, T. Yoshida, D. Lu, J. N. Kondo, M. Hara, K. Domen, and S. Hayashi, "Titanium Niobate and Titanium Tantalate Nanosheets as Strong Solid Acid Catalysts," *J. Phys. Chem. B*, **108** [31] 11549-55 (2004).
67. M. Osada, K. Akatsuka, Y. Ebina, H. Funakubo, K. Ono, K. Takada, and T. Sasaki, "Robust High-K Response in Molecularly Thin Perovskite Nanosheets," *ACS Nano*, **4** [9] 5225-32 (2010).
68. M. Osada, G. Takanashi, B. W. Li, K. Akatsuka, Y. Ebina, K. Ono, H. Funakubo, K. Takada, and T. Sasaki, "Controlled Polarizability of One - Nanometer - Thick Oxide Nanosheets for Tailored, High - K Nanodielectrics," *Advanced Functional Materials*, **21** [18] 3482-7 (2011).
69. B.-W. Li, M. Osada, Y. Ebina, K. Akatsuka, K. Fukuda, and T. Sasaki, "High Thermal Robustness of Molecularly Thin Perovskite Nanosheets and Implications for Superior Dielectric Properties," *ACS Nano*, **8** [6] 5449-61 (2014).

70. I. A. Shkrob and M. C. Sauer, "Hole Scavenging and Photo-Stimulated Recombination of Electron-Hole Pairs in Aqueous TiO<sub>2</sub> Nanoparticles," *J. Phys. Chem. B*, **108** [33] 12497-511 (2004).
71. M. Onoda, Y. Ebina, and T. Sasaki, "Simulation of the Powder Diffraction Pattern of Randomly Restacked Ca<sub>2</sub>Nb<sub>3</sub>O<sub>10</sub> Nanosheets," *J. Appl. Crystallogr.*, **42** [6] 1062-7 (2009).
72. P. Fenter and S. S. Lee, "Hydration Layer Structure at Solid-Water Interfaces," *MRS Bull.*, **39** [12] 1056-61 (2014).
73. P. D. Olmsted, "Perspectives on Shear Banding in Complex Fluids," *Rheol. Acta*, **47** [3] 283-300 (2008).
74. A. Stokes, "X-Ray Diffraction by Polycrystalline Materials," *Ch*, **17** 428 (1960).
75. T. Zhong, J. Tang, M. Zhu, Y. Hou, H. Wang, and H. Yan, "Synthesis and Characterization of Layered Niobate K<sub>4</sub>Nb<sub>6</sub>O<sub>17</sub> Thin Films by Niobium-Chelated Precursor," *J. Cryst. Growth*, **285** [1] 201-7 (2005).
76. L. J. Michot, I. Bihannic, K. Porsch, S. Maddi, C. Baravian, J. Mougel, and P. Levitz, "Phase Diagrams of Wyoming Na-Montmorillonite Clay. Influence of Particle Anisotropy," *Langmuir*, **20** [25] 10829-37 (2004).
77. J. Grigsby, H. Blanch, and J. Prausnitz, "Cloud-Point Temperatures for Lysozyme in Electrolyte Solutions: Effect of Salt Type, Salt Concentration and Ph," *Biophys. Chem.*, **91** [3] 231-43 (2001).
78. M. B. Sierra, V. I. Pedroni, F. E. Buffo, E. A. Disalvo, and M. A. Morini, "The Use of Zeta Potential as a Tool to Study Phase Transitions in Binary Phosphatidylcholines Mixtures," *Colloids Surf., B*, **142** 199-206 (2016).
79. P. Jayaweera and S. Hettiarachchi, "Determination of Zeta Potential and Ph of Zero Charge of Oxides at High Temperatures," *Rev. Sci. Instrum.*, **64** [2] 524 (1993).
80. K. S. Sing, "Reporting Physisorption Data for Gas/Solid Systems with Special Reference to the Determination of Surface Area and Porosity (Recommendations 1984)," *Pure Appl. Chem.*, **57** [4] 603-19 (1985).
81. T. Sekine, J. Yoshimura, A. Tanaka, K. Domen, K.-i. Maruya, and T. Onishi, "Photocatalytic Reaction on Layered Cs-Nb-Ti Complex Oxide," *Bull. Chem. Soc. Jpn.*, **63** [7] 2107-9 (1990).
82. D. C. Hurum, A. G. Agrios, K. A. Gray, T. Rajh, and M. C. Thurnauer, "Explaining the Enhanced Photocatalytic Activity of Degussa P25 Mixed-Phase TiO<sub>2</sub> Using EPR," *J. Phys. Chem. B*, **107** [19] 4545-9 (2003).

83. B. Ruzicka, E. Zaccarelli, L. Zulian, R. Angelini, M. Sztucki, A. Moussaïd, T. Narayanan, and F. Sciortino, "Observation of Empty Liquids and Equilibrium Gels in a Colloidal Clay," *Nat. Mater.*, **10** [1] 56-60 (2011).
84. A. Hasmy, R. Vacher, and R. Jullien, "Small-Angle Scattering by Fractal Aggregates: A Numerical Investigation of the Crossover between the Fractal Regime and the Porod Regime," *Phys. Rev. B*, **50** [2] 1305 (1994).
85. B. Lemaire, P. Panine, J. Gabriel, and P. Davidson, "The Measurement by SAXS of the Nematic Order Parameter of Laponite Gels," *EPL (Europhys. Lett.)*, **59** [1] 55 (2002).
86. A. Mourchid, A. Delville, J. Lambard, E. Lecolier, and P. Levitz, "Phase Diagram of Colloidal Dispersions of Anisotropic Charged Particles: Equilibrium Properties, Structure, and Rheology of Laponite Suspensions," *Langmuir*, **11** [6] 1942-50 (1995).
87. D. Yamaguchi, N. Miyamoto, T. Fujita, T. Nakato, S. Koizumi, N. Ohta, N. Yagi, and T. Hashimoto, "Aspect-Ratio-Dependent Phase Transitions and Concentration Fluctuations in Aqueous Colloidal Dispersions of Charged Platelike Particles," *Phys. Rev. E*, **85** [1] 011403 (2012).
88. D. Yamaguchi, N. Miyamoto, S. Koizumi, T. Nakato, and T. Hashimoto, "Hierarchical Structure of Niobate Nanosheets in Aqueous Solution," *Appl. Crystallogr.*, **40** [s1] s101-s5 (2007).